Quaternary Science Reviews 220 (2019) 30–74

Contents lists available at ScienceDirect

Quaternary Science Reviews

journal homepage: www.elsevier.com/locate/quascirev

Invited review

Mechanisms of millennial-scale atmospheric CO_2 change in numerical model simulations

Julia Gottschalk [a], [b], *, Gianna Battaglia [c], Hubertus Fischer [c], Thomas L. Frölicher [c], Samuel L. Jaccard [a], Aurich Jeltsch-Thömmes [c], Fortunat Joos [c], Peter Köhler [d], Katrin J. Meissner [e], [f], Laurie Menviel [e], [f], Christoph Nehrbass-Ahles [c], [g], Jochen Schmitt [c], Andreas Schmittner [h], Luke C. Skinner [g], Thomas F. Stocker [c]

[a] Institute of Geological Sciences and Oeschger Center for Climate Change Research, University of Bern, Bern, Switzerland
[b] Lamont-Doherty Earth Observatory of Columbia University, Palisades, NY, USA
[c] Climate and Environmental Physics, Physics Institute, and Oeschger Center for Climate Change Research, University of Bern, Bern, Switzerland
[d] Alfred-Wegener-Institut, Helmholtz-Zentrum für Polar- und Meeresforschung, Bremerhaven, Germany
[e] Climate Change Research Centre, University of New South Wales, Sydney, Australia
[f] ARC Centre of Excellence for Climate Extremes, Australia
[g] Godwin Laboratory for Palaeoclimate Research, Earth Sciences Department, University of Cambridge, Cambridge, United Kingdom
[h] College of Earth, Ocean, and Atmospheric Sciences, Oregon State University, Corvallis, OR, USA

ARTICLE INFO

Article history:
Received 21 January 2019
Received in revised form
14 May 2019
Accepted 15 May 2019

Keywords:
Palaeoclimate modelling
Carbon cycle
Atmospheric CO_2 variations
Freshwater hosing
Southern-hemisphere westerlies
Sea ice
Dust

ABSTRACT

Numerical models are important tools for understanding the processes and feedbacks in the Earth system, including those involving changes in atmospheric CO_2 ($CO_{2,atm}$) concentrations. Here, we compile 55 published model studies (consisting of 778 individual simulations) that assess the impact of six forcing mechanisms on millennial-scale $CO_{2,atm}$ variations: changes in freshwater supply to the North Atlantic and Southern Ocean, the strength and position of the southern-hemisphere westerlies, Antarctic sea ice extent, and aeolian dust fluxes. We generally find agreement on the direction of simulated $CO_{2,atm}$ change across simulations, but the amplitude of change is inconsistent, primarily due to the different complexities of the model representation of Earth system processes. When freshwater is added to the North Atlantic, a reduced Atlantic Meridional Overturning Circulation (AMOC) is generally accompanied by an increase in Southern Ocean- and Pacific overturning, reduced Antarctic sea ice extent, spatially varying export production, and changes in carbon storage in the Atlantic (rising), in other ocean basins (generally decreasing) and on land (more varied). Positive or negative $CO_{2,atm}$ changes are simulated during AMOC minima due to a spatially and temporally varying dominance of individual terrestrial and oceanic drivers (and compensating effects between them) across the different models. In contrast, AMOC recoveries are often accompanied by rising $CO_{2,atm}$ levels, which are mostly driven by ocean carbon release (albeit from different regions). The magnitude of simulated $CO_{2,atm}$ rise broadly scales with the duration of the AMOC perturbation (i.e., the stadial length). When freshwater is added to the Southern Ocean, reduced deep-ocean ventilation drives a $CO_{2,atm}$ drop via reduced carbon release from the Southern Ocean. Although the impacts of shifted southern-hemisphere westerlies are inconsistent across model simulations, their intensification raises $CO_{2,atm}$ via enhanced Southern Ocean Ekman pumping. Increased supply of aeolian dust to the ocean, and thus iron fertilisation of marine productivity, consistently lowers modelled $CO_{2,atm}$ concentrations via more efficient nutrient utilisation. The magnitude of $CO_{2,atm}$ change in response to dust flux variations, however, largely depends on the complexity of models' marine ecosystem and iron cycle. This especially applies to simulations forced by Antarctic sea ice changes, in which the direction of simulated $CO_{2,atm}$ change varies greatly across model hierarchies. Our compilation highlights that no single (forcing) mechanism can explain observed past millennial-

---

* Corresponding author. Lamont-Doherty Earth Observatory of Columbia University, Palisades, NY, USA.
E-mail address: jgottsch@ldeo.columbia.edu (J. Gottschalk).

https://doi.org/10.1016/j.quascirev.2019.05.013

scale $CO_{2,atm}$ variability, and identifies important future needs in coupled carbon cycle-climate modelling to better understand the mechanisms governing $CO_{2,atm}$ changes in the past.

---

1. Introduction

Numerical models represent important tools to test our understanding of how the Earth system operates under past, present or future boundary conditions, when subjected to a variety of forcing mechanisms. They contribute to quantitatively assess first-order sequences of climate events, -sensitivities and -feedbacks, and can be compared against spatially and temporally limited proxy data from a variety of climate archives. Questions regarding the nature and characteristics of global climate-carbon cycle feedbacks have motivated a plethora of model simulations directed at testing hypotheses regarding environmental processes and trigger mechanisms of global carbon cycle change, as well as making predictions of the future (e.g., Randall et al., 2007; Eby et al., 2013; Hülse et al., 2017).

In its infant years in the mid-fifties, climate modelling was based on highly idealised box models (e.g., Eriksson and Welander, 1956) and box-diffusion models (e.g., Oeschger et al., 1975), and continued with the development of atmospheric, oceanic and subsequently coupled atmosphere-ocean general circulation models (AOGCM) in the 1960s (e.g., Bryan and Cox, 1967; Bryan, 1969; Manabe, 1969a, 1969b; Hansen et al., 1983). With the implementation of biogeochemical processes (e.g., Sarmiento et al., 1988; Bacastow and Maier-Reimer, 1990; Foley et al., 1998; Cox et al., 2000; Schulz et al., 2001), the so-called coupled carbon cycle-climate models or Earth system models (ESMs) have expanded our understanding of the global carbon cycle under different climate conditions. In the 1990s, Earth system models of intermediate complexity (EMICs) became popular (Claussen et al., 2002), because simulations with EMICs are computationally efficient. EMICs are typically applied in low spatial resolution and include a wide range of Earth system processes, albeit often in parameterised form, allowing long (i.e., multi-millennial) simulations.

Early estimates of past $CO_{2,atm}$ levels derived from polar ice cores (e.g., Delmas et al., 1980; Neftel et al., 1982) have initiated model investigations to unravel the causes of lower-than-Holocene $CO_{2,atm}$ values, initially using simple and highly idealised three- to five-box models (e.g., Knox Ennever and McElroy, 1981; Berger and Keir, 1984; Knox and McElroy, 1984; Sarmiento and Toggweiler, 1984; Siegenthaler and Wenk, 1984; Toggweiler and Sarmiento, 1985; Wenk and Siegenthaler, 1985), and subsequently >10-box models (e.g., Broecker and Peng, 1986, 1987; Keir, 1988; Munhoven and François, 1996; Köhler et al., 2005a; Köhler and Fischer, 2006). Some of these studies have highlighted the crucial role of the Southern Ocean (SOc) in driving past $CO_{2,atm}$ variations, primarily through hypothesised reduced vertical mixing and/or enhanced nutrient utilisation during glacial times (Knox and McElroy, 1984; Sarmiento and Toggweiler, 1984; Siegenthaler and Wenk, 1984; Köhler et al., 2005a). The viability of other mechanisms governing variations in $CO_{2,atm}$ levels has also been illuminated by numerical model simulations, including processes such as ocean solubility changes (e.g., Keir, 1993; Bacastow, 1996; Ito and Follows, 2003), iron fertilisation of marine biota (e.g., Joos et al., 1991; Peng and Broecker, 1991; Watson et al., 2000), coral reef build-up (e.g., Berger and Keir, 1984; Opdyke and Walker, 1992; Ridgwell et al., 2003), changes in the ocean carbonate system (e.g., Broecker and Peng, 1987; Boyle, 1988), CO_2 fertilisation changes and biome shifts on land (e.g., Prentice and Fung, 1990), ocean temperature effects on the remineralisation of marine organic matter (e.g., Matsumoto et al., 2007; Kwon et al., 2009), as well as marine ecosystem changes (e.g., Archer and Maier-Reimer, 1994; Brzezinski et al., 2002; Matsumoto et al., 2002). The level of scientific understanding of these different processes varies, and no consensus has yet been reached on the relative quantitative contributions of each mechanism to $CO_{2,atm}$ change (see review of Kohfeld and Ridgwell, 2009).

Since the late 1990s, well-dated and (sub-) millennially resolved $CO_{2,atm}$ records from Antarctic ice cores reveal marked millennial-scale variations in $CO_{2,atm}$ concentrations on the order of 10–30 ppm, or larger. These represent a distinct feature of the last glacial period (Fig. 1; Stauffer et al., 1998; Indermühle et al., 2000; Ahn and Brook, 2008; Bereiter et al., 2012) or the last deglaciation (Fischer et al., 1999; Monnin et al., 2001; Marcott et al., 2014), respectively, and possibly earlier glacial periods (Petit et al., 1999; Siegenthaler et al., 2005; Lüthi et al., 2008). Millennial-scale $CO_{2,atm}$ changes are found to be tightly linked with inter-hemispheric climate variability: past increases in $CO_{2,atm}$ occurred primarily during millennial cold periods in the North Atlantic (NAtl), i.e., stadials, whereas decreases in $CO_{2,atm}$ were synchronous with millennial NAtl warm periods, i.e., interstadials (Fig. 1a,b). Abrupt oscillations in northern-hemisphere temperatures are generally believed to be linked with perturbations of the Atlantic Meridional Overturning Circulation (AMOC) that may have been related to varying freshwater (FW) supply to the NAtl (with the strongest and longest of these FW events occurring during stadials dubbed “Heinrich (H) events”) (Fig. 1a; e.g., Broecker, 1997; Rahmstorf, 2002; Lynch-Stieglitz, 2017). Perturbations of the AMOC cause adjustments of the meridional heat transport that lead to opposite but less abrupt temperature changes in the southern hemisphere, i.e., warming during stadials and cooling during interstadials (referred to as “bipolar seesaw” mechanism; Fig. 1a,c; Crowley, 1992; Stocker and Johnsen, 2003; EPICA Community Members, 2006; Buizert et al., 2018; Pedro et al., 2018). AMOC perturbations are also hypothesised to result in rapid (quasi-immediate) changes in the strength and/or position of the southern-hemisphere westerlies (SHW) (e.g., Anderson et al., 2009; Lee et al., 2011; Jaccard et al., 2016), contributing to changes in SOc temperature (e.g., Buizert et al., 2018; Pedro et al., 2018). Millennial $CO_{2,atm}$ variability may also be linked with changes in Antarctic sea ice extent (e.g., Fischer et al., 2007a,b; Rae et al., 2018; Fig. 1d) and in aeolian dust fluxes to the ocean (e.g., Lambert et al., 2012; Martínez-García et al., 2014; Landais et al., 2015; Fig. 1e). Based on marine proxy data, millennial-scale $CO_{2,atm}$ changes were suggested to have resulted from changes in SOc vertical mixing and SOc-to-atmosphere CO_2 fluxes in response to AMOC perturbations (Skinner et al., 2010, 2014; as illustrated in Fig. 2). NAtl climate- and $CO_{2,atm}$ anomalies are also thought to be linked with variations in CO_2 release from the SOc through an atmospheric teleconnection, in which for instance increases in the SHW wind intensity during AMOC perturbations lead to variations in Ekman pumping, and hence in elevated ocean-to-atmosphere CO_2 fluxes (Anderson et al., 2009; Jaccard et al., 2016; as illustrated in Fig. 2). However, the relative contributions of these oceanic and atmospheric processes (i.e., “teleconnections”)

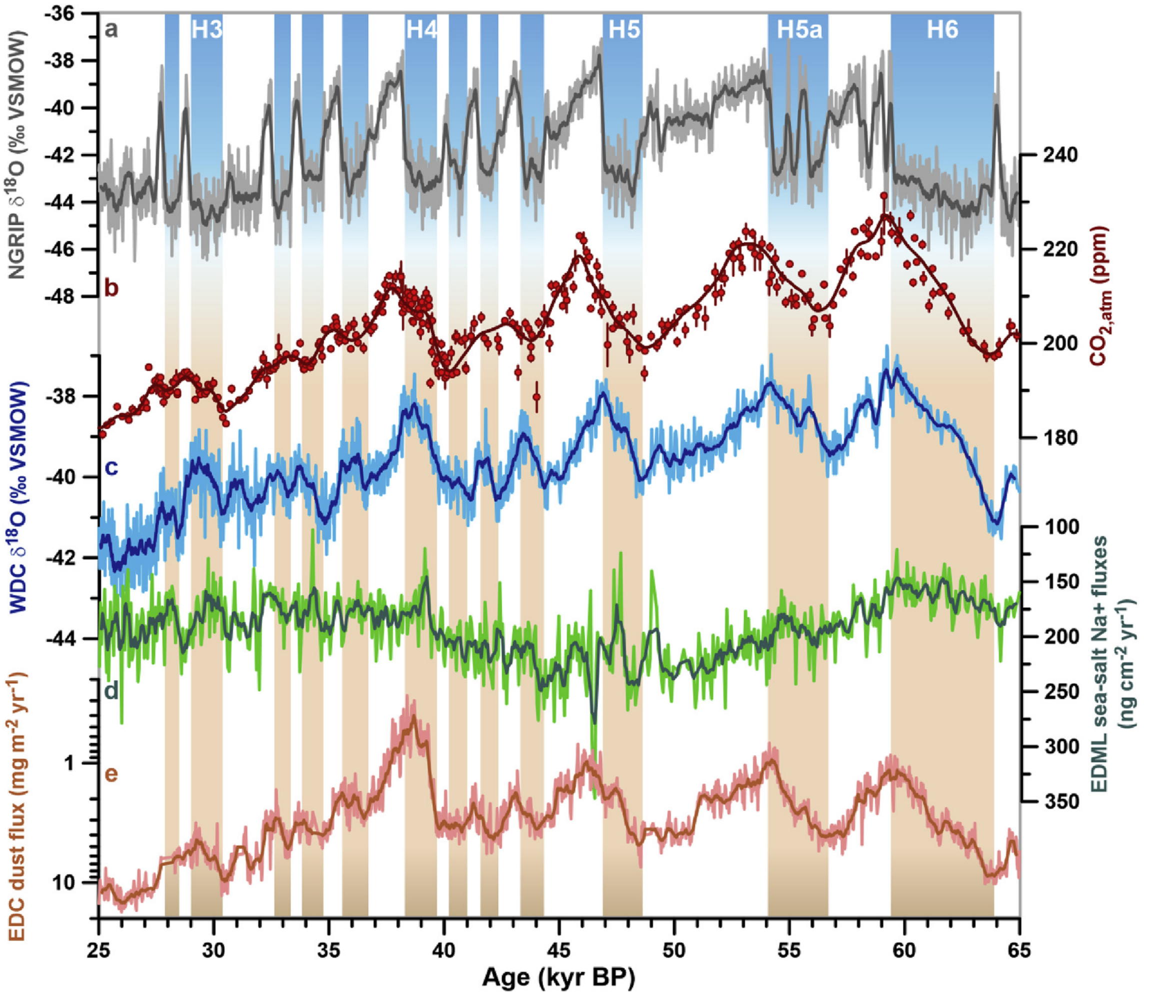

Fig. 1. Observations of millennial-scale climate variability in Greenland and Antarctic ice cores have stimulated numerous numerical model simulations that test and aim to identify the mechanisms governing atmospheric CO_2 ($CO_{2,atm}$) change. a) Greenland ice core (NGRIP) $\delta^{18}O$ changes (NGRIP members, 2004), b) composite Antarctic ice core $CO_{2,atm}$ record and $CO_{2,atm}$ spline (Köhler et al., 2017), c) WAIS Divide ice core (WDC) $\delta^{18}O$ variations (WAIS Divide Project Members, 2015), d) EPICA Dronning Maud Land (EDML) ice-core sea-salt Na^+ fluxes (Fischer et al., 2007a, 2007b), and e) EPICA Dome C (EDC) dust fluxes (Lambert et al., 2012). Northern-hemisphere cold intervals (stadials) and phases of Antarctic warming that are paralleled by gradually rising $CO_{2,atm}$ levels are respectively highlighted by blue and orange vertical bars. Strong and prolonged stadials are generally referred to as Heinrich (H) events.

to millennial-scale $CO_{2,atm}$ variations remain unclear.

A wealth of numerical model simulations has been performed in order to investigate the dynamics behind observed millennial-scale climate variability (Fig. 1) and to test proposed mechanisms of millennial-scale $CO_{2,atm}$ change (Fig. 2). Specifically, FW hosing both in the NAtl or SOc is often imposed to induce changes in meridional ocean heat transport, and hence stimulate a bipolar seesaw response, in order to assess parallel adjustments of the global carbon cycle. Other simulations are forced by prescribed changes in the SHW wind intensity and/or their latitudinal position in order to investigate their role in past $CO_{2,atm}$ changes, because the atmospheric component of most coupled carbon cycle-climate models capable of running long simulations is very simple. This also applies to simulations forced by variations in Antarctic sea ice extent and aeolian dust fluxes. Given structural model differences (such as grid resolution, complexity of model components, or parameterisations) and/or variable experimental designs across model simulations, a comprehensive and comparative analysis of numerical simulations of $CO_{2,atm}$ change with respect to the experimental design and the applied forcing, and their realistic representation of past climate events, is warranted.

Here, we compile 55 published model studies that investigate millennial-scale changes in $CO_{2,atm}$ (Table 1, also see expanded version in Table S1). We systematically catalogue the simulated $CO_{2,atm}$ change from 778 individual simulations as a function of the applied forcing, the climate boundary conditions (i.e., interglacial and glacial) and the model complexity (Table 1, Tables S2–S7). The model complexity both combines the structural complexity (i.e., the model components and their representation) as well as the spatial complexity of the model (i.e., the model's grid resolution); both of which are linked to some degree. We categorise the coupled carbon cycle-climate models as box models (circles; Table S8), dynamic global vegetation models (DVM, crosses), EMICs (diamonds), ocean-only general circulation models (OGCMs) with biogeochemistry (five-point star), and coupled climate-carbon cycle AOGCMs (i.e., ESMs; six-point star) (Table S9). ESMs are comprised of atmospheric and oceanic 3-D primitive equation circulation models, whereas EMICs usually have a less complex atmosphere (e.g., represented by an energy moisture balance model, a statistical-dynamical model or a 3-D quasi-geostrophic circulation model), with varying complexities of the ocean model (Table S9). We additionally distinguish EMICs by the complexity of their ocean

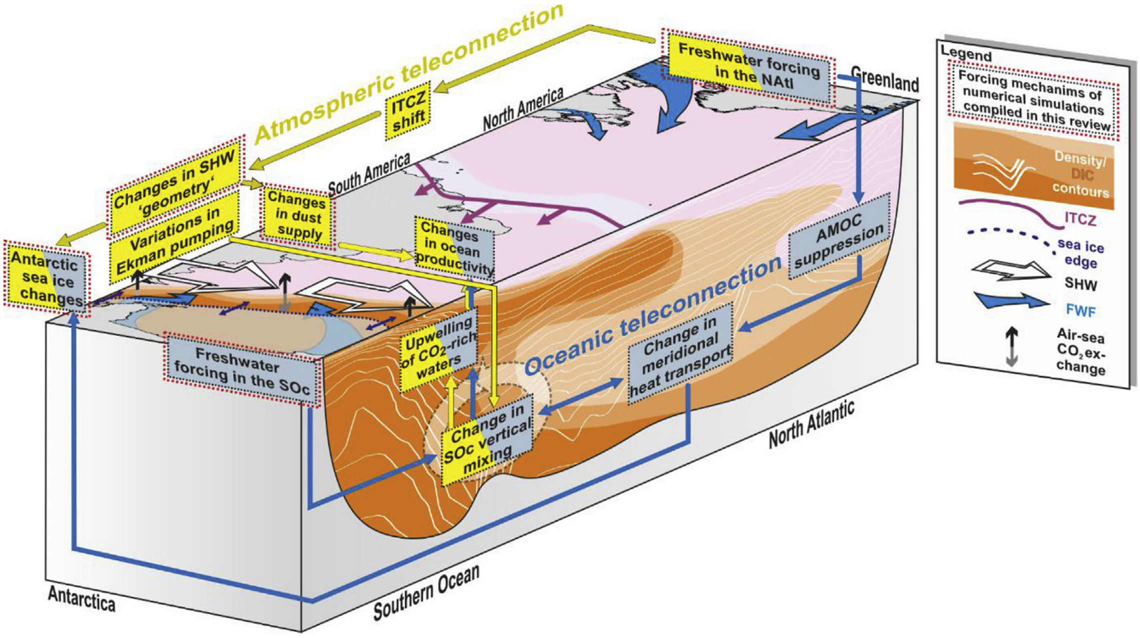

Fig. 2. Atmospheric (yellow) and oceanic link (blue) between North Atlantic climate anomalies and millennial-scale $CO_{2,atm}$ changes illustrated for the Atlantic Ocean and the Atlantic sector of the SOc, following broadly Anderson and Carr (2010). An atmospheric teleconnection between FW-driven AMOC perturbations and the release of CO_2 in the SOc, and hence a $CO_{2,atm}$ increase, was suggested to be driven by a southward ITCZ shift and a poleward SHW strengthening. This might have led to an increase in SOc-to-atmosphere CO_2 fluxes through enhanced Ekman pumping, and adjustments in SOc surface ocean buoyancy forcing, Antarctic sea ice extent and aeolian dust fluxes (e.g., Anderson et al., 2009; Jaccard et al., 2016). An oceanic teleconnection between FW-driven AMOC perturbations and the release of CO_2 in the SOc, leading to a rise in $CO_{2,atm}$, was proposed to be driven by changes in meridional heat transport in the ocean that resulted in enhanced vertical mixing in the SOc and the upwelling of CO_2-rich water masses, reduced Antarctic sea ice cover and changes in surface ocean buoyancy forcing (e.g., Skinner et al., 2010, 2014).

model component (Table S9), i.e., EMICs with simple 2D ocean models (i.e., with 2D friction-geostrophic circulation models), EMICs with simple 3D ocean models (i.e., with 3D friction-geostrophic circulation models) and EMICs with complex 3D ocean models (i.e., with 3D primitive equation circulation models/ OGCM-type). We also differentiate between principal model simulations that impose a single forcing mechanism and sensitivity studies that apply a combination of forcing parameters or adjustments of the background conditions. The model studies compiled here were performed with 22 different numerical models (Table 1; model details and -abbreviations are given in Tables S8 and S9); five of which are box models (*PANDORA* (e.g., Broecker and Peng, 1986), *the* Stephens and Keeling (2000) *box model*, *the* Toggweiler (1999) *box model*, *the* Archer et al. (2003) *3-box model* and *the* Watson et al. (2000) *6-box model*); one is an atmosphere-only general circulation model (AGCM: *NCAR CCM3*); one is a DVM (*LPJ-DGVM*); seven are EMICs (*CLIMBER-2*, *Bern-2.5D*, *Bern-3D*, *MESMO*, *cGENIE*, *LOVECLIM*, *UVic-ESCM*); four are ocean-only GCMs with ocean biogeochemistry (*HAMOCC/LSG*, *GFDL MOM*, *MITgcm*, *COCO*); two are ocean biogeochemistry models (OBGM: *PISCES, NPZD*) with offline tracer transport based on OGCM- or AOGCM output (e.g., from *MIROC*) and two are ESMs (*NCAR CSM1.4-carbon*, *MRI-GCM2*).

In our compilation, we focus on model simulations that are perturbed by six different types of forcing (Tables 1 and 2), representing changes in: i) freshwater forcing (FWF) in the NAtl (17 studies; Table S2) and ii) the SOc (7 studies; Table S3), iii) the strength (18 studies; Table S4) and iv) position of the SHW (8 studies; Table S5) and v) the extent of sea ice in the SOc (9 studies; Table S6), and vi) aeolian dust supply to the ocean (14 studies; Table S7). Although the details of the applied forcing for each type (e.g., magnitude and location) may vary across model simulations (Fig. 3), a comparison of these model simulations is facilitated by common forcing parameters. An overview of simulated $CO_{2,atm}$ change as function of the model hierarchy for each type of forcing is shown in Fig. 4. We exclude model simulations from our compilation that are *forced* by processes generally relevant for $CO_{2,atm}$ change on timescales longer than several millennia, such as continental weathering, variations in the ocean's carbonate chemistry (involving carbonate compensation), mantle degassing, changes in the remineralisation rate of organic matter, or that investigate anthropogenic change. We also omit model simulations of $CO_{2,atm}$ changes that apply time-dependent climate background conditions and forcing parameters (e.g., transient simulations of the last glacial cycle), along with factorial analyses of past $CO_{2,atm}$ change that test a large parameter space for a number of processes and combinations thereof.

In this review, we present and discuss simulated changes in the global ocean- and land carbon cycle and associated $CO_{2,atm}$ variations in numerical models forced by the different parameters listed above (sections 2.1-2.5). We will briefly summarise existing proxy-data evidence that provide the rationale underlying the applied forcings, and point out the typical climatic and hydrographic response of climate models forced with these parameters. We also discuss the capacity of our model compilation to predict realistic $CO_{2,atm}$ change during past millennial-scale climate events by assessing the $CO_{2,atm}$ change in all simulations combined under most realistic forcing parameters. In section 3, we summarise the major findings of this compilation, before providing concluding remarks in section 4.

Table 1

Overview of simulated changes in $CO_{2,atm}$ in numerical models forced by different forcing parameters and run with different climate background conditions. Details on the individual simulations are listed in Tables S2–S7. Information on the models (including an explanation of abbreviations) can be found in Tables S8–S9. Simulated $CO_{2,atm}$ values indicate equilibrium values with respect to the reference state, except for freshwater (FW) hosing experiments. For NAtl hosing experiments, we list simulated $CO_{2,atm}$ change at AMOC minima and at AMOC recoveries/overshoots (*in italics* and parentheses; cf. Fig. 9). For SOc hosing experiments, we report simulated $CO_{2,atm}$ changes at the end of the prescribed FW fluxes (cf. Fig. 11). The following abbreviations are used in this table: freshwater forcing (FWF), Southern Ocean (SOc), North Atlantic (NAtl), Pacific (Pac), eastern Equatorial Pacific (eEqPac), Atlantic Meridional Overturning Circulation (AMOC), Antarctic Bottom Water (AABW), Antarctic Intermediate Water (AAIW), dissolved inorganic carbon (DIC), northern hemisphere (nh), southern hemisphere (sh), model version (v.), and Gent and McWilliams (1990) eddy parameterisation (GM parameterisation). The simulations were performed with interglacial (e.g., Preindustrial – PI, Bølling Allerød – BA) or glacial climate boundary conditions (Heinrich event 1 – H1, Younger Dryas – YD, Last Glacial Maximum – LGM). A more expanded version of this table that additionally outlines the cause of simulated $CO_{2,atm}$ change as proposed in each study can be found in Table S1).

	Reference	Model	Experimental design	Climate background	Model complexity	Simulated $CO_{2,atm}$ change [at AMOC minima *(or at AMOC recoveries)*]
			FWF in the North Atlantic			
1	Marchal et al. (1998)	Bern 2.5D	FWF in the NAtl (32.5–45°N, centered triangle-function) for 1 kyr and rate of 0.38 Sv; sensitivity studies are made by changing the location (20–32.5°N, 45–55°N), duration (250–2500 yr) and rate (0.032–1.5 Sv) of FWF (simultaneous global salt compensation is applied)	modern	EMIC (2D-ocean)	+15 *(+19)* ppm (for “reference” simulation)
2	Marchal et al. (1999)	Bern 2.5D	FWF in the NAtl (32.5–45°N, centered triangle-function) with 0.5 kyr-duration and a rate of 0.44 Sv, to mimic YD-conditions	modern (BA)	EMIC (2D-ocean)	+13 *(+15)* ppm
3	Scholze et al. (2003)	LPJ-DGVM	FWF in the NAtl (Labrador Sea) with max. 0.625 Sv (centered triangle-shape) for 500 yr	YD	DVM (forced with input from AOGCM)	+30 ppm
4	Ewen et al. (2004)	UVic-ESCM v. 2.7	FWF in the NAtl (55–65°N) with different durations (500–1000 yr) and rates (0.015–0.8 Sv)	LGM	EMIC (complex 3D-ocean)	+14 ppm (constant 0.35 Sv, for 500 yrs)
5	Köhler et al. (2005b)	LPJ-DGVM	The LPJ-DGVM was forced with anomalies from FW hosing experiments in the NAtl (50–70°N; 1000 yr, max. 0.5 Sv, centered triangle-function and 0.3 Sv, constant flux) from the ECBILT-CLIO AOGCM. Sensitivity experiments are made with and without CO_2 fertilisation feedback.	Holocene (i.e., 1 and 13 kyr time slice)	DVM (forced with input from AOGCM)	0/+2 *(+7/+13)* ppm with/without CO_2 fertilisation feedback
6	Köhler et al. (2005b)	LPJ-DGVM	In addition to climate anomalies from FWF in the NAtl (50–70°N) over 1000 yr (constant 0.3 Sv flux), LPJ-DGVM was forced with anomalies from time slice simulations with the Hadley Centre model HadSM3 of the past 21 kyr.	LGM (i.e., 17 and 21 kyr time slice)	DVM (forced with input from AOGCM)	+5/+6 *(+2/+3)* ppm with/without CO_2 fertilisation feedback
7	Obata (2007)	MRI-CGCM2	FWF in the NAtl (50–70°N, 65–2°W) with varying duration (3 and 62 yr), FW function and magnitude not specified	PI	ESM	+7 *(−0.5)* ppm (for 62 yr-FWF hosing)
8	Schmittner et al. (2007a)	UVic-ESCM v. 2.7	FWF in the NAtl (0.2 Sv, constant flux, region not further specified) for 500 yr	PI	EMIC (complex 3D-ocean)	+27 ppm
9	Schmittner et al. (2007a)	UVic-ESCM	as in No. 8	Glacial	EMIC (complex 3D-ocean)	+5 ppm
10	Meissner (2007)	UVic-ESCM v.2.8	FW release in the St. Lawrence River Delta (max. 0.12 Sv, step function) for 1000 yr to mimic meltwater discharge from St. Lawrence River	12.9 kyr	EMIC (complex 3D-ocean)	−6 (+7) ppm (Run B)
11	Schmittner and Galbraith (2008)	UVic-ESCM v.2.7	FWF in the NAtl (0.2 Sv, constant flux, region not further specified) with FW extraction after 400, 700, 1100 and 1700 yrs	Glacial	EMIC (complex 3D-ocean)	+21 *(+25)* ppm (for 1700 yrs-long AMOC perturbation)
12	Menviel et al. (2008a)	LOVECLIM	FWF in the NAtl (55–10°W, 50–65°N) for 200 yr with a maximum rate of 2 Sv (centered triangle-function)	PI	EMIC (complex 3D-ocean)	+14 *(−7)* ppm
13	Menviel et al. (2008a)	LOVECLIM	as in No. 12	LGM	EMIC (complex 3D-ocean)	0 *(−7)* ppm
14	Bozbiyik et al. (2011)	NCAR CSM1.4-carbon	FWF in the NAtl (50–70°N) with constant flux of 0.3–1 Sv over 100 years	PI	ESM	+20 *(+20)* ppm (1 Sv-hosing)
15	Bouttes et al. (2012)	CLIMBER-2	FWF in the NAtl (50°N–67.5°N) with different durations (400–1700 yr), different functions (centered triangle- and rectangle-function) and different magnitudes (0.05–2 Sv); simultaneous global salt compensation is applied	PI	EMIC (2D-ocean)	−10 *(+7)* ppm (constant 1 Sv, for 400 yrs)
16	Bouttes et al. (2012)	CLIMBER-2	as in No. 15	LGM	EMIC (2D-ocean)	−10 *(+2)* ppm (constant 1 Sv, for 400 yrs)
17	Bouttes et al. (2012)	CLIMBER-2, plus parametrisation of brine sinking	as in No. 15	LGM+brines	EMIC (2D-ocean)	−1 *(+6)* ppm (constant 1 Sv-hosing for 400 yrs)
18	Huiskamp and Meissner (2012)	UVic-ESCM	FWF in the NAtl (0.12 Sv for 500 yr, exact region not specified) in two equilibrium simulations mimicking H1 conditions (A: forced with present-day winds, B: forced with winds shifted north by	H1	EMIC (complex 3D-ocean)	+0.3 *(+10.2)* ppm (for A) +5.5 *(+15.5)* ppm (for B)

Table 1 (*continued*)

	Reference	Model	Experimental design	Climate background	Model complexity	Simulated $CO_{2,atm}$ change [at AMOC minima *(or at AMOC recoveries)*]
			9°), in combination with FW extraction after FWF and changes in the position of the SHW.			
19	Matsumoto and Yokoyama (2013)	MESMO	FWF in the NAtl (region not specified) with varying magnitude (0.1–0.4 Sv) applied for 1000 years, with salt compensation applied uniformly and globally (outside the NAtl)	PI	EMIC (simple 3D-ocean)	+23 *(+25)* ppm (for 0.4 Sv-hosing)
20	Matsumoto and Yokoyama (2013)	MESMO	FWF in the NAtl (region not specified) with a magnitude of 0.4 Sv applied for 1000 years	LGM	EMIC (simple 3D-ocean)	+9 ppm (for 0.4 Sv-hosing)
21	Menviel et al. (2014)	LOVECLIM v. 1.1 and UVic-ESCM v. 2.9	FWF in the NAtl (55–10°W, 50–65°N) for 1000 yr (constant 0.2 Sv) with and without parallel global and regional (SOc, NPac, eEqPac) salt compensation and subsequent FW extraction (constant 0.2 Sv) for 1000 yr.	LGM	EMIC (complex 3D-ocean)	−5/−7 ppm in LOVECLIM/UVic (0.2 Sv-hosing, for 1000 years, without salt compensation)
22	Schmittner and Lund (2015)	UVic-ESCM v. 2.9	FWF in the NAtl (45–65°N, 60–0°W) with magnitudes between 0.05 and 0.2 Sv (constant flux)	PI	EMIC (complex 3D-ocean)	+23 ppm (for 0.2 Sv FWF)
23	Menviel et al. (2015a)	LOVECLIM, Bern-3D	FWF in the NAtl (55–11°W, 50–65°N) with a magnitude of 0.05 and 0.1 Sv (LOVECLIM), as well as 0.07 and 0.25 Sv (Bern-3D) for 1000 yr. Carbon fluxes between the land and the atmopshere are held constant.	PI	EMIC (complex and simple 3D-ocean)	−11.5/−15 ppm (for 0.1/0.25 Sv-hosing in LOVECLIM/Bern-3D)
			FWF in the Southern Ocean			
24	Marchal et al. (1998)	Bern-2.5D	FW hosing (centered triangle-shaped) in the SOc (62.5–70°S) with 1 kyr-duration and rate of 0.38 Sv, with simultaneous global salt compensation	modern	EMIC (2D-ocean)	−7 ppm
25	Ewen et al. (2004)	UVic-ESCM	FW hosing in the SOc (in modern AAIW formation area south of South America) for 500 yr with magnitude of 0.3 and 1 Sv, in combination with variations in initial $CO_{2,atm}$ concentrations and the AMOC strength	LGM	EMIC (complex 3D-ocean)	+10.5 ppm (for LGM climate conditions, and gradually increasing FWF)
26	Ewen et al. (2004)	UVic-ESCM	as in No. 25	PI	EMIC (complex 3D-ocean)	+42 to +48 ppm
27	Tagliabue et al. (2009b)	OBGM-PISCES	PISCES is forced offline by a variety of LGM circulation schemes (obtained from the fully coupled IPSL model that was forced with FW hosing in different regions and with different magnitudes, not further specified).	LGM	OBGM (with offline tracer transport based on OGCM)	−3.5 ppm (in scenario that reproduces LGM $\delta^{13}C_{DIC}$ best)
28	Menviel et al. (2010)	LOVECLIM v.1.1	FW hosing in the SOc (163°E–11°E, 70–80°S) with magnitude/duration of 0.2 Sv/800 years (constant flux) and 0.35 Sv/400 years (centered triangle function)	PI	EMIC (complex 3D-ocean)	+2.5 ppm (for 400 yr-simulation)
29	Bozbiyik et al. (2011)	NCAR CSM1.4-carbon	FWF flux in the SOc (Weddell Sea and Ross Sea; 1 Sv) for 100 years	PI	ESM	−8/−9 ppm (FWF in Weddell/Ross Sea)
30	Bouttes et al. (2012)	CLIMBER-2	FWF in the SOc (60–75°S) with varying magnitude (0.05–1 Sv) and a duration of 400 yr, with simultaneous global salt compensation	LGM	EMIC (2D-ocean)	−11 ppm (for 1 Sv-FWF)
31	Bouttes et al. (2012)	CLIMBER-2	as in No. 30, plus parametrisation of brine formation beneath sea ice	LGM+brines	EMIC (2D-ocean)	−5 ppm (for 1 Sv-FWF)
32	Menviel et al. (2015a)	LOVECLIM, Bern-3D	FWF in the SOc (50–62°S, 0–280°E) with a magnitude of 0.1 Sv (LOVECLIM) and 0.2 Sv (Bern-3D) for an unspecified duration. Carbon fluxes between the land and the atmopshere are held constant.	PI	EMIC (complex and simple 3D-ocean)	−9/−12 ppm (for 0.1/0.2 Sv-hosing in LOVECLIM/Bern-3D)
			Changes in the intensity of the SHW wind stress			
33	Winguth et al. (1999)	HAMOCC3/LSG	Changes in the zonal SHW wind stress between 30 and 70°S were made by 1.5x.	LGM	OGCM with ocean biogeochemistry	+7 ppm (for 1.5x scenario)
34	Toggweiler et al. (2006)	GFDL MOM v. 3	Changes in the zonal SHW wind stress between 35 and 75°S were made by 0.5x to 3x to represent latitudinal westerly shifts.	modern	OGCM with ocean biogeochemistry	+35 ppm (for 1.5x scenario)
35	Parekh et al. (2006b)	MITgcm	Changes in SHW wind strength by 0.5x and 1.5x were made in the southern hemisphere (exact region unspecified), in combination with dust fluxes according to LGM estimates (3.5% Fe, 1% Fe solubility).	PI	OGCM with ocean biogeochemistry	+25 ppm (for 1.5x scenario) −31 ppm (for 0.5x scenario)
36	Schmittner et al. (2007a)	UVic-ESCM	Zonal wind stress was changed by 0.5x and 2x (everywhere).	PI	EMIC (complex 3D-ocean)	+85 ppm (for 2x scenario) −25 ppm (for 0.5x scenario)
37		LOVECLIM		PI		

(*continued on next page*)

Table 1 (*continued*)

	Reference	Model	Experimental design	Climate background	Model complexity	Simulated $CO_{2,atm}$ change [at AMOC minima *(or at AMOC recoveries)*]
	Menviel et al. (2008b)		Atmospheric wind velocities (at 10 m) were changed by 0.85x and 1.15x between 40 and 60°S. Model simulation with abiotic ocean (with prescribed phosphate field) was also performed.		EMIC (complex 3D-ocean)	+5 ppm (for 1.22x scenario) −5 ppm (for 0.67x scenario)
38	Tschumi et al. (2008)	Bern-3D	Changes in zonal wind stress by 0.25x, 0.5x, 0.75x, 2x and 3x were made between 30 and 70°S, and run with different model setups.	PI	EMIC (simple 3D-ocean)	+11 ppm (for 1.5x standard scenario) −3 ppm (for 0.5x standard scenario)
39	Marinov et al. (2008b, 2008a)	GFDL MOM v. 3 and Princeton model (P2A)	Changes in the intensity of the SHW by 0.5x, 2x and 3x were made south of 30°S.	PI	OGCM with ocean biogeochemistry	+36 ppm (for 2x scenario) −5 ppm (for 0.5x scenario)
40	d'Orgeville et al. (2010)	UVic-ESCM v. 2.8	Changes in the intensity of the SHW by 0.5x and 2x were made between 30 and 70°S.	Interglacial	EMIC (complex 3D-ocean)	+36 ppm (for 2x scenario) −20 ppm (for 0.5x scenario)
41	Tschumi et al. (2011)	Bern-3D	Changes in SHW wind strength (zonal and meridional wind stress) by 0.2x, 0.4x, 0.6x, 0.8x, 1x, 1.2x, 1.4x, 1.6x and 1.8x were made south of 51°S, considering active and inactive ocean-sediment interaction in the model.	PI	EMIC (simple 3D-ocean)	+16 ppm (for 1.6x scenario, ocean-only model) −25 ppm (for 0.4x scenario, ocean-only model)
42	Lee et al. (2011)	NCAR CCM3 v. 3.6 and MESMO v. 1.0	Cooling of the NAtl mixed layer is prescribed by a uniform cooling flux term north of 25°N of various magnitudes (in CCM3). Through an atmospheric teleconnection, this increases the SHW wind intensity by 1.25x. Wind field anomalies of CCM3 are used off-line to force MESMO.	modern with LGM land-mask	AGCM, EMIC (simple 3D-ocean)	+21 ppm (with responsive biology) +58 ppm (with constant biology)
43	Lauderdale et al. (2013)	MITgcm in global ocean configuration	Changes in SHW zonal wind stress by 0.5x and 1.5x were made between 30 and 70°S, in combination with changes in eddy parameterisation, surface buoyancy boundary conditions and nh westerlies.	PI	OGCM with ocean biogeochemistry	+16 ppm (for 1.5x scenario) −16 ppm (for 0.5x scenario)
44	Munday et al. (2014)	MITgcm in eddy-permitting sector configuration	The zonal wind stress of the SHW between 30 and 60°S was multiplied by a factor of 0–5 in sector model configuration with a grid spacing of 2° (GM eddy parameterisation) and 0.5° (no eddy parameterisation, mesoscale eddy-permitting).	PI	OGCM with ocean biogeochemistry	+7 to +21 ppm (for 1.5x scenario) −4 to −19 ppm (for 0.5x scenario)
45	Huiskamp et al. (2015)	UVic-ESCM v. 2.9	Changes in the SHW wind strength (zonal and meridional) were made by 0.8x and 1.2x between 25 and 90°S.	PI	EMIC (complex 3D-ocean)	+6 ppm (for 1.2x scenario) −4 ppm (for 0.8x scenario)
46	Menviel et al. (2015a)	LOVECLIM	Changes in the SHW wind stress were made by 0.7x and 1.35x between 34 and 60°S. Carbon fluxes between the land and the atmosphere are held constant.	PI	EMIC (complex 3D-ocean)	+11 ppm (for 1.35x scenario) −3.5 ppm (for 0.7x scenario)
47	Lauderdale et al. (2017)	MITgcm in global ocean (as in No. 43) and in sector configuration (as in No. 44)	Changes in the SHW zonal wind stress by 0.5x and 1.5x were made in the SOc (exact area not specified) in global-ocean simulations with varying eddy parameterisation, and in sector model.	PI	OGCM with ocean biogeochemistry	+16 ppm (for 1.5x standard scenario) −16 ppm (for 0.5x standard scenario)
48	Menviel et al. (2018)	Eddy-permitting global ocean, sea ice model MOM5	A 15% increase in the 10 m wind speed (corresponds to 33% increase in wind stress) *and* a 4° southward shift of the SHW were prescribed.	PI	OGCM with ocean biogeochemistry	+20 ppm
49	Ödalen et al. (2018)	cGENIE	Wind stress was changed by 0.5x and 2x (everywhere).	PI	EMIC (simple 3D-ocean)	+47 ppm (for 2x scenario) −33 ppm (for 0.5x scenario)
			Changes in the latitudinal position of the SHW			
50	Tschumi et al. (2008)	Bern-3D	Changes in the position of the SHW by −5° and by +10° in latitude were made with 1° increments and run with different model setups (different boundary conditions, diapycnal mixing strengths, AMOC overturning rates and efficiency of the ocean carbon pumps).	PI	EMIC (simple 3D-ocean)	−3 ppm (for −5° standard scenario) +9 ppm (for +5° standard scenario)
51	d'Orgeville et al. (2010)	UVic-ESCM	Changes in the position of the SHW by −7.2° and 7.2° in latitude were made.	Interglacial	EMIC (complex 3D-ocean)	−0.5 ppm (for −7.2° scenario) −2.5 ppm (for +7.2° scenario)
52	Huiskamp and Meissner (2012)	UVic-ESCM	Changes in the position of the SHW by −9° and −18° in latitude were made in two equilibrium simulations mimicking H1 conditions (A: forced with present-day winds, B: forced with winds shifted north by 9°), in combination with FWF (0.12 Sv for 500 yr) and salt addition in the NAtl.	H1	EMIC (complex 3D-ocean)	−0.5 ppm (for −9° scenario and background climate A) −8.7 ppm (for −9° scenario and background climate B)
53		MITgcm		LGM		

Table 1 (*continued*)

	Reference	Model	Experimental design	Climate background	Model complexity	Simulated $CO_{2,atm}$ change [at AMOC minima *(or at AMOC recoveries)*]
	Völker and Köhler (2013)		Changes to the position of the SHW by ±5° and ±10° were applied between 25 and 65°S. The LGM simulation is forced with atmospheric anomaly fields from coupled atmosphere-ocean simulations with the COSMOS model.		OGCM with ocean biogeochemistry	+3 ppm (for +10° scenario) +9 ppm (for −10° scenario)
54	Lauderdale et al. (2013)	MITgcm	Changes to the position of the SHW were made by ±3° and ±10° in latitude, and combined with changes in sh and nh westerly wind intensity, and in surface buoyancy boundary conditions.	PI	OGCM with ocean biogeochemistry	+10 ppm (for +10° scenario) −10 ppm (for −10° scenario)
55	Huiskamp et al. (2015)	UVic-ESCM	Changes to the position of the SHW (29–90°S) were made by ±1.8°, ±3.6 and ± 5.4°, in combination with intensity changes.	PI	EMIC (complex 3D-ocean)	+12 ppm (for +5.4° scenario)–10 ppm for (−5.4°scenario)
56	Lauderdale et al. (2017)	MITgcm	Changes to the position of the SHW were made by ±10°, in combination with variations of the SHW wind stress, both in global-ocean simulations with varying eddy parameterisation and in sector model configuration.	PI	OGCM with ocean biogeochemistry	+10 ppm (for +10° scenario) −9 ppm (for −10° scenario)
			Antarctic sea ice changes			
57	Stephens and Keeling (2000)	Biogeochemical 7-box ocean model	The ice free surface area south of the APF (i.e., in the AABW formation box and Antarctic surface box) is varied between 0 and 16 10^{12} m^2.	modern	Box	−67 ppm (for best guess glacial scenario)
58	Morales Maqueda and Rahmstorf (2002)	Coupled thermodynamic-dynamic sea ice-upper ocean model	12 sensitivity experiments with changes in annual mean air temperatures [−5 °C;-20 °C] and wind velocities [0x, 0.5x, 0.75x] to estimate glacial sea ice extent and derive associated $CO_{2,atm}$ changes according to No. 57	PI	OGCM (sea ice extent simulations)	−35 ppm (for best guess LGM scenario)
59	Archer et al. (2003)	CLIMBER-2, Bern 2-D, HAMOCC2, POP, box models of Stephens and Keeling (2000) and Toggweiler (1999), 3-box model and PANDORA	A permanent sea ice cap is implemented south of 55°S by inhibiting air-sea gas exchange.	modern	Box, EMIC, GCM	−33 to −53 ppm (Stephens and Keeling and Toggweiler model) −1 to −7 ppm (other box models) −3 to +5 ppm (GCMs)
60	Kurahashi-Nakamura et al. (2007)	COCO v. 3.4	Fractional sea ice cover (0–100%) and the location of the sea ice edge (40°S-56°S) were adjusted, in combination with reductions in air-sea CO_2 fluxes (“ventilation”) and export production (“biological pump”) in sea ice regions. Feedbacks between ocean physics and sea ice, and seasonality are not included.	PI	OGCM with ocean biogeochemistry	+10 ppm (for 100% sea ice cover, and reduced ventilation and bio pump-scenario) −6 ppm (for 100% sea ice cover, and reduced ventilation-scenario)
61	Tschumi et al. (2008)	Bern-3D	Changes in the air-sea gas exchange in the SOc were made in sea ice-covered regions during the LGM, also in combination with changes in wind stress intensity and other parameters.	PI	EMIC (simple 3D-ocean)	+5 ppm (with respect to 0.5x wind stress-scenario)
62	Bouttes et al. (2010)	CLIMBER-2	Different parameterisation of brine formation and deep water mass sinking were made in combination with decreases in vertical ocean diffusivities.	LGM	EMIC (2D-ocean)	−52 ppm (for standard LGM minus all salt in brines-scenario)
63	Sun and Matsumoto (2010)	MESMO v. 1.0	Changes in polar sea ice extent are simulated by modifying the sea ice albedo from 0 (perfect adsorption) to 1 (perfect reflection).	modern	EMIC (simple 3D-ocean)	+6 ppm (for sea ice albedo of 0.4 "warm mode") −9.4 ppm (for sea ice albedo of 0.77 "cold mode")
64	Bouttes et al. (2011)	CLIMBER-2	Sensitivity simulations with changes in brine sinking parameter, in combination with changes in iron fertilisation and vertical diffusivity	LGM	EMIC (2D-ocean)	−42 ppm
65	Chikamoto et al. (2012a)	OBGM forced offline with output from MIROC v.3.2	Pre-industrial simulations are run with LGM Antarctic sea ice extent.	PI	OBGM (with offline tracer transport based on OGCM)	−3 ppm (for “a” simulation)
66	Chikamoto et al. (2012a)	as in No. 65	Glacial simulations are run with PI Antarctic sea ice extent.	LGM	OBGM (with offline tracer transport based on OGCM)	−3.9 ppm (for “a” simulation)
			Changes in the supply of aeolian dust to the ocean			
67	Lefèvre and Watson (1999); Watson and Lefèvre (1999)	PANDORA: reservoir-flux 10-box ocean model including biogeochemistry and Fe cycling	Aeolian dust input to the SOc and the global ocean was changed by 20x and 2–10x the modern value, respectively.	modern	Box	−10 and −23 ppm (for increased dust supply everywhere) −1 ppm (for scenario with dust supply in SOc)

(*continued on next page*)

Table 1 (*continued*)

	Reference	Model	Experimental design	Climate background	Model complexity	Simulated $CO_{2,atm}$ change [at AMOC minima *(or at AMOC recoveries)*]
68	Lefèvre and Watson (1999); Watson and Lefèvre (1999)	PANDORA as in No. 67	as in No. 67, but combined with glacial ocean chemistry and reduced SOc upwelling (to mimic glacial conditions).	LGM	Box	−12 and −24 ppm (for increased dust supply everywhere) −3 ppm (for scenario with dust supply in SOc)
69	Watson et al. (2000)	CYCLOPS-like box model, with simple representation of ecosystem dynamics	Aeolian dust input to the SOc is varied over time, with the magnitude scaled to the Vostok dust record.	modern	Box	−40 ppm (for glacial increase in dust supply)
70	Bopp et al. (2003)	OGCM-PISCES	Aeolian dust input to the global ocean was increased according to LGM model estimates (1.75x).	PI	OBGM (with offline tracer transport based on OGCM)	−15 ppm
71	Bopp et al. (2003)	OGCM-PISCES as in No. 70	as in No. 70, but with LGM SST and SST fields, -ocean circulation and -sea ice.	LGM	OBGM (with offline tracer transport based on OGCM)	−32 ppm
72	Ridgwell (2003)	similar to No. 69	Aeolian dust input to the global ocean was modified by a factor of 1–3.5 (assuming that the dust scaling factor *f* for the LGM equals 1.75 as in No. 70)	PI	Box	−38 ppm (for glacial increase in dust supply)
73	Parekh et al. (2006a, 2006b)	MITgcm (global configuration)	Aeolian dust input to the global ocean was modified by a factor of 0–5.5 (the latter represents LGM model estimates).	PI	OGCM with ocean biogeochemistry	−8 ppm (for 5.5x modern-scenario) +94 ppm (for 0.1x modern-scenario)
74	Parekh et al. (2006b)	as in No. 73	LGM dust fields as in No. 73 but with doubled ligand concentrations (2 nM)	PI	OGCM with ocean biogeochemistry	~−22 ppm
75	Parekh et al. (2008)	Bern-3D	Increased dust input is applied to 8 different ocean regions (100x increase for 1000 years), and in the SOc with different loading factors (2–100).	PI	EMIC (simple 3D-ocean)	−10 ppm (for globally increased dust fluxes)
76	Parekh et al. (2008)	as in No. 75	as in No. 75 but with adjustments of ligand concentrations and -strength in the ocean.	PI	EMIC (simple 3D-ocean)	−10 ppm (doubled ligand concentration) −8 ppm (increased ligand strength)
77	Tagliabue et al. (2009a)	OGCM-PISCES as in No. 27	as in No. 27, but in combination with aeolian dust input to the global ocean according to LGM model estimates and changes in the C/N stoichiometry of phytoplankton.	PI	OBGM (with offline tracer transport based on OGCM)	−11 ppm (LGM-dust scenario)
78	Oka et al. (2011)	COCO	Aeolian dust input to the global ocean was increased according to LGM model estimates. Sensitivity studies are made on regional dust impacts.	PI	ESM	−14.6 ppm (LGM-dust scenario)
79	Bouttes et al. (2011)	CLIMBER-2 as in No. 62	Sensitivity simulations with changes in iron fertilisation (through subpolar nutrient utilisation efficiency), in combination with changes in brine sinking and vertical diffusivity	LGM	EMIC (2D-ocean)	−10 to −21 ppm
80	Tagliabue et al. (2014a)	NEMO-PISCES v.3.5	Aeolian dust sources to the global ocean (as predicted by the from the INCA and National Center for Atmospheric Research (NCAR) models) were eliminated.	PI	OBGM (with offline tracer transport based on OGCM)	+1.8 to +2.3 ppm
81	Tagliabue et al. (2014a)	as in No. 80	Adjustments of ligand concentrations were made without changes to aeolian dust supply.	PI	OBGM (with offline tracer transport based on OGCM)	−5.4/+5.1 ppm (doubled/halved ligand concentration)
82	Watson et al. (2015)	2D ocean circulation model coupled to simple biogeochemical scheme	Different buoyancy forcings are applied in the southern channel (by specifying surface-atmosphere buoyancy fluxes), to mimic glacial, modern and intermediate-climate conditions, in combination with halving the biological response time to Fe supply (from 1 yr to 6 m).	modern	EMIC (2D-ocean)	−20 to −50 ppm
83	Lambert et al. (2015)	NEMO-PISCES	The model was forced by extended versions of DIRTMAP, i.e., global-ocean dust fluxes during the Holocene and LGM	PI	OBGM (with offline tracer transport based on OGCM)	<10 ppm (LGM-Holocene)

Table 2

Overview of simulated changes in $CO_{2,atm}$ across numerical models run under interglacial (IG) and glacial (G) climate boundary conditions and forced by different forcing mechanisms. Minima, maxima and percentile ranges of the simulated $CO_{2,atm}$ values are based on principal model simulations only, which may differ in the experimental setup and the model complexity. For NAtl hosing experiments, the reported values refer to the simulated $CO_{2,atm}$ changes at AMOC minima and during the AMOC recovery/-overshoot (*in italics* and in parentheses; cf. Fig. 9). For SOc hosing experiments, we report simulated $CO_{2,atm}$ changes at the end of the prescribed FW fluxes (cf. Fig. 11; excluding Ewen et al., 2004). In all other instances, simulated $CO_{2,atm}$ values indicate equilibrium values after the imposed forcing with respect to the initial/reference state. Arrows illustrate the general trend of simulated $CO_{2,atm}$ change for a particular forcing, with ↔ indicating both a rise (↑) and drop (↓). We have quantified these trends, where possible, but some restrictions apply: [a]only EMICs and positive $CO_{2,atm}$ change considered, [b]linear approximation for $f = 1–2$, [c]linear approximation for $f = 0.5–1$, [d]linear approximation including all model data, [e]box model results of Ridgwell (2003) for $f_{global} = 1–1.5$, [f]box model results of Lefèvre and Watson (1999) for $f_{global} = 1–2$, and [g]GCM and ESM results for $f_{global} = 1–2$.

Forcing	Climate background	# Principal simulations	Simulated $\Delta CO_{2,atm}$ (ppm)						Sources of uncertainties, biases and unresolved issues
			Minimum	Maximum	25%-percentile	75%-percentile	Principal trend	Change per unit forcing	
NAtl FWF	IG	34 *(26)*	−15 *(−8)*	27 *(25)*	−7 *(1)*	14 *(14)*	↔ *(↑)*	0.4 ± 0.3 per 100 yr stadial duration (very low confidence, $p = 0.2$)[a]	• Nature of ocean response (in different regions) • Nature and timing of terrestrial biosphere carbon changes (soil versus land vegetation) • Response of the hydrological cycle (specifically precipitation changes) • Atmospheric circulation changes • Initial conditions (AMOC background, state of the North Pacific halocline, etc.) • Magnitude of meltwater release into the NAtl in the past
	G	50 *(36)*	−10 *(−7)*	24 *(25)*	−5 *(0)*	6 *(7)*	↔ *(↑)*	0.4 ± 0.2 per 100 yr stadial duration (low confidence, $p = 0.07$)[a]	
SOc FWF	IG	6	−12	2.5	−9	−7	↓	−1.7 ± 1.2 per 10^6 km^3 of FW added (low confidence, $p = 0.2$)	• Nature of terrestrial biosphere carbon changes • Marine ecosystem response • Influence of sea ice changes • Hydrological cycle (specifically precipitation changes) • Timing and magnitude of meltwater release from Antarctica in the past
	G	15	−11	0	−4	−2	↓	−0.6 ± 0.1 per 10^6 km^3 of FW added ($p < 0.05$)	
SHW wind intensity increase	IG	29	3	95	11	38	↑	3.2 ± 1.6 per 10% intensity change[b] ($p < 0.05$)	• Compensating effects through mesoscale eddy activity • Compensating effects through ocean productivity changes • Constant thickness diffusivities • Feedbacks on Antarctic sea ice extent • Feedbacks on mode and location of AABW formation • Response under (mild-) glacial boundary conditions • Nature of past changes in SHW intensity over millennial timescales
	G	1	7	7	7	7	↑	–	
SHW wind intensity decrease	IG	23	−70	−2	−26	−4	↓	−3.7 ± 1.5 per 10% intensity change[c] ($p < 0.05$)	
	G	–	–	–	–	–	–	–	
Northward shift of SHW	IG	18	−3	17	7	12	↑	0.9 ± 0.4 per 1° northward shift[d] ($p < 0.05$)	• As above • Nature of past changes in the latitudinal position of the SHW over millennial timescales
	G	2	1	3	1	2	↑	–	
Southward shift of SHW	IG	13	−10	1	−9	−2	↓	−0.6 ± 0.4 per 1° southward shift[d] ($p < 0.05$)	
	G	5	−15	9	−9	7	↔	–	
Antarctic sea ice expansion	IG	70	−71	26	−15	0	↓	–	• Role of brine formation and feedback on deep-ocean salinity and vertical diffusivities • Feedbacks on the position of the SHW • Feedbacks on mode and location of AABW formation • Role of other limiting factors on marine biology (light, nutrients) • Nature of past Antarctic sea ice changes on millennial timescales
	G	15	−52	−4	−47	−20	↓	–	
Antarctic sea ice retreat	IG	7	2	6	3	5	↑	–	
	G	1	4	4	4	4	↑	–	
Increased aeolian dust fluxes	IG	36	−50	−2	−43	−19	↓	−66 ± 17[e], −17 ± 11[f], −8±7[g] (per doubling in aeolian dust fluxes, $p < 0.05$)	• Non-aeolian sources of iron to the surface ocean • Drivers and influence of changes in ligand abundances (i.e., bioavailability) • Fe solubility of dust in the ocean • Role of silicic acid leakage in the SOc • Compensating effects through productivity changes in the equatorial region • Nature of past changes in aeolian dust fluxes to the ocean on millennial timescales
	G	5	−32	−8	−29	−16	↓	–	
Decreased aeolian dust fluxes	IG	5	2	181	55	138	↑	–	
	G	–	–	–	–	–	–	–	

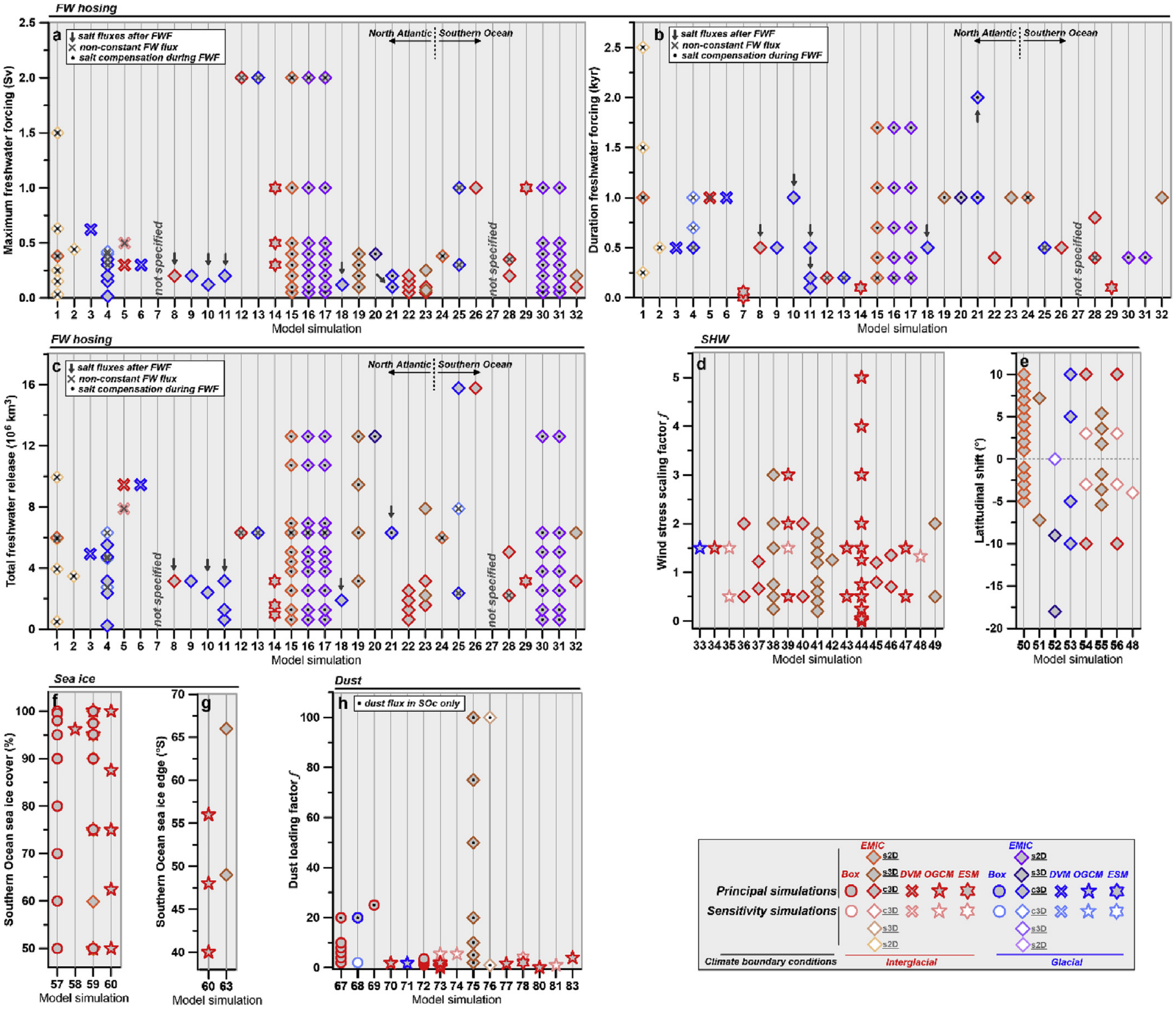

Fig. 3. Overview of forcing parameters. (a) Maximum magnitude, (b) duration and (c) total (time-integrated) amount of FW hosing in the NAtl and in the SOc, changes in the (d) intensity and (e) latitudinal position of the SHW, changes in (f) the fractional sea ice cover in the SOc south of ~55°S and (g) the mean latitudinal position of the sea ice edge in the SOc, and (h) changes in the supply of aeolian dust to the SOc (black dots in symbols) and to the global ocean. Grey symbols show principal model simulations, whereas white symbols show sensitivity experiments that apply a combination of different forcings or different background conditions. Symbol colour indicates interglacial (reddish) and glacial (blueish) climate boundary conditions applied in the simulations. The model types are categorised as box models (circles), DVMs (crosses), EMICs (diamonds), ocean-only GCMs with biogeochemistry (pentagons), and ESMs (hexagons), cf. Tables S8 and S9. EMICs are further classified by the complexity of their ocean model (orange: simple 2D ocean model (s2D), brown: simple 3D ocean model (s3D) and red: complex 3D ocean (c3D)). In (a) to (c), arrows point at FW hosing simulations that apply salt fluxes after cessation of freshwater forcing (FWF) in order to encourage an AMOC recovery. Crosses show simulations that use gradually increasing or centered-triangle shaped FW fluxes, all others apply constant FW fluxes. Black dots highlight hosing experiments that apply global or regional salt compensation at the time of hosing (in order to maintain a constant global-ocean salinity). References and further details on all model simulations can be found in Tables 1, 2, and S1-S7.

2. Millennial-scale $CO_{2,atm}$ changes simulated in coupled carbon cycle-climate models

2.1. Freshwater forcing in the North Atlantic

2.1.1. Proxy data constraints on variable FW supply to the NAtl

Abrupt changes in surface ocean- and air temperatures as well as in precipitation patterns have been reported throughout the northern hemisphere (e.g., Clement and Peterson, 2008; Voelker et al., 2002), and were first described as Dansgaard-Oeschger (D-O) cycles in Greenland ice cores (Dansgaard et al., 1982, 1984; NGRIP members, 2004). In the NAtl, this distinct climate variability, occurring primarily during glacial periods, was linked with perturbations of the AMOC (e.g., Broecker et al., 1985; Keigwin and Jones, 1994; McManus et al., 2004; Böhm et al., 2015; Lynch-Stieglitz, 2017; see also Stocker, 2000; Rahmstorf, 2002). Specifically, there is consistent evidence for a weakening and shoaling of the AMOC during H events (e.g., Lynch-Stieglitz et al., 2014; Schmittner and Lund, 2015; Lynch-Stieglitz, 2017). In addition, high-resolution proxy data support the existence of fast AMOC changes during weaker and shorter stadials (Kissel et al., 1999; Gottschalk et al., 2015; Henry et al., 2016; Waelbroeck et al., 2018), and support previous lower-resolution water mass- and overturning proxy-reconstructions (Charles et al., 1996; Keigwin and

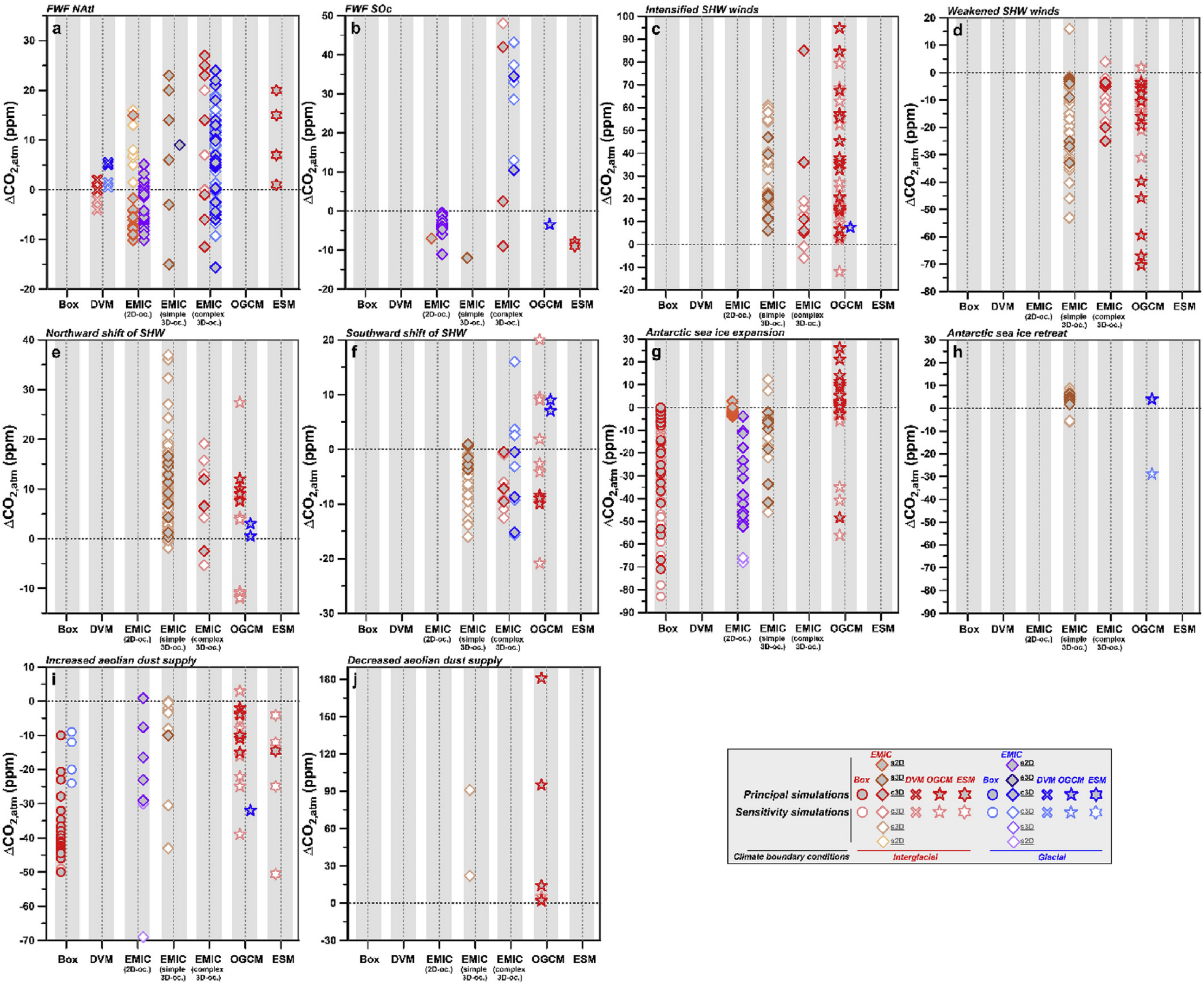

Fig. 4. Overview of simulated $CO_{2,atm}$ response to different types of forcing applied in coupled carbon cycle-climate models. (a) FWF in the NAtl ($CO_{2,atm}$ changes refer to those simulated at AMOC minima), (b) FWF in the SOc ($CO_{2,atm}$ values are those simulated at the end of the prescribed FW fluxes), (c) increased and (d) decreased intensity of the SHW winds, (e) northward and (f) southward shifts of the SHW, (g) expansion and (h) retreat of SOc sea ice, as well as (i) enhanced and (j) diminished iron fertilisation in the global or SOc. Simulated $CO_{2,atm}$ values in (c) to (j) indicate differences in simulated equilibrium values with respect to the reference state. Note that DVMs (crosses) specifically investigate the response of the land biosphere to FWF (while the ocean is a buffer). OGCM assess the ocean response to FWF (while neglecting any contribution from the land biosphere). EMICs and ESMs assess changes in both carbon reservoirs (unless the interaction of the land biosphere is disabled, e.g., Menviel et al., 2015a). Symbols are shown as in Fig. 3. References and further details on all model simulations can be found in Tables 1, 2, andTables S1-S7.

Boyle, 1999; Elliot et al., 2002).

A variety of complex cryosphere-ocean interactions (Alvarez-Solas et al., 2010; Marcott et al., 2011; Dokken et al., 2013; Pedro et al., 2018) as well as self-sustaining mechanisms (Peltier and Vettoretti, 2014; Li and Born, 2019) have been proposed as drivers of D-O cycles and the bipolar seesaw involving distinct AMOC variability. In numerical model simulations, AMOC changes are generally considered to result from melt-/freshwater supply to major NAtl deep convection sites (e.g., Bond et al., 1992b; Broecker, 1994; Grousset et al., 2000). This is supported by increased fluxes of ice-rafted detritus (IRD), an indicator for increased iceberg discharge from ice sheets, and hence FW supply to the ocean, found in NAtl sediment cores during H events (e.g., Heinrich, 1988; Bond et al., 1993; Hemming, 2004), with lower-amplitude fluxes also observed during short and weak D-O cycles (e.g., Bond and Lotti, 1995; Elliot et al., 2002). Evidence for parallel sea surface freshening (e.g., Bond et al., 1992a; Hillaire-Marcel and Bilodeau, 2000) and a near-cessation of the southward export of NAtl Deep Water (NADW) (e.g., Praetorius et al., 2008; Böhm et al., 2015; Henry et al., 2016) supports the contention of a tight link between northern-hemisphere climate anomalies and perturbations of the AMOC. Geochemical proxies (Hemming, 2004) and isotope-enabled EMIC simulations (Roche et al., 2004) respectively suggest a duration and magnitude of FW fluxes during H event 1 and 4 of 0.15–0.3 Sv for 500 years, and 0.25–0.3 Sv over 100–400 years, which is likely an upper limit of FW fluxes into the NAtl during stadials.

2.1.2. Physical response of climate models to NAtl FWF

Physics-only climate model simulations have highlighted the non-linear response of the AMOC to prescribed FW fluxes in the NAtl (Manabe and Stouffer, 1988, 1995) and the existence of multiple stable AMOC states for a given forcing (e.g., Stommel, 1961; Bryan, 1986; Marotzke and Willebrand, 1991; Stocker and Wright, 1991; Mikolajewicz and Maier-Reimer, 1994). The AMOC strength can change abruptly between two stable states in a defined range of FWF (e.g., Stocker and Wright, 1991; Rahmstorf, 2002; Rahmstorf et al., 2005). This hysteresis behaviour is, however, strongly determined by the initial state of the AMOC prior to FWF, indicating its sensitivity to perturbations (i.e., its 'proximity' to transition) (e.g., Stocker and Marchal, 2000; Rahmstorf et al., 2005). In addition, the sensitivity of the AMOC to surface buoyancy forcing was shown to depend on climate boundary conditions (e.g., Ganopolski and Rahmstorf, 2001; Schmittner et al., 2002; Kageyama et al., 2010), the model resolution (e.g., Spence et al., 2013; Gent, 2018) and ocean diffusivities (e.g., Schmittner and Weaver, 2001; Prange et al., 2003).

Most climate models consistently simulate a reduction of the AMOC as a result of FW input into the NAtl, despite differences in the location, rates and durations of prescribed FWF. For example, a mean reduction in the AMOC by 30% after 100 years is simulated by AOGCMs and EMICs forced by a 0.1 Sv-FW perturbation (Stouffer et al., 2006). However, the timescale of the AMOC recovery and the existence of AMOC overshoots is model-dependent (Stouffer et al., 2006). After FWF cessation, the AMOC in some models remains perturbed (e.g., Manabe and Stouffer, 1988; Rind et al., 2001a), while in others it returns to near-initial conditions; in some cases exhibiting an AMOC overshoot (e.g., Vellinga et al., 2002). Again, this is crucially dependent on the initial AMOC state with respect to the hysteresis structure of the model, which determines the (ir)reversibility of the perturbation (Stocker and Marchal, 2000).

FW hosing in the NAtl causes generally abrupt cooling in the northern hemisphere and a southward shift of the Intertropical Convergence Zone (ITCZ) (e.g., Zhang and Delworth, 2005; Stouffer et al., 2006; Kageyama et al., 2010, 2013). Simulated temperature- and precipitation changes differ in amplitude and regional extent (Vellinga and Wood, 2002; Stouffer et al., 2006; Kageyama et al., 2010, 2013). The simulated southern-hemisphere air temperature change is often confined to ~1.5 °C, which is mostly smaller than observed in ice cores (~1–4 °C) (Kageyama et al., 2013; Pedro et al., 2018). Kageyama et al. (2013) also pointed out that only those FW hosing experiments with a strong AMOC decrease or -collapse produce the expected pattern of the bipolar seesaw, while in simulations with reduced but active AMOC no consistent warming and even cooling throughout the southern hemisphere is observed, because the active AMOC conveyed the cooling southward (Kageyama et al., 2013). FWF in the NAtl has other far-field effects and can lead to changes in polar sea ice extent, Antarctic Circumpolar Current dynamics or deep-water formation in the SOc (e.g., Rind et al., 2001b; Schmittner et al., 2003; Knutti et al., 2004) or the sub-Arctic Pacific Ocean (e.g., Saenko et al., 2004; Okazaki et al., 2010). Some of these simulated changes were related to the specific salt compensation scheme applied in the models, which refers to the addition of salt in order to compensate for hosing-driven ocean salinity changes and maintain a constant global salinity budget (Stocker et al., 2007). Below, we focus on simulated biogeochemical impacts of FW-induced AMOC perturbations on the global carbon cycle and $CO_{2,atm}$ levels.

2.1.3. Global carbon cycle response to NAtl FWF

2.1.3.1. Overview of experimental design used in the compiled studies. We synthesise 17 studies that assessed changes in simulated $CO_{2,atm}$ resulting from FW hosing in the NAtl on the basis of 147 separate simulations (Table 1; Table S2). The numerical models lack a representation of interactive ice sheets and -shelves. FW is therefore added as an imposed buoyancy forcing to the NAtl to mimic past variations in the meltwater forcing associated with changes in the cryosphere, such as for instance iceberg calving or the re-routing of major rivers (e.g., Manabe and Stouffer, 1995).

In most simulations, the ocean models were perturbed with FW fluxes imposed at the surface of the NAtl with a maximum rate ranging from 0.015 Sv to 2 Sv and a duration between 3 and 2500 yrs (Fig. 3a–c; Table S2). This FWF is often arbitrarily selected, but in some cases more specifically chosen to mimic past millennial-scale climate events. FW hosing experiments were run under interglacial or glacial climate boundary conditions, using a DVM, several EMICs with both simple and complex 2D- or 3D ocean components, as well as two ESMs (Table 1, Fig. 4a). In fact, 90% of the compiled FW hosing experiments were performed with EMICs (Table S2). FW fluxes are either prescribed in specific regions such as the Labrador Sea (Scholze et al., 2003), the St. Lawrence River Delta (Meissner, 2007), in a latitudinal band in the subtropics (e.g., 32–45°N, Marchal et al., 1998) or in the subpolar region (e.g., 50–67.5°N, Buttes et al., 2012), or in a zonally and meridionally confined area (e.g., 50–70°N and 55–10°W, Obata, 2007; 50–65°N and 55–10°W, Menviel et al., 2014). The FW fluxes prescribed in the models are often selected to remain constant (on-off hosing function), but in some cases are prescribed to gradually increase to a maximum value (linear function) or gradually increase and subsequently gradually decrease back to zero (centered triangular-shaped function, crosses in Fig. 3a–c; Table S2). The simulations of Scholze et al. (2003) and Köhler et al. (2005b) focus on terrestrial impacts, and their DVMs were forced offline with surface temperature- and precipitation anomaly fields derived from FW hosing experiments with AOGCMs. These DVMs specifically assess the response of the land biosphere to FWF, while the ocean is allowed to buffer $CO_{2,atm}$ changes only. In contrast, OGCM assess the ocean response to FWF, while neglecting any contribution from the land biosphere. EMICs and ESMs assess changes in both carbon reservoirs unless the interaction with the land biosphere is disabled (e.g., Menviel et al., 2015a). Some FW hosing experiments apply salt compensating either globally (Marchal et al., 1998; Bouttes et al., 2012; Matsumoto and Yokoyama, 2013; Menviel et al., 2014) or regionally (Menviel et al., 2014) (symbols with dots in Fig. 3a–c).

FW hosing in the NAtl consistently leads to a weakening of the AMOC (and sometimes even a collapse) in all simulations. In those model simulations, in which the AMOC remains subdued or in an off-state despite cessation of FWF, primarily in the UVic-ESCM, the AMOC is forced to resume through negative FW fluxes in the NAtl (arrows in Fig. 3a–c; Schmittner et al., 2007a; Schmittner and Galbraith, 2008; Huiskamp and Meissner, 2012; Menviel et al., 2014). In some instances the hosing experiments are combined with prescribed changes in the latitudinal position of the SHW (Huiskamp and Meissner, 2012; Menviel et al., 2014) or a parameterisation of sinking brines beneath sea ice (Bouttes et al., 2012). Below, we review simulated $CO_{2,atm}$ changes resulting from NAtl FWF as function of the magnitude, duration and total (time-integrated) amount of FW added (Fig. 5) as well as associated changes of the AMOC (Fig. 6).

2.1.3.2. Simulated $CO_{2,atm}$ changes. Because transient changes in simulated $CO_{2,atm}$ levels are very different during the hosing experiments (Fig. 7), we first focus on discussing simulated $CO_{2,atm}$ change at AMOC minima (immediately prior to the AMOC recovery, when present; Figs. 5, 6a,b), and subsequently assess the $CO_{2,atm}$ change during the subsequent AMOC recovery or -overshoot (Fig. 6c, d; Table S2).

Our compilation shows a wide positive and negative range of simulated $CO_{2,atm}$ change during FW-induced AMOC minima (Fig. 5). For the total set of simulations, no clear relationship

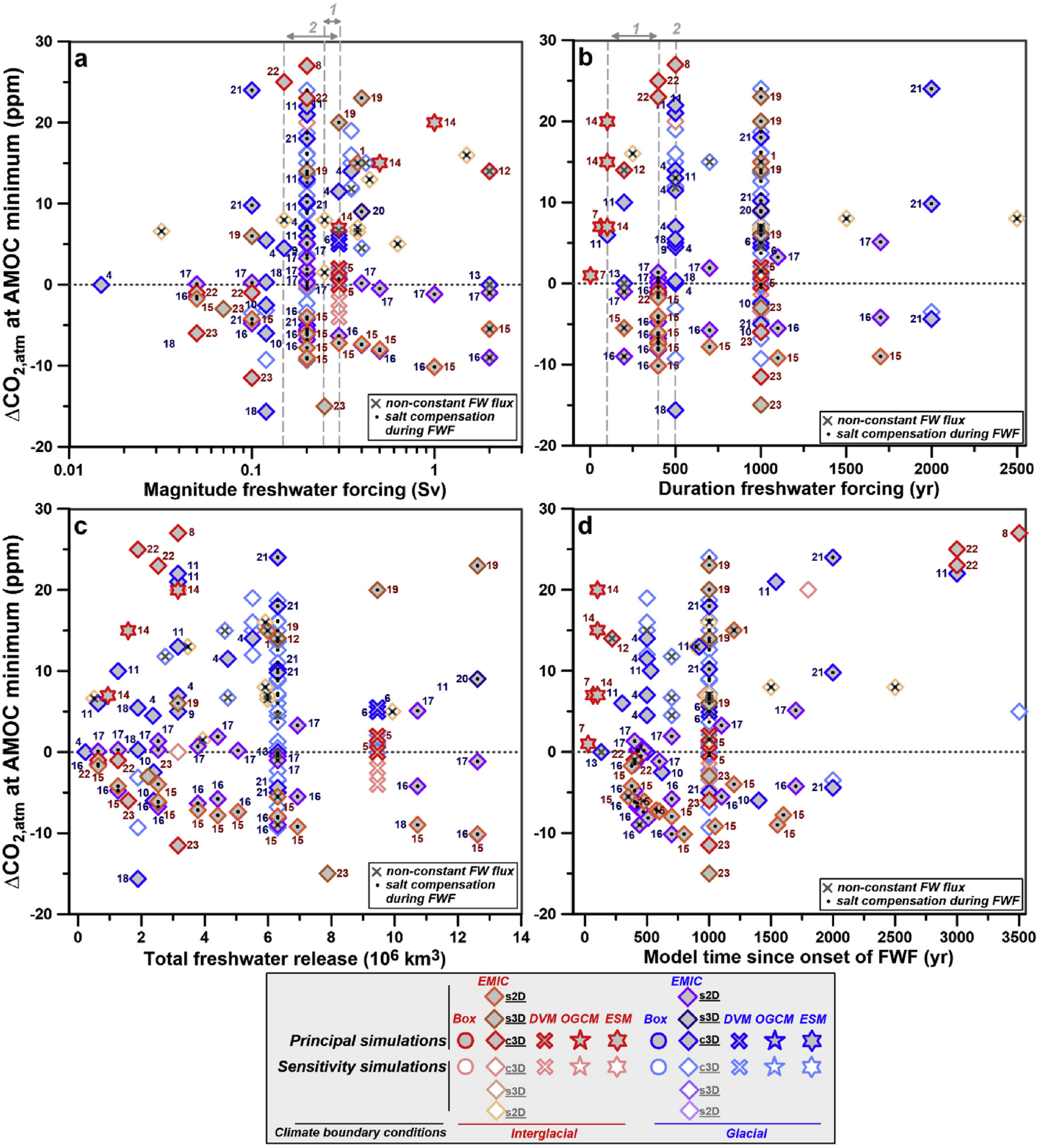

Fig. 5. Simulated changes in $CO_{2,atm}$ in coupled carbon cycle-climate models forced by FW hosing in the NAtl. Simulated $CO_{2,atm}$ changes at AMOC minima versus the (a) maximum magnitude, (b) the duration and (c) total (time-integrated) amount of FW added in the NAtl. Symbols are shown as in Fig. 3. The reported $CO_{2,atm}$ change is based on simulated $CO_{2,atm}$ changes at AMOC minima (cf. Fig. 9). Vertical dashed lines in (a) and (b) indicate estimates of the duration (D) and magnitude (M) of FW hosing into the NAtl during past millennial climate events: 1) D = 100–400 years, M = 0.25–0.3 Sv (e.g., Heinrich event 4; Roche et al., 2004), and 2) D = 500 years, M = 0.15–0.3 Sv (e.g., Heinrich event 1; Hemming, 2004). Numbers refer to Table 1, Tables S1 and S2, which list more information on the simulations and associated references. Note that in (a) the x-axis is shown on a logarithmic scale.

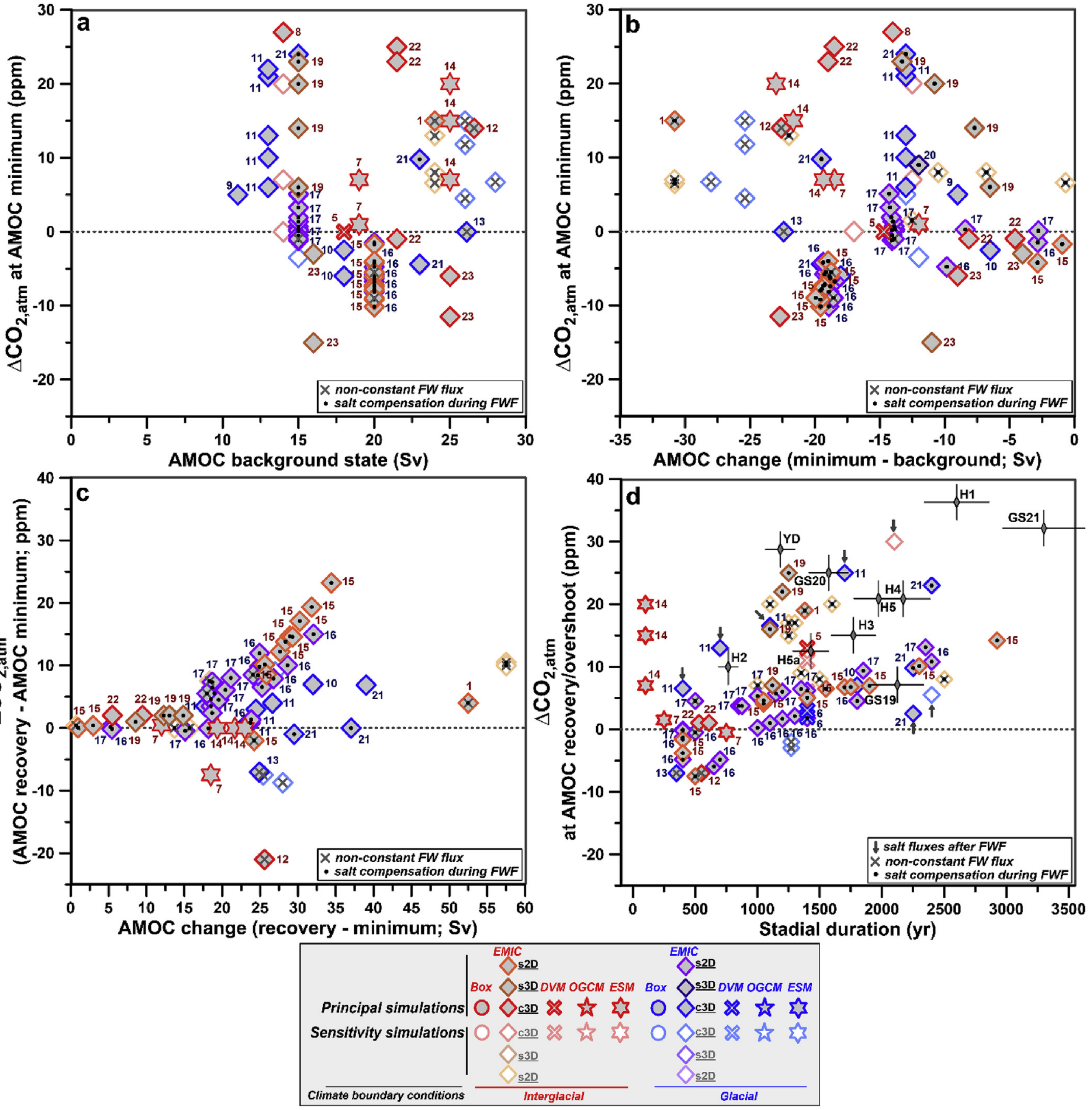

Fig. 6. Simulated changes in $CO_{2,atm}$ and AMOC in numerical models forced by FW hosing in the NAtl. Changes in simulated $CO_{2,atm}$ levels at AMOC minima versus (a) the AMOC strength prior to the FWF and (b) the maximum AMOC decrease during FWF (cf. yellow dots in Fig. 9). (c) Simulated $CO_{2,atm}$ change from AMOC minima to AMOC recovery/overshoots versus the magnitude of AMOC change at the recovery (cf. difference between yellow and red dots in Fig. 9). (d) Link between simulated $CO_{2,atm}$ change at the AMOC recovery/overshoots (referenced to background levels) versus the simulated stadial duration (cf. red dots in Fig. 9). Grey symbols in (d) highlight the observed duration of Greenland stadials (GS) and Heinrich (H) events (NGRIP members, 2004) and parallel $CO_{2,atm}$ rise as recorded in Antarctic ice cores (e.g., Ahn and Brook, 2008; Bereiter et al., 2015). Symbols are identical to Fig. 3. Black dots highlight FW hosing experiments that apply global or regional salt compensation during the prescribed FW fluxes. Crosses show simulations that use gradually increasing or centered-triangle shaped FW fluxes, rather than constant FW fluxes. Arrows point at simulations that apply salt fluxes after FW hosing (to stimulate an AMOC recovery). All information and references associated with the compiled model simulations are listed in Table 1, Tables S1 and S2.

between simulated $CO_{2,atm}$ change and the magnitude, duration or total time-integrated amount of FW added to the NAtl emerges (Fig. 5). The interval of suppressed or collapsed AMOC exceeds in most cases the interval of FWF, but no correspondence between simulated $CO_{2,atm}$ change and the time span between the onset of FWF and AMOC minima can be observed (Fig. 5d). However, individual studies show that increases in the duration or magnitude of the FW hosing, all else held constant, lead to a stronger $CO_{2,atm}$ change (e.g., Schmittner and Galbraith, 2008; Bouttes et al., 2012; Matsumoto and Yokoyama, 2013). In our compilation, these trends are likely masked by large inter-model differences in the climate boundary conditions and the forcing parameters (Fig. 5; Table S2).

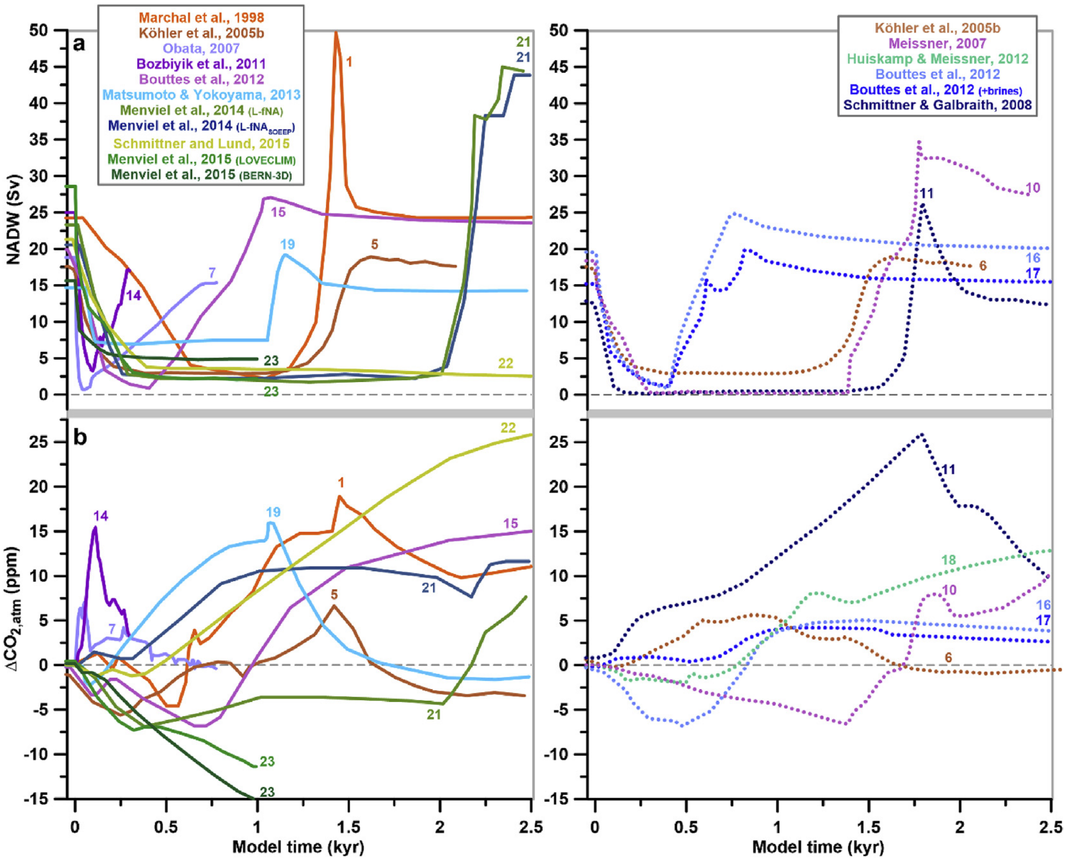

Fig. 7. Timeseries of simulated $CO_{2,atm}$ and AMOC change in selected NAtl FW hosing experiments. (a) AMOC changes, and (b) variations in simulated $CO_{2,atm}$ levels. Solid and dotted lines indicate simulations performed under interglacial and glacial climate boundary conditions, respectively. Numbers refer to Table 1, Tables S1 and S2, which list all details and references of the hosing experiments.

Both positive and negative $CO_{2,atm}$ change during AMOC minima is simulated in models with different complexities, and in simulations performed both under interglacial and glacial boundary conditions, except in principal simulations with a DVM that consistently model a small but marked $CO_{2,atm}$ rise at AMOC minima (Figs. 4a, 5a-c; Köhler et al., 2005b). Both trends can also be observed in simulations performed with different EMICs and in simulations, which apply global salt compensation during FWF and non-constant FW fluxes (Fig. 5a–c). This suggests that the observed differences in simulated $CO_{2,atm}$ change result primarily from structural differences between the models rather than experimental setups. Irrespective of the exact forcing parameters and experimental design, the 25%- to 75%-percentile range of simulated $CO_{2,atm}$ change across all model simulations under interglacial boundary conditions is −7 and +14 ppm ($n = 34$), which is larger than in simulations under glacial boundary conditions (−5 to +6 ppm; $n = 50$) (Table 2).

The mean AMOC background state is similar between the compiled interglacial (19.9 ± 3.8 Sv) and glacial simulations (18.2 ± 4.5 Sv) (Fig. 6a, Table S2). Also, simulated $CO_{2,atm}$ changes show no correlation with the magnitude of AMOC decrease during the FW hosing (Fig. 6b, Table S2). On the other hand, simulated $CO_{2,atm}$ levels in FW hosing experiments in most cases increase at the AMOC recovery (Fig. 6c). The magnitude of $CO_{2,atm}$ increase scales with the total AMOC change at that time, especially for AMOC changes larger than ~18 Sv (Fig. 6c). Accordingly, when considering the stadial length as the time encompassed by the onset of FWF and the AMOC recovery, i.e., the AMOC overshoot, when present, simulated $CO_{2,atm}$ change tends to be positive at the end of the stadial. In all cases, the stadial duration exceeds the duration of associated FWF (Fig. 8). Furthermore, the simulated increase in $CO_{2,atm}$ at the end of stadials broadly scales with the stadial duration (Fig. 6d, Table S2), in particular for stadials longer than 700 years, confirming that the findings of Schmittner and Galbraith (2008) and Bouttes et al. (2012) are found across a wider range of models. The 25%- to 75%-percentile range of simulated $CO_{2,atm}$ change at AMOC recoveries/-overshoots in interglacial simulations is +1 and + 14 ppm ($n = 26$), which again is larger than in glacial simulations (0 and + 7 ppm, $n = 36$; Fig. 6d, Table 2). Some simulations suggest a negative $CO_{2,atm}$ change for short stadials (<700 years, Fig. 6d; Menviel et al., 2008a; Bouttes et al., 2012).

Linear regression of all simulations suggests a $CO_{2,atm}$ increase of 0.4 ± 0.3 ppm ($p = 0.2$) and 0.4 ± 0.2 ppm per 100 yr stadial length ($p = 0.07$) under interglacial and glacial boundary conditions, respectively (please note that the statistical significance of the regression slope of interglacial simulations is low; Table 2). Schmittner et al. (2007a) and Schmittner and Galbraith (2008) pointed out that for sufficiently long stadial durations (e.g., >3000 years), simulated $CO_{2,atm}$ changes asymptote (Fig. 6d, Table S2), which may suggest an upper limit of carbon release from the ocean and/or the terrestrial biosphere during FW hosing. The simulated stadial length and associated $CO_{2,atm}$ rise in the compiled model studies resembles the observed duration of Greenland stadials as seen in the NGRIP ice core (NGRIP members, 2004) and parallel variations in $CO_{2,atm}$ levels observed in Antarctic ice cores (Fig. 6d; Ahn and Brook, 2008; Bereiter et al., 2012).

2.1.3.3. Driving mechanisms. Model outputs are to some extent

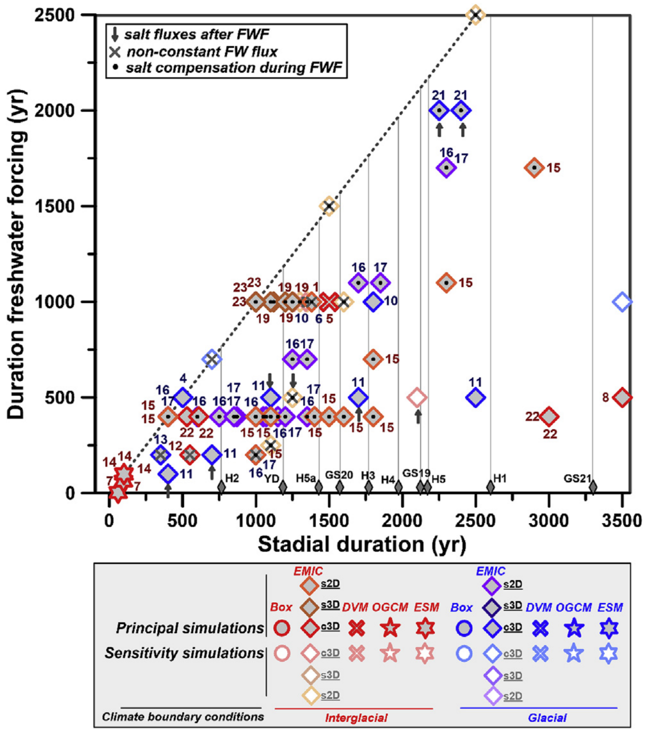

Fig. 8. Duration of freshwater fluxes in the NAtl versus the duration of the associated AMOC suppression/shutdown. The duration of reduced AMOC (i.e., stadials) is similar or longer than the interval of prescribed FW fluxes in all simulations. Stadial length is here defined as the time encompassed by the onset of FWF and the simulated AMOC recovery, i.e., the AMOC overshoot, when present. Grey symbols on the x-axis highlight the duration of Greenland stadials (GS) and H events observed in Greenland ice-core water isotope records (NGRIP members, 2004). The dotted grey line indicates a 1:1 relationship between duration of FWF and the simulated stadial length. Symbols are shown as in Fig. 3. Black dots highlight FW hosing experiments that apply global or regional salt compensation during prescribed FW fluxes. Crosses show simulations that use gradually increasing or centered-triangle shaped FW fluxes, rather than constant FW fluxes. Arrows point at simulations that apply salt fluxes after the FW hosing (to stimulate an AMOC recovery).

model-dependent: models that explicitly simulate changes in the terrestrial biosphere (different land plants, soil dynamics etc.) but have a rather simple ocean component provide insights into the impact of the land biosphere on simulated $CO_{2,atm}$ levels during FW hosing (Scholze et al., 2003; Köhler et al., 2005b). In models with a crude representation of the land biosphere, or in which fluxes from the terrestrial biosphere are held constant, FW hosing experiments highlight the role of ocean processes in simulated $CO_{2,atm}$ changes (Marchal et al., 1998, 1999; Chikamoto et al., 2012a). In simulations that resolve both changes in the land and in the ocean, simulated changes in $CO_{2,atm}$ are the integral of carbon fluxes from the ocean and the land biosphere (Meissner, 2007; Obata, 2007; Schmittner et al., 2007a; Menviel et al., 2008a; Schmittner and Galbraith, 2008; Bozbiyik et al., 2011; Bouttes et al., 2012; Huiskamp and Meissner, 2012; Matsumoto and Yokoyama, 2013). However, both the ocean- and land carbon reservoirs can show complex spatial and temporal changes of different sub-components throughout the simulations, because these have different response time scales to forcing. While some coupled models suggest that simulated $CO_{2,atm}$ changes (at the end of stadial periods) are mainly driven by carbon release from the land biosphere (Obata, 2007; Menviel et al., 2008a; Bozbiyik et al., 2011), others indicate that they are dominated by oceanic processes (Ewen et al., 2004; Meissner, 2007; Schmittner et al., 2007a; Schmittner and Galbraith, 2008; Bouttes et al., 2012; Huiskamp and Meissner, 2012; Matsumoto and Yokoyama, 2013; Menviel et al., 2014; Schmittner and Lund, 2015).

2.1.3.4. *Simulated changes of the ocean carbon inventory.*

FW hosing in the NAtl affects the ocean carbon inventory, and hence $CO_{2,atm}$ levels, in different ways, as determined by initial boundary conditions, the complexity of the ocean model and forcing parameters. A FW-driven reduction or collapse of the AMOC leads to a substantial increase in carbon storage in the Atlantic Ocean due to weaker Atlantic overturning and larger deep-water residence times (Menviel et al., 2014), reduced equilibration with the atmosphere (Bouttes et al., 2012) and increases in the CO_2 solubility in the Atlantic due to surface ocean freshening and cooling (e.g., Marchal et al., 1999; Ewen et al., 2004; Menviel et al., 2014), despite diminished marine export production in the Atlantic Ocean owing to a reduced sub-surface supply of nutrients (Marchal et al., 1998; Köhler et al., 2006; Menviel et al., 2008a; Mariotti et al., 2012). Although the Atlantic Ocean carbon sequestration can increase substantially (often by > 100 GtC), this is in most instances compensated by far-field ocean adjustments and/or terrestrial biosphere changes that accompany AMOC perturbations in the models. The ocean impact on simulated $CO_{2,atm}$ change in the compiled simulations is therefore often determined by parallel adjustments in other ocean regions, in particular due to changes in North Pacific Intermediate/Deep Water- (NPIW, NPDW), Antarctic Bottom Water- (AABW) and Antarctic Intermediate Water (AAIW) formation (e.g., Huiskamp and Meissner, 2012; Menviel et al., 2014).

Intervals of AMOC weakening were shown to cause changes in the SOc, for instance in vertical mixing (e.g., Schmittner and Galbraith, 2008), in surface ocean temperatures and CO_2 solubility (e.g., Marchal et al., 1998), as well as in sea ice extent (Ewen et al., 2004). During these intervals, increased SOc vertical mixing was found to promote the release of carbon from the deep ocean, which may be driven by different mechanisms (Schmittner et al., 2007a; Schmittner and Galbraith, 2008; Huiskamp and Meissner, 2012; Menviel et al., 2014; Schmittner and Lund, 2015): firstly, the export of salt into the southern high latitudes via NADW is reduced during an AMOC weakening, which results in a decreased density stratification of the water column in the SOc, promoting the release of carbon from the ocean (Schmittner et al., 2007a; Schmittner and Galbraith, 2008; Schmittner and Lund, 2015); secondly, AMOC perturbations enhance the formation and ventilation rate of NPIW and possibly NPDW through atmospheric and oceanic teleconnections (Saenko et al., 2004; Okazaki et al., 2010; Chikamoto et al., 2012b; Menviel et al., 2014), which causes a release of carbon from the Pacific (Menviel et al., 2014), thus leading to a rise in simulated $CO_{2,atm}$ levels (Schmittner et al., 2007a; Huiskamp and Meissner, 2012; Menviel et al., 2014). Even though ventilation changes in the Pacific Ocean remain small, they may have a large impact on $CO_{2,atm}$ levels, because the Pacific Ocean holds most of the ocean's respired carbon (Huiskamp and Meissner, 2012; Menviel et al., 2014). In some simulations, changes in Pacific overturning during AMOC perturbations also lead to considerable exchange of carbon between ocean basins, whereby a small and variable fraction may vent into the atmosphere and contribute to changes in $CO_{2,atm}$ levels (Huiskamp and Meissner, 2012).

Menviel et al. (2014) emphasise a significant $CO_{2,atm}$ increase due to an increase in deep SOc convection in their simulations (primarily in the Pacific sector), which are forced through global or regional compensating *negative* FW fluxes in the SOc (‘salt compensation’) in parallel to *positive* NAtl FW fluxes. However, the effects of ocean mixing on $CO_{2,atm}$, in particular in the SOc, are buffered to some (unspecified) extent by increased export production owing to nutrient supply from below, as shown in other simulations (Schmittner et al., 2007a; Schmittner and Galbraith, 2008; Matsumoto and Yokoyama, 2013; Schmittner and Lund, 2015). In contrast, in simulations of Menviel et al. (2014) without salt compensation, simulated $CO_{2,atm}$ change at the time of reduced AMOC is negative due to lower Atlantic overturning rates and increased carbon storage in the Atlantic.

Stocker et al. (2007) show that in hosing experiments with parameterised eddy mixing global salt compensation leads to an equatorward shift and tilting of outcropping isopycnals in the SOc, as well as changes in surface ocean buoyancy fluxes that cause an anomalous meridional heat transport to the SOc. This was shown to affect millennial-scale inter-hemispheric climate patterns in FW hosing experiments by amplifying surface warming in the SOc (Stocker et al., 2007). Salt compensation in some FW hosing experiments compiled here (e.g., Marchal et al., 1999; Bouttes et al., 2012; Matsumoto and Yokoyama, 2013) lowers the density stratification of the SOc water column and/or increases the formation of deep- and intermediate-water masses (e.g., NPIW, AABW or AAIW), which may have an additional impact on $CO_{2,atm}$ levels compared to FW hosing experiments without salt compensation. By applying global and regional salt compensation, Menviel et al. (2014) have shown that the effect of this additional "forcing" can be large, as both the sign of simulated $CO_{2,atm}$ change as well as its amplitude significantly vary. However, a comprehensive comparison of FW hosing experiments with and without global salt compensation is often not available (Marchal et al., 1999; Bouttes et al., 2012; Matsumoto and Yokoyama, 2013). The associated change in simulated $CO_{2,atm}$ due to this adjustment remains unclear, and therefore contributes to inter-model differences in simulated $CO_{2,atm}$ changes in NAtl FW hosing experiments.

2.1.3.5. Simulated changes in terrestrial carbon inventory. FW supply to the NAtl leads in some simulations to a carbon loss from the terrestrial biosphere during AMOC minima primarily as a result of surface air cooling and drying in the northern hemisphere, and changes in precipitation associated with southward shifts of the ITCZ (Köhler et al., 2005b; Obata, 2007; Menviel et al., 2008a; Bozbiyik et al., 2011). In the northern high-latitudes, the treeline shifts equatorward and the areal extent of boreal forests contracts during AMOC minima, while improved growing conditions and slower soil decomposition increase carbon stocks in the northern mid-latitudes (Köhler et al., 2005b). This leads to an initial decrease and subsequent rise of $CO_{2,atm}$ during AMOC minima under interglacial climate boundary conditions (Fig. 9a; Köhler et al., 2005b). When the AMOC recovers, carbon is released from mid-latitude soils due to increased temperatures and higher rates of soil degradation outcompeting the effects of a regrowth of boreal forests, increasing $CO_{2,atm}$ above background levels (Fig. 9a; Köhler et al., 2005b). In the interglacial simulation of Menviel et al. (2008a), northern high-latitude and tropical carbon stocks also decline during FWF, which outweighs an increase in southern-hemisphere vegetation carbon stocks due to enhanced precipitation associated with a southward shift of the ITCZ, and therefore acts to increase $CO_{2,atm}$ (Fig. 9c). In contrast to Menviel et al. (2008a), Bouttes et al. (2012) and Schmittner and Galbraith (2008) simulate carbon uptake by the terrestrial biosphere during AMOC minima, which is primarily driven by enhanced land vegetation in a warmer and wetter southern hemisphere, and/or increased global carbon storage in soils (Fig. 9b,d).

The response of the terrestrial biosphere to AMOC perturbations is generally faster than that of the ocean (Fig. 9; e.g., Schmittner and Galbraith, 2008; Bouttes et al., 2012; Matsumoto and Yokoyama, 2013), although it may take a few centuries to re-establish a new equilibrium in the land biosphere carbon inventory due to different adjustment timescales of land vegetation and soil carbon processes (Köhler et al., 2005b). Soil overturning rates were found to be spatially heterogeneous and faster in the temperate mid-latitudes than in colder high latitudes (e.g., Köhler et al., 2005b). Even when globally integrated carbon changes in the terrestrial biosphere are small, large (compensating) regional changes in vegetation cover may occur in DVMs.

2.1.3.6. Transient evolution of the ocean- and land carbon inventories. Comparing transient $CO_{2,atm}$ changes in NAtl FW hosing experiments along with associated shifts in ocean- and land carbon inventories highlights that they can evolve differently throughout the simulations and can be determined by different internal processes (Fig. 9). Adjustments in the non-dominant reservoir typically buffer the impact of changes in the dominant reservoir by 50–80% (e.g., Köhler et al., 2005b; Schmittner et al., 2007a; Schmittner and Galbraith, 2008).

In the DVM simulations of Köhler et al. (2005b), the oceanic carbon pool is responsive to land carbon changes only through buffering the surplus or deficit of carbon in the atmosphere (by ~80%). Simulated $CO_{2,atm}$ changes are, by model construction, primarily controlled by terrestrial carbon changes (Fig. 9a). Other simulations portrayed in Fig. 9b–d are based on coupled carbon cycle-climate models, which differ, however, in the structural and spatial complexity of the individual ocean and atmosphere components. Simulated $CO_{2,atm}$ increase in Schmittner et al. (2007a) and Schmittner and Galbraith (2008) during AMOC minima are primarily driven by ocean carbon release (through SOc vertical mixing and a reduced efficiency of the ocean carbon pumps; Fig. 9b). Most of the land carbon changes in these FW hosing experiments are driven by increased carbon storage in soils, but these are much smaller than parallel changes in the ocean carbon inventory, and therefore only buffer ocean-driven $CO_{2,atm}$ variations (Fig. 9b). A limitation of the UVic-ESCM used by Schmittner et al. (2007a) and Schmittner and Galbraith (2008) is the atmospheric component, which is a simple 2D energy-moisture-balance model (Table S9). Therefore, the response of the vegetation and ocean-to-atmosphere CO_2 fluxes to changes in precipitation may not be as sensitive as in a coupled carbon cycle-climate model with a better-resolved atmosphere such as the dynamic albeit simplified atmosphere in LOVECLIM (Menviel et al., 2008a, Fig. 9c). In contrast to Schmittner et al. (2007a) and Schmittner and Galbraith (2008), the $CO_{2,atm}$ response under pre-industrial boundary conditions in Menviel et al. (2008a) is primarily driven by carbon loss from the terrestrial biosphere (decline of northern-hemisphere land carbon stocks) but is compensated by 70% through ocean carbon uptake (via weaker upwelling in the tropics and an enhanced water column density stratification; Fig. 9c). In their glacial simulations, however, ocean carbon uptake overcompensates parallel carbon loss from the terrestrial biosphere, and therefore causes a drop in simulated $CO_{2,atm}$ (Fig. 9c). Disparities in the UVic-ESCM- and LOVECLIM outputs may therefore to some extent be related to the ability of the atmospheric models to simulate changes of the hydrological cycle, and its interaction with the land biosphere and ocean. During the interval of FW hosing, Bouttes et al. (2012) simulate an increase in soil and vegetation carbon stocks in the tropics (as simulated in Bozbiyik et al., 2011) and the southern hemisphere, which causes a drop in $CO_{2,atm}$ levels during AMOC minima, despite substantial ocean carbon loss primarily due to a decreased ocean CO_2 solubility (i.e., upper-ocean warming) in the SOc (Fig. 9c). The simple 2D nature of the ocean model used by Bouttes et al. (2012) with CLIMBER-2 might explain differences in the response timescale and magnitude of parallel ocean carbon release during FW hosing compared to more complex ocean models as in the UVic-ESCM (Fig. 9b,d). The same might apply to

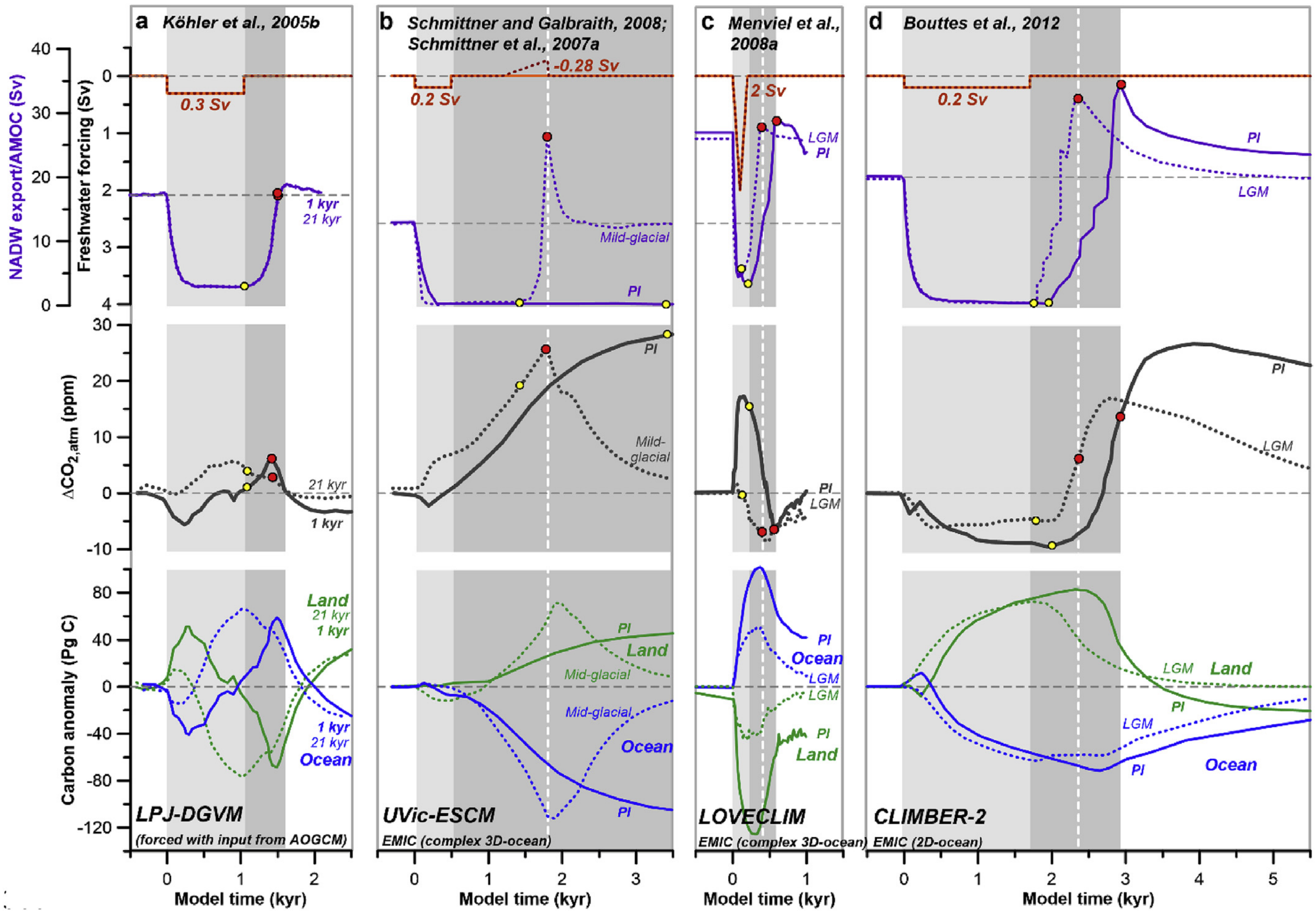

Fig. 9. Temporal evolution of simulated $CO_{2,atm}$ changes in NAtl FW hosing experiments and associated variations in the ocean and land carbon inventories. Re-drawn after (a) Köhler et al. (2005b) showing simulations without CO_2 fertilisation feedback, (b) Menviel et al. (2008a), (c) Schmittner et al. (2007a) and Schmittner and Galbraith (2008), and (d) Bouttes et al. (2012). From top to bottom: FW hosing function applied to the NAtl (orange, reversed axis), strength of Atlantic overturning (purple), changes in simulated $CO_{2,atm}$ levels (dark grey), and variations in the total oceanic (blue) and terrestrial (green) carbon inventories. Solid and stippled lines show results from model simulations run under interglacial (pre-industrial (PI)/modern) or glacial (last glacial maximum, LGM) boundary conditions, respectively. Light grey bars highlight the duration of FW hosing in the NAtl, while dark grey bars indicate the duration of the associated slowdown or collapse of the AMOC observed in interglacial simulations. The vertical white dashed line highlights the AMOC overshoot present in glacial simulations. In all cases, the AMOC recovery significantly lags the end of FWF (cf. Fig. 8). Yellow dots highlight FW-driven AMOC minima and simulated $CO_{2,atm}$ changes at that time (as illustrated in Figs. 5 and 6a,b). Red dots mark the stadial duration and the modelled $CO_{2,atm}$ change at the AMOC recovery/overshoot (as illustrated in Fig. 6c,d). Further details on the simulations can be found in Table 1, Tables S1 and S2. Note that all x-axes have the same scaling.

the atmospheric model of CLIMBER-2, which is a coarse-resolution 2.5D statistical-dynamical model. Although better than a simple energy-moisture balance model of the atmosphere (UVic-ESCM), its simple nature may also lead to biases in simulated precipitation fields, and hence land-atmosphere CO_2 fluxes, that are not simulated with more sophisticated atmospheric models such as with LOVECLIM or others (Table S9).

In summary, simulated $CO_{2,atm}$ change in coupled carbon cycle-climate models are driven by different processes, even when a similar direction of change is observed. In case models agree on the major driver of simulated $CO_{2,atm}$ change (ocean or land), the internal processes in that reservoir can be very different.

2.1.3.7. Link to stadial durations. The observed link between simulated $CO_{2,atm}$ change and the stadial length (>700 years) suggests that cumulative carbon release from the ocean and/or the terrestrial biosphere is determined by the combined duration of AMOC suppression and -recovery. The characteristic millennial timescale of the increase in simulated $CO_{2,atm}$ at the end of stadial conditions is consistent with a slow (deep-) ocean response (e.g., Schmittner and Galbraith, 2008; Bouttes et al., 2012) that is modulated by changes in the terrestrial biosphere. Simulated $CO_{2,atm}$ change due to fast terrestrial biosphere adjustment is anticipated to be less dependent on the stadial duration. However, this notion remains currently untested, and is likely complicated by possible fast (centennial-scale) SOc CO_2 outgassing due to SHW wind intensity changes (Menviel et al., 2018) or rapid variations in Antarctic sea ice extent (as hypothesised by Rae et al., 2018, but not tested with numerical models). The close link between simulated $CO_{2,atm}$ change and stadial lengths ~>700 years may also imply that the magnitude of oceanic (e.g., CO_2 solubility, ventilation, sea ice, carbon redistribution) and/or terrestrial carbon changes (e.g., carbon respiration in soils, forest extent) respond linearly to the severity of the AMOC perturbation, and possibly the magnitude of AMOC change at the recovery. However, different ocean circulation patterns (e.g., differences in deep- and intermediate water formation) may evolve despite similar FW hosing in the NAtl, which may account for a decoupling of simulated $CO_{2,atm}$ and stadial durations in FW hosing experiments (e.g., Huiskamp and Meissner, 2012; Menviel et al., 2014).

2.1.3.8. Role of climate boundary conditions. In FW hosing experiments, simulated $CO_{2,atm}$ changes were shown to depend on climate boundary conditions (Köhler et al., 2005b, 2006; Schmittner et al., 2007a; Menviel et al., 2008a; Bouttes et al., 2012). One reason why simulated $CO_{2,atm}$ changes are slightly lower under glacial background climate conditions may be due to the fact that glacial simulations are often equilibrated (i.e., spun up) under low $CO_{2,atm}$ condition, and therefore have reduced amounts of carbon in the ocean. As any changes in ocean-atmosphere or land-atmosphere CO_2 fluxes broadly scale with the amount of carbon available, they are inherently smaller under glacial boundary conditions. One can also surmise that when FWF is applied to the Atlantic Ocean characterised by weaker overturning, the resulting AMOC suppression may be reduced, and hence associated ocean processes such as the ventilation of the deep Pacific, SOc vertical mixing and CO_2 solubility changes may have a relatively smaller impact on $CO_{2,atm}$. However, the link between FW-driven AMOC changes and parallel $CO_{2,atm}$ variations is likely model-specific owing to the influence of parameters such as the initial state of the North Pacific halocline, the degree of density stratification of the SOc, global sea ice extent, or the stability characteristics of overturning cells, which may vary from model to model.

Climate background conditions may also affect the timescale of the AMOC recovery (Fig. 9c,d; Menviel et al., 2008a; Bouttes et al., 2012). We have argued that a longer duration of the AMOC suppression may leave more time for processes to fully affect $CO_{2,atm}$ levels. The model's climate background conditions may therefore impact on the magnitude of simulated $CO_{2,atm}$ changes through an influence on the length of stadial conditions.

The contribution of variations in the terrestrial biosphere to simulated $CO_{2,atm}$ change is also a function of the applied climate boundary conditions, because the initial distribution of vegetation and soils, the temperature-dependent degradation of organic matter and/or CO_2 fertilisation on photosynthesis matter for the simulated $CO_{2,atm}$ response (Köhler et al., 2005b; Menviel et al., 2008a). In the experiments of Köhler et al. (2005b), the area of increased soil storage at mid-latitudes is compressed under glacial conditions due to the existence of land ice, which makes simulated $CO_{2,atm}$ levels more sensitive to changes in the extent of boreal and temperate forests (Fig. 9a). In most simulations, however, the overall character and the processes driving changes in the oceanic and terrestrial carbon inventories under glacial climate backgrounds are similar to interglacial simulations, as the physics behind the simulations does not change (Fig. 9b–d; Schmittner et al., 2007a; Menviel et al., 2008a; Schmittner and Galbraith, 2008; Bouttes et al., 2012). However, the timing and magnitude of these changes may vary in such a way that their integrated effect on $CO_{2,atm}$ may cause a sign change in simulated $CO_{2,atm}$. This is best illustrated by the simulations of Menviel et al. (2008a), which under interglacial climate conditions show a dominance of integrated carbon release from the terrestrial biosphere over ocean carbon uptake, and hence a $CO_{2,atm}$ increase (Fig. 9c). Under glacial conditions, however, the terrestrial carbon release is smaller and although ocean carbon uptake during AMOC perturbations is not as strong as in the interglacial simulation, it is stronger than terrestrial carbon loss, resulting in a net decline of $CO_{2,atm}$ levels (Fig. 9c).

Peak glacial climate boundary conditions may not be the most appropriate starting point to simulate millennial-scale $CO_{2,atm}$ variations, which primarily occur under mild-glacial climate conditions. van Meerbeeck et al. (2011) point out differences in seasonality, the formation of NADW, and global sea ice extent, while Gong et al. (2013) highlight different characteristics of the AMOC recovery between glacial and mild-glacial climate boundary conditions. As discussed above, these aspects may have a large impact on simulated $CO_{2,atm}$ levels, and more realistic climate boundary conditions therefore need to be taken into account in future transient or equilibrium climate simulations that aspire to explain past millennial-scale $CO_{2,atm}$ changes (e.g., Menviel et al., 2015b).

2.1.3.9. Model-predictions of past millennial-scale $CO_{2,atm}$ changes due to NAtl FWF. Because simulated $CO_{2,atm}$ changes are strongly dependent on initial boundary conditions, the model complexity and the characteristics of the AMOC, a model-based prediction of $CO_{2,atm}$ change due to NAtl FWF on the basis of the forcing parameters alone is likely highly uncertain. The stadial duration may serve as a better metric for a model-derived prediction of $CO_{2,atm}$ change owing to NAtl FWF, because it expresses more clearly the impact of FWF on the AMOC. Our linear regressions of modelled $CO_{2,atm}$ change in FW hosing experiments under interglacial and glacial boundary conditions (Table 2) respectively predict a $CO_{2,atm}$ increase of 0.4 ± 0.3 ppm and 0.4 ± 0.2 ppm per 100 year stadial duration. Taking stadial H5a (Greenland stadial 13) with a duration of ~1400 years as an example, in both cases the predicted $CO_{2,atm}$ during this interval of 6 ± 4 ppm and 6 ± 3 ppm is lower than observed (13 ± 2 ppm). This also applies to other stadial periods. Our compilation hence shows that NAtl FW hosing experiments alone cannot reproduce observed $CO_{2,atm}$ change over millennial timescales.

2.2. Freshwater forcing in the Southern Ocean

2.2.1. Proxy data constraints on variable FW flux into the SOc

Based on sea level records, Clark et al. (2002) suggested that an Antarctic meltwater source is required to explain the observed deglacial patterns of global sea level rise during meltwater pulse 1A (MWP-1A) at the onset of the Bølling-Allerød warm period. This is supported by foraminiferal and diatom stable oxygen isotope data from the SOc that suggest a surface freshening broadly synchronous with MWP-1A (Shemesh et al., 1995; Clark et al., 1996). Planktic foraminiferal stable oxygen isotope minima are also observed during the last glacial period, which are accompanied by increased supply of IRD at interstadial onsets in the NAtl (Kanfoush et al., 2000). These were interpreted as phases of Antarctic ice sheet instability that could have supplied large volumes of debris-laden meltwater to the SOc (Kanfoush et al., 2000). Evidence of temporal deglacial changes in IRD deposition in the iceberg alley in the Scotia Sea (Weber et al., 2014) and surface elevation changes of the West Antarctic Ice Sheet (Fogwill et al., 2017) have corroborated the contention of rapid reductions in the Antarctic ice sheet and a significant contribution to global sea level rise on millennial timescales (Clark et al., 2002; Rohling et al., 2004). FW fluxes are prescribed to the SOc surface to mimic these changes in numerical models.

2.2.2. Physical response of climate models to SOc FWF

FW hosing in the SOc leads to surface cooling, a strengthening of the SHW, and an expansion of Antarctic sea ice cover (e.g., Richardson et al., 2005; Stouffer et al., 2007; Swingedouw et al., 2008; Menviel et al., 2010; Ma and Wu, 2011), which in turn causes a northward shift of the ITCZ (Bozbiyik et al., 2011; Menviel et al., 2010), as well as enhanced upper-ocean stratification, subsurface ocean warming and reduced AABW formation in the SOc (Swingedouw et al., 2008; Menviel et al., 2010). These changes also influence the AMOC (Seidov and Maslin, 2001; Weaver et al., 2003; Trevena et al., 2008; Swingedouw et al., 2009; Ma and Wu, 2011) through changes in meridional heat transport, a propagation of the Antarctic salinity anomaly to the NAtl and adjustments of the SHW wind intensity (Swingedouw et al., 2009). Specifically, FW fluxes into the SOc were suggested to have promoted an abrupt strengthening of the AMOC during the Bølling-Allerød warm period, and hence explain warming throughout the northern hemisphere (Weaver et al., 2003). Below, we discuss the biogeochemical impacts of FWF in the SOc in numerical model simulations.

2.2.3. Global carbon cycle response to SOc FWF

2.2.3.1. Overview of experimental design used in the compiled studies. We have compiled seven studies that have assessed changes in $CO_{2,atm}$ owing to FW hosing in the SOc based on 31 model simulations (Table 1, Table S3). The experiments were run under both interglacial and glacial climate boundary conditions, using mostly EMICs, with a simple 2D- (Bern-2.5D, CLIMBER-2), simple 3D- (Bern-3D) and a complex 3D ocean component (UVic, LOVECLIM), but also the ocean biogeochemical model PISCES (with offline tracer transport from an OGCM) and one ESM (NCAR-CSM1.4-carbon; Table 1, Table S3). In these simulations, FW is added to the SOc with a magnitude ranging from 0.05 Sv to 1 Sv and with a duration ranging between 100 and 2000 yrs (Fig. 3a–c; Table S3). FW fluxes are mostly held constant (on-off hosing function), with the exception of Marchal et al. (1998) and Menviel et al. (2010), who use gradually changing fluxes (i.e., a centered-triangular function), and Ewen et al. (2004), who impose gradually increasing FW fluxes that cease abruptly (i.e., a linear function) (crosses in Fig. 3a–c). The exact region where the FW hosing is applied varies among distinct circumpolar latitudinal bands, e.g., 60°S-75°S (Marchal et al., 1998; Bouttes et al., 2012), particular sectors of the SOc, e.g., 163°E–11°E and 70°S–80°S (Menviel et al., 2010, 2015a), and intermediate- (Ewen et al., 2004) and bottom water formation sites, e.g., in the Ross or Weddell Sea (Bozbiyik et al., 2011). Some FW hosing experiments apply global salt compensation (symbols with dots in Fig. 3a–c; Bouttes et al., 2012).

2.2.3.2. Simulated $CO_{2,atm}$ changes. The sign and magnitude of simulated $CO_{2,atm}$ change in response to FWF in the SOc (at the time of cessation of FWF) is generally consistent among the coupled carbon cycle-climate models, apart from simulations of Ewen et al. (2004) (Figs. 4b, 10, Table S3). The simulated $CO_{2,atm}$ change at the time of FWF cessation is in most cases close to the maximum simulated $CO_{2,atm}$ change throughout the simulations (Fig. 11). In addition, the temporal evolution of modelled $CO_{2,atm}$ is broadly similar in these simulations (Fig. 12).

Most interglacial simulations indicate a $CO_{2,atm}$ drop of −7 to −12 ppm (Fig. 10; Marchal et al., 1998; Bozbiyik et al., 2011; Menviel et al., 2015a). This is consistent with model simulations run under glacial boundary conditions with CLIMBER-2 (Bouttes et al., 2012), which show a progressively stronger $CO_{2,atm}$ drop with increasing magnitude of SOc FW fluxes from 0.05 to 1 Sv (0 to −13 ppm; Fig. 10). Bouttes et al. (2012) and Menviel et al. (2015a) highlight that AABW overturning decreases due to SOc FWF proportional to the magnitude of the prescribed fluxes, and in parallel to a reduction of the AMOC (Fig. 13). An exception to these trends is shown by Ewen et al. (2004) and Menviel et al. (2010), who under interglacial climate boundary conditions simulate a $CO_{2,atm}$ rise of +11/ + 42 ppm, and +2.5 ppm, respectively (Fig. 10). The simulations of Ewen et al. (2004) differ from other FW hosing experiments for a number of reasons. Firstly, FW is added to the ocean in a very confined region, namely at the AAIW formation site south of South America, and secondly, the AMOC background state in these simulations is much lower (1.0–14.3 Sv), which was provoked by FWF in the NAtl (Fig. 13; Table S3). Hence, AMOC overturning intensifies in the SOc FW simulations of Ewen et al. (2004), in contrast to what is modelled in all other experiments (Fig. 13). But more importantly, Ewen et al. (2004) only consider the inorganic carbon cycle in their simulations (i.e., solubility and speciation effects), but neglect any feedbacks or processes related to the cycling of organic carbon (e.g., productivity changes, remineralisation, etc). Setting therefore the results of Ewen et al. (2004) aside, the 25%- to 75%-percentile range of simulated $CO_{2,atm}$ changes in SOc FW hosing experiments performed under interglacial and glacial boundary conditions is −7 to −9 ppm ($n = 6$) and −2 to −4 ppm ($n = 15$), respectively (Fig. 4b, Table 2 and Table S3). A linear regression of the model results show a -1.7 ± 1.2 ppm ($p = 0.2$) and -0.6 ± 0.1 ppm change in simulated $CO_{2,atm}$ for every 10^6 km^3-volume of FW added in the SOc ($p<0.05$), respectively (Table 2; please note that the statistical significance of the regression slope for interglacial simulations is low).

2.2.3.3. Driving mechanisms. The simulations of Bouttes et al. (2012) with a simple 2D-EMIC show a decrease in $CO_{2,atm}$ concentrations, because SOc cooling enhances the solubility of CO_2 in the ocean and the transport of dissolved inorganic carbon (DIC) into the ocean interior by AABW and NADW increases. Carbon is also more efficiently stored in the ocean interior due to slower deep-water overturning. The associated ocean carbon uptake is partly compensated by carbon loss from the terrestrial biosphere due to overall drier and colder conditions in both hemispheres (Bouttes et al., 2012). The oceanic response is consistent with the Bern-2.5D simulations of Marchal et al. (1998) that lack specific ocean-land vegetation feedbacks. In these simulations, ocean carbon uptake through SOc cooling and CO_2 solubility increase explains most of the −7 ppm-$CO_{2,atm}$ drop during FW hosing in the SOc. By disabling land-atmosphere CO_2 fluxes in FW hosing experiments in the SOc with 3D-EMICs, Menviel et al. (2015a) suggest that ocean carbon uptake in the SOc results from reduced AABW formation, which decreases ocean outgassing of CO_2 and increases deep-ocean carbon storage, thereby lowering $CO_{2,atm}$ levels (Fig. 13). In contrast, Menviel et al. (2010) simulate an increase in $CO_{2,atm}$ in SOc FW hosing experiments (Fig. 11; Table S3). In their simulations, carbon loss from the terrestrial biosphere owing to the decline of land vegetation in the southern hemisphere is nearly entirely compensated by enhanced export production in the equatorial ocean, increased ocean CO_2 solubility and slight carbon uptake in the tropical region, thus leading to a slight rise of $CO_{2,atm}$ levels. Menviel et al. (2010) also simulate a strengthening of NADW export during the reduction in AABW formation, in contrast to Bozbiyik et al. (2011), Marchal et al. (1998) and Bouttes et al. (2012), which may explain differences in the sign of $CO_{2,atm}$ changes simulated in this study.

2.2.3.4. Transient evolution of the ocean- and land carbon inventories. Simulated $CO_{2,atm}$ changes in SOc FWF experiments result from a delicate balance between changes in the ocean- and land carbon inventories. This is emphasised by a comparison between transient changes in $CO_{2,atm}$ levels simulated by Bouttes et al. (2012) and Bozbiyik et al. (2011) that are qualitatively similar despite different climate boundary conditions and durations of FWF (Fig. 11). In simulations with the ESM NCAR CSM1.4-carbon under interglacial boundary conditions, FWF in the SOc causes an increase in carbon storage in the tropical land biosphere, which drives a decrease in $CO_{2,atm}$ levels (Fig. 11a; Bozbiyik et al., 2011). This drop in $CO_{2,atm}$ is amplified by enhanced ocean carbon uptake due to cooling during FWF and buffered by increased ocean CO_2 solubility in the SOc after cessation of FWF (Fig. 11a; Bozbiyik et al., 2011). In contrast, in the glacial simulations of Bouttes et al. (2012) oceanic carbon uptake dominates the simulated $CO_{2,atm}$ decrease (i.e., through ocean CO_2 solubility increase and DIC transport into ocean interior), which is buffered by carbon loss from the terrestrial biosphere due to widespread drying and cooling (Fig. 11b), as described above. This comparison emphasises that a similar direction of $CO_{2,atm}$ change can be brought about by very different

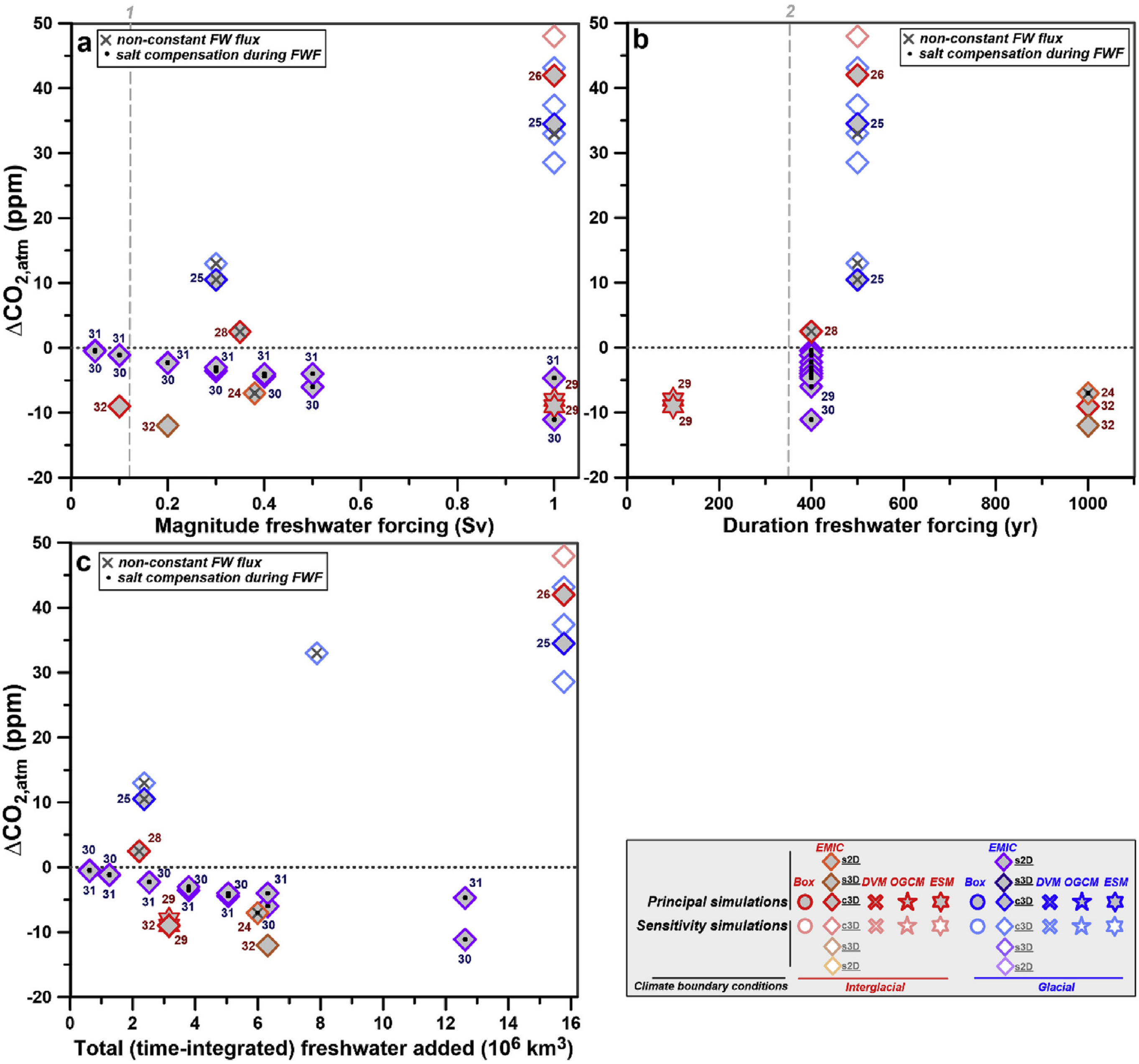

Fig. 10. Simulated $CO_{2,atm}$ changes in coupled carbon cycle-climate models forced by FW hosing in the SOc. Simulated $CO_{2,atm}$ levels at the end of FWF (which in most cases coincides with the maximum simulated $CO_{2,atm}$ change throughout the experiments; cf. pink dots in Fig. 11) as function of the (a) maximum magnitude, (b) duration and (c) total (time-integrated) amount of FW fluxes in the SOc. Symbols are identical to Fig. 3. Symbols with centered black dots highlight simulations that apply global salt compensation during FW hosing. Crosses indicates simulations, which apply non-constant FW fluxes. References and further information on all model simulations are listed in Table 1, Tables S1 and S3. Vertical dashed lines indicate recent estimates of 1) the magnitude of Antarctic FW discharge during meltwater pulse 1A (~0.11 Sv; Golledge et al., 2014) and 2) the duration of meltwater pulse 1A (~350 years; Deschamps et al., 2012).

terrestrial and ocean processes and the interaction between them, which emphasises that the mechanisms underlying the simulated $CO_{2,atm}$ decrease due to FWF in the SOc remain uncertain.

2.2.3.5. Model-predictions of past millennial-scale $CO_{2,atm}$ changes due to SOc FWF. With the exception of MWP-1A, the timing and rates of FW fluxes from the Antarctic continent during millennial-scale climate events remain poorly constrained. However, MWP-1A may provide an upper limit of the Antarctic meltwater supply during these events, as it was associated with very large fluxes. The most recent estimate of FW supply during MWP-1A suggests an Antarctic contribution of 0.11 Sv (Golledge et al., 2014) over 350 years (Deschamps et al., 2012), suggesting combined a total (time-integrated) FW release of 1.2×10^6 km^3. Both parameters are close to the forcing applied by Bouttes et al. (2012), who forced CLIMBER-2 with a FW input into the SOc with a rate of 0.1 Sv over 400 years under glacial boundary conditions. The simulated $CO_{2,atm}$ change in CLIMBER-2 is ~ −1.5 ppm only (Fig. 10). This finding is consistent with the magnitude of $CO_{2,atm}$ change obtained by the linear trend of all compiled SOc FWF experiments (Table 2), suggesting a $CO_{2,atm}$ drop of 0.7 ppm and 2 ppm under interglacial or glacial boundary conditions, respectively (for a 1.2×10^6 km^3 FW release during MWP-1A). Hence, from the current (limited) model standpoint, SOc FW supply associated with MWP-1A or in fact millennial-scale

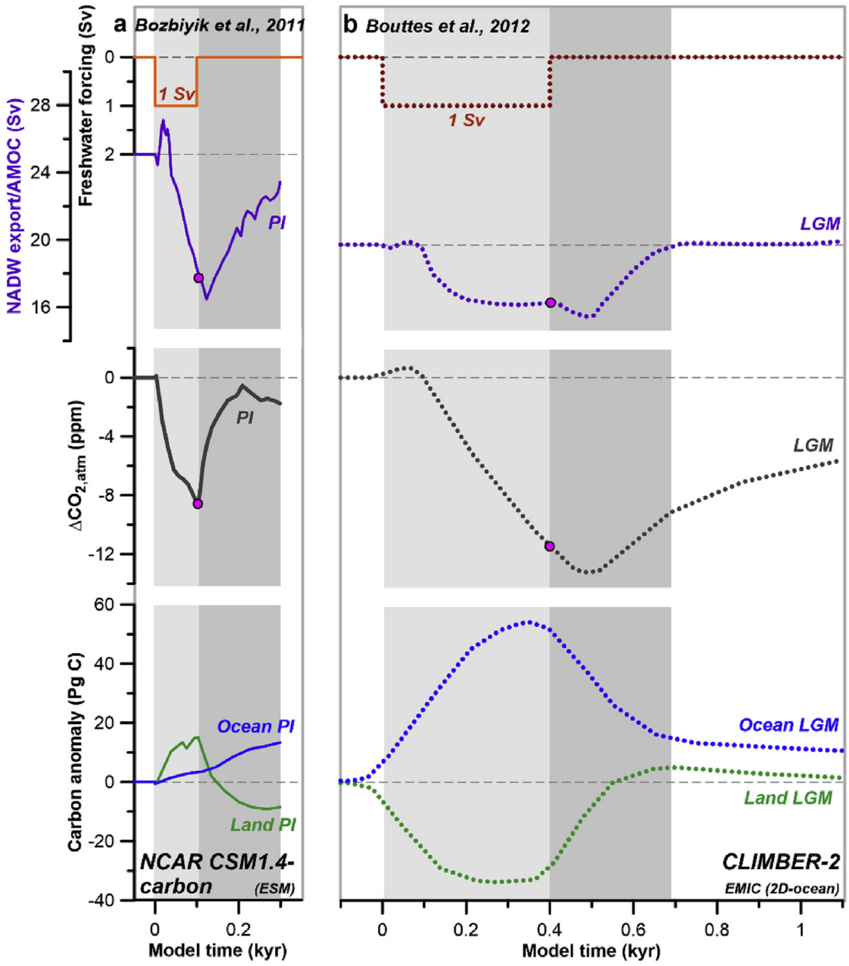

Fig. 11. Temporal evolution of simulated $CO_{2,atm}$ changes and variations in the ocean- and land carbon inventories in SOc FW hosing experiments. Re-drawn after (a) Bozbiyik et al. (2011) and (b) Bouttes et al. (2012). From top to bottom: FW hosing function applied to the SOc (orange, reversed axis), AMOC strength (purple), simulated $CO_{2,atm}$ changes (dark grey), and variations in the total oceanic (blue) and terrestrial (green) carbon inventories. Solid and stippled lines show results from model simulations run under interglacial and glacial boundary conditions, respectively. Light grey bar highlights the duration of FW hosing in the SOc, while dark grey bars indicate the duration of AMOC suppression. In both cases, FWF in the SOc has an impact on the AMOC, and its recovery significantly lags the end of FWF. Pink dots indicate the simulated $CO_{2,atm}$ change at the end of FW hosing and the associated AMOC minimum (as illustrated in Fig. 13). Further details are given in Table 1, Tables S1 and S3. Note that both x-axes have the same scaling.

climate variability likely did not cause a significant change in $CO_{2,atm}$ levels.

2.3. Southern-hemisphere westerlies

2.3.1. Proxy data constraints on past changes of the SHW 'geometry'

Reconstructing the strength and intensity of the SHW in the past is challenging, and is based on indirect indicators of changes in the position of ocean fronts, ocean temperature, dust fluxes, ocean productivity and precipitation (see reviews of Shulmeister et al., 2004; Hodgson and Sime, 2010; Kohfeld et al., 2013). However, these changes are not exclusively related to SHW wind changes, and complex regional and inter-annual dynamics may characterise the SHW wind system in the past (similarly to today), which makes inferences based on proxy data difficult and highly uncertain (Kohfeld et al., 2013). Although there is a large discrepancy regarding the strength and latitudinal position of the SHW during the last glacial maximum (LGM) ranging from northward shifted (by up to +9°) and poleward shifted westerlies (by up to −8°), the SHW were most likely either displaced northward (by 3–5°) or were slightly stronger (with unconstrained magnitude), but a southward shift or a weakening cannot robustly be ruled out either (Kohfeld et al., 2013). These estimates may serve as an upper limit for SHW changes during millennial-scale climate events, which were recently identified in Antarctic ice records (Landais et al., 2015; Markle et al., 2017; Buizert et al., 2018). Large shifts in the position of the westerlies of 7–10° as hypothesised by Toggweiler et al. (2006) are not supported by the compilation of Kohfeld et al. (2013).

Changes in the position or intensity of the SHW during Antarctic warming events and Greenland stadials are poorly constrained. Anderson et al. (2009) and Denton et al. (2010) conjectured a poleward shift and/or strengthening of the westerlies during stadial intervals, along with changes in SOc buoyancy fluxes. This is in part supported by proxy data showing precipitation- and vegetation changes in South America (Lamy et al., 1999; Moreno et al., 2012; Mayr et al., 2013; Montade et al., 2015; Quade and Kaplan, 2017), hydrographic sea surface changes south of Australia (De Deckker et al., 2012) and off Chile (Lamy et al., 2007), glacier retreats and -advances in the southern high-latitudes (Putnam et al., 2010), benthic foraminiferal communities in the South Atlantic responding to wind-driven cross-frontal mixing (Diz and Barker, 2015), and high-resolution dust- and water isotope records from Antarctic ice cores (Landais et al., 2015; Buizert et al., 2018). Although Quade and Kaplan (2017) suggest a southward shift of the SHW of ~8° during stadials, their estimates are associated with

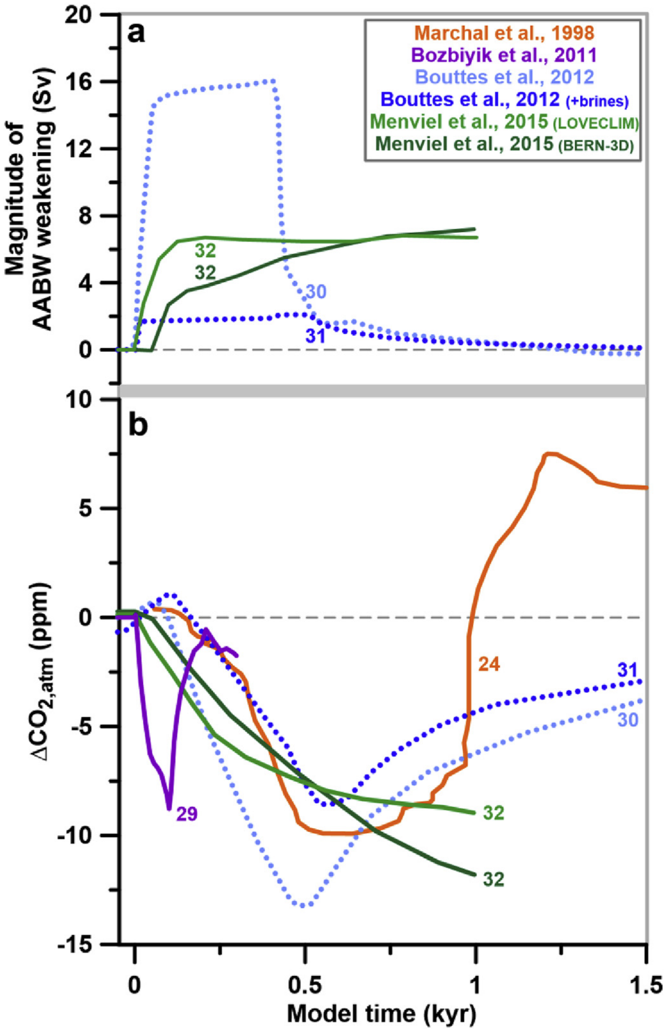

Fig. 12. Timeseries of simulated $CO_{2,atm}$ change and variations in Antarctic Bottom Water (AABW) formation in selected FW hosing experiments in the SOc. (a) Magnitude of AABW weakening, and (b) parallel change in simulated $CO_{2,atm}$ levels. Solid and dotted lines indicate simulations performed under interglacial and glacial climate boundary conditions, respectively. Numbers refer to Table 1, Tables S1 and S3, which list all details and references of the simulations.

large uncertainties ($1\sigma = {\sim}10°$) and remain to be confirmed.

2.3.2. SHW dynamics in climate models

The characteristics of the SHW under LGM boundary conditions vary widely across climate models. The intensity and position of the SHW were investigated in systematic and coordinated AOGCM simulations within the Paleoclimate Modelling Inter-comparison Project (PMIP) 2, PMIP3 and in PMIP-independent simulations (Menviel et al., 2008b; Rojas et al., 2009; Chavaillaz et al., 2013; Rojas, 2013; Sime et al., 2013, 2016; Liu et al., 2015; Kim et al., 2017). Simulations indicate either no consistent changes in wind intensity (e.g., Menviel et al., 2008b; Rojas et al., 2009; Chavaillaz et al., 2013; Rojas, 2013), a strengthening (e.g., Wyrwoll et al., 2000; Otto-Bliesner et al., 2006; Sime et al., 2013, 2016; Kim et al., 2017) or a weakening (e.g., Kim et al., 2002; Kim and Lee, 2009). Most of the PMIP2 and PMIP3 simulations support a slight weakening of the LGM SHW of 10–20% (Menviel et al., 2008b; Chavaillaz et al., 2013; Rojas, 2013), with the exception of the NCAR CCSM3 model that indicates a slight strengthening of ~10% (Otto-Bliesner et al., 2006) or larger (20–40%; Kim et al., 2002; Kim and Lee, 2009). The physical ocean model response to increased SHW intensities was reviewed by Gent (2016), and primarily shows an increase in SOc overturning, which is dampened by invigorated mesoscale eddy activity (i.e., eddy compensation). In addition, models suggest either no significant shift in the latitudinal position (Otto-Bliesner et al., 2006; Menviel et al., 2008b; Rojas et al., 2009; Chavaillaz et al., 2013; Rojas, 2013), a poleward or an equatorward displacement of the LGM SHW zonal maximum by 2–8° (e.g., Wyrwoll et al., 2000; Sime et al., 2013; Kim et al., 2017) or by 3–10° (e.g., Kim et al., 2002; Kim and Lee, 2009), respectively.

Toggweiler et al. (2006) conjecture a tight relationship between the position of the SHW and $CO_{2,atm}$ via deep convection in the SOc over past glacial cycles. Specifically, the superposition of the SHW core with the Antarctic Divergence propels Ekman-driven upwelling of CO_2-rich sub-surface water masses, and hence CO_2 outgassing, predicting a poleward and equatorward position of the SHW during interglacials and glacials, respectively (Toggweiler and Russell, 2008). During stadial conditions, the SHW winds were suggested to have shifted poleward in unison with the ITCZ (Anderson et al., 2009; Denton et al., 2010). The simulation of Chiang and Bitz (2005) that mimics NAtl stadial conditions shows no major changes in the SHW position, despite a pronounced southward shift of the ITCZ, whereas other studies point indeed at a strengthening and/or southward shift of the SHW during NAtl stadial conditions (Timmermann et al., 2005, 2007; Schmittner et al., 2007b; Lee et al., 2011; Pedro et al., 2018). Changes in the strength of the SHW in idealised stadial simulations were suggested to be large (~25%; Lee et al., 2011), while in other cases these were considered too small (<10%) to have a significant impact on the SOc carbon cycle (Schmittner and Lund, 2015). The results of Lee et al. (2011) were suggested to be an overestimation, because they are based on offline model simulations and unrealistically large prescribed cooling in the NAtl (Schmittner and Lund, 2015). In their simulations, simulated sea surface cooling in the NAtl (>10 °C) is much stronger than proxy records suggest (e.g., Cacho et al., 1999; Sachs and Lehman, 1999). Indeed, the SHW wind intensity changes seen by Lee et al. (2011) are large, when considering that the effect of removing the entire Antarctic Ice Sheet causes a SHW strengthening by ~25% only (Schmittner et al., 2011).

Inter-model differences regarding changes in the SHW wind intensity and -position during climate transitions may be related to the challenges simulating the SHW as a component of the Earth system. This is expressed in mismatches between the simulated and observed (i.e., present-day) seasonality and position of the SHW (Russell et al., 2006; Rojas et al., 2009; Swart and Fyfe, 2012; Wilcox et al., 2012). In addition, initial biases may curb the capacity of climate models to reliably simulate wind dynamics (Denton et al., 2010). Below, we discuss results from numerical model simulations of how and to what extent prescribed changes of the SHW may have influenced the past global carbon cycle.

2.3.3. Global carbon cycle response to changes in the SHW wind intensity

2.3.3.1. Overview of experimental design used in the compiled studies. We have compiled 18 model studies that have assessed the millennial-scale $CO_{2,atm}$ response to changes in the SHW wind strength in 167 separate simulations (Table 1, Table S4). All of these studies apply interglacial, i.e., either modern or pre-industrial, boundary conditions, with the exception of Winguth et al. (1999). The model simulations are performed with EMICs characterised by a simple and complex 3D ocean model component, as well as with OGCMs, but in some cases with highly simplified geometry (Table 1, Table S9). The exact region of adjusted wind fields may vary from a relatively narrow latitudinal band, i.e. 40°S–60°S (Menviel et al., 2008b), to a wider one, i.e., 30°S–70°S (Winguth et al., 1999;

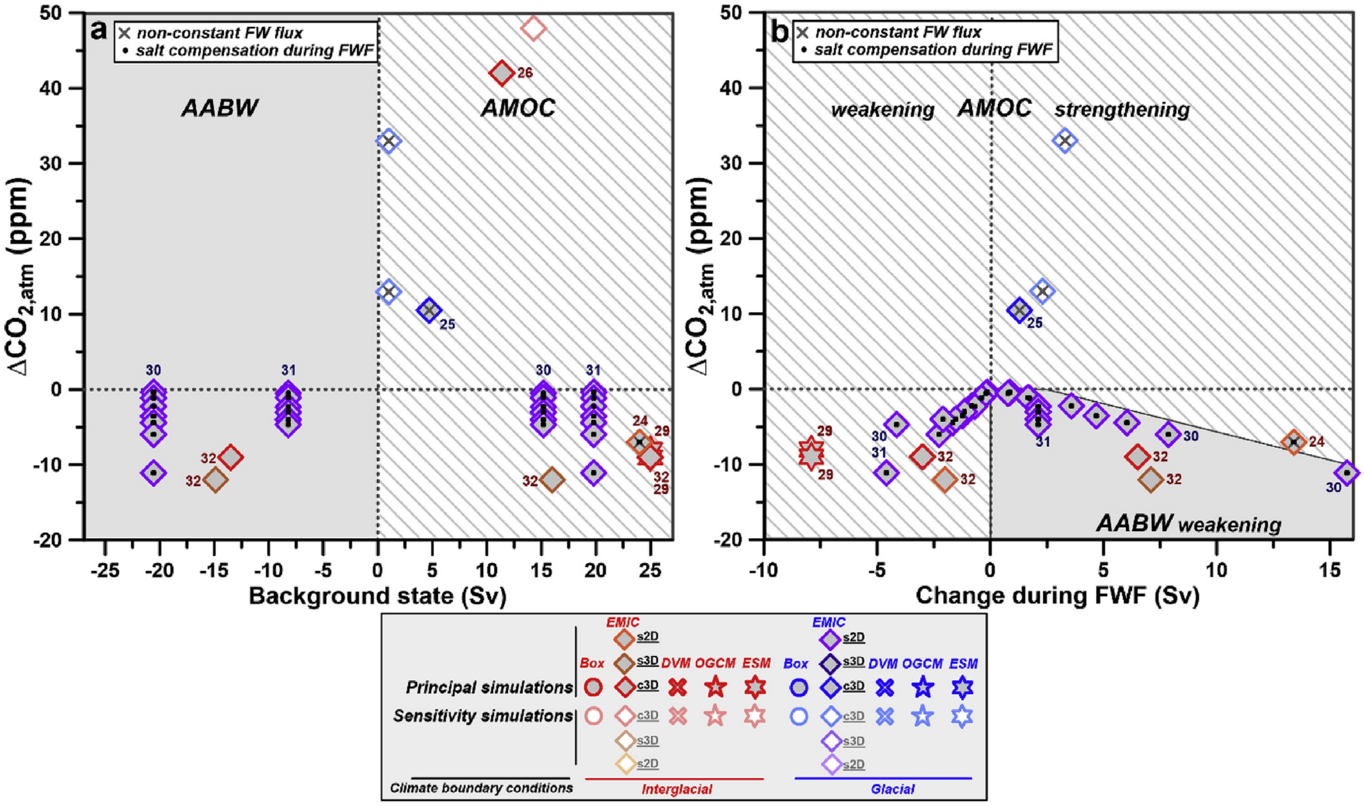

Fig. 13. Simulated changes in $CO_{2,atm}$ levels compared to variations of the AMOC and AABW in numerical models forced by FW hosing in the SOc. Changes in simulated $CO_{2,atm}$ changes versus (a) the background state of the AMOC (hatched area) and AABW (grey area) *prior to* FWF, and (b) the AMOC change (hatched area) and AABW decrease (grey area) *during* FWF. Symbols are identical to those used in Fig. 3. Symbols with centered black dots highlight simulations that apply global salt compensation during FW hosing. Symbols with crosses highlight simulations, which apply non-constant FW fluxes but centered-triangular or gradually increasing FW fluxes instead. Further details and references associated with the compiled model simulations are listed in Table 1, Tables S1 and S3.

Marinov et al., 2008a, 2008b; Tschumi et al., 2008; d'Orgeville et al., 2010; Lauderdale et al., 2013). As an extreme, Schmittner et al. (2007a) and Ödalen et al. (2018) considered a doubling and halving of the wind stress globally at the ocean- and sea ice surface. Lee et al. (2011) impose cooling in the NAtl in an AGCM to apply the resulting atmospheric wind field anomalies offline to an EMIC with a simple 3D ocean and carbon cycle model (MESMO; Table 1, Table S9).

Increases of the SHW wind intensity in numerical models can be induced through various ways, for instance by adjusting the wind stress, the wind speed and/or the moisture advection velocities (Rodgers et al., 2011; Schmittner and Lund, 2015). Changes of the SHW wind stress influence $CO_{2,atm}$ levels by impacting momentum transfer and ocean circulation, whereas wind speed additionally affects $CO_{2,atm}$ levels through changes in the air-sea exchange of CO_2 and heat fluxes (Rodgers et al., 2011; Schmittner and Lund, 2015). Most studies impose changes in the *zonal* wind component of the SHW by scaling the *wind stress* by a factor *f* varying between 0–5 (Fig. 3d, Table S4), but in some cases the *wind speed* is also adjusted (Menviel et al., 2008b), or both the zonal and meridional wind stress components are varied (Tschumi et al., 2011; Huiskamp et al., 2015). Some SHW wind intensity experiments are simultaneously forced with latitudinal shifts of the SHW (Lauderdale et al., 2013; Huiskamp et al., 2015), with variations of vertical diffusivity coefficients (Tschumi et al., 2008), with different representations of mesoscale eddies (Munday et al., 2014; Lauderdale et al., 2017) and with changes in the aeolian dust fluxes (Parekh et al., 2006b).

2.3.3.2. Simulated $CO_{2,atm}$ changes. Increasing (decreasing) the wind intensity of the SHW in numerical model simulations leads to an increase (decrease) in modelled $CO_{2,atm}$, and is generally consistent across different model hierarchies and experimental setups (Figs. 4c,d, 14a, Table S4). In fact, the compiled simulations broadly follow a polynomial fit, where the rate of simulated $CO_{2,atm}$ changes as function of the wind intensity scaling factor *f* is significantly smaller for $f > 2.5$, but larger for $f < 0.5$ (Fig. 14a). This is reproduced by individual studies that prescribe a large range of wind intensity scaling factors under identical boundary conditions and model setups (Fig. 14a; Tschumi et al., 2008, 2011; Munday et al., 2014). The 25%- to 75%-percentile range of simulated $CO_{2,atm}$ change is +11 to +38 (−26 to −4) ppm, when all 29 (23) principal interglacial simulations forced by increased (decreased) SHW wind intensities are combined, irrespective of whether the applied wind scaling factors are realistic or not (Table 2). Simulated $CO_{2,atm}$ change for less extreme scenarios of SHW intensity change ($f = 0.5–2$) can be approximated by a linear regression, which shows a $CO_{2,atm}$ increase of 3.2 ± 1.6 ppm for each 10% SHW strengthening and a $CO_{2,atm}$ decrease of -3.7 ± 1.5 ppm for each 10% SHW weakening (both statistically significant, $p < 0.05$; Table 2).

However, for a given wind intensity scaling factor *f*, the magnitude of simulated $CO_{2,atm}$ changes differs among simulations (Fig. 14a). For large (unrealistic) increases in the SHW wind intensity ($f > 4$), $CO_{2,atm}$ changes by +85 to +95 ppm or +45 to +56 ppm in the MITgcm (sector configuration), depending on the treatment of mesoscale eddies, i.e., parameterising or permitting eddies, respectively (Munday et al., 2014). Similarly, for a near-cessation of the SHW ($f = 0–0.05$), $CO_{2,atm}$ decreases by −67

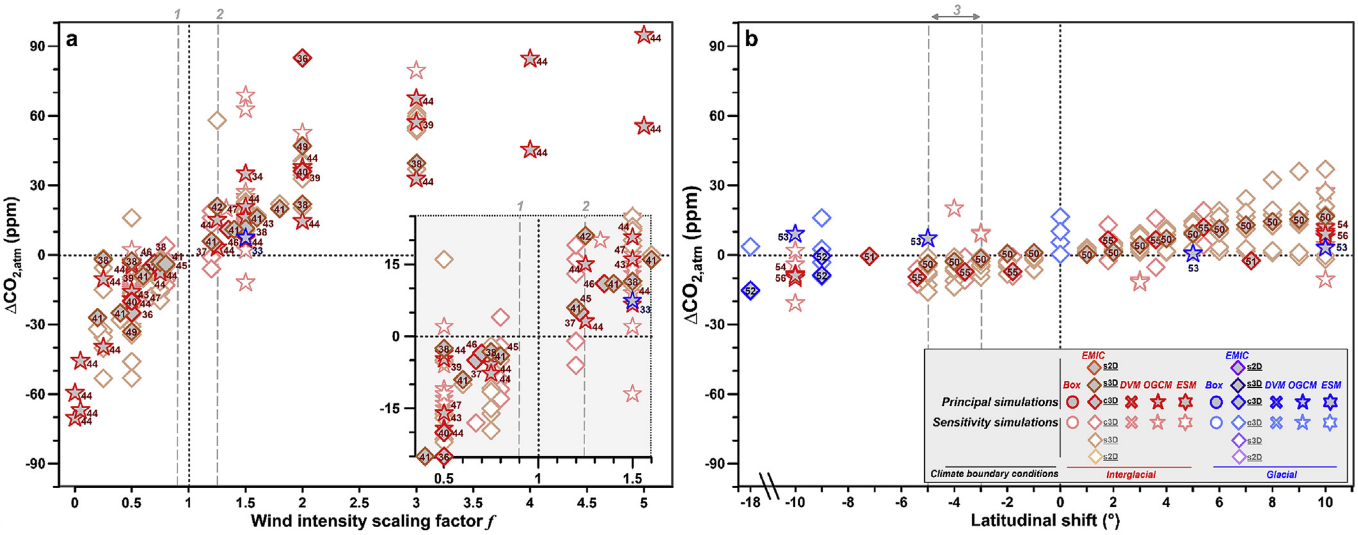

Fig. 14. Simulated $CO_{2,atm}$ response in numerical models forced by SHW wind changes. Changes in simulated $CO_{2,atm}$ shown as function of (a) changes in the (zonal and/or meridional) SHW wind intensity, i.e., wind scaling factor *f*, and (b) shifts in the latitude of maximum wind stress. Symbols are identical to Fig. 3. Numbers refer to individual model studies listed in Table 1, Tables S1, S4, and S5. Proxy data- and model-derived estimates of realistic changes of the SHW wind intensity and -position during stadials are shown as vertical dashed lines: 1) a 10%-weakening (Menviel et al., 2015b; Schmittner and Lund, 2015), 2) a 25%-strengthening (Lee et al., 2011), and 3) a southward displacement of the westerly winds by −3° to −5° (to be considered as upper limit, Kohfeld et al., 2013). Note that the x-axis in (b) is discontinuous. Inset in lower right corner in (a) shows $CO_{2,atm}$ response for small wind scaling factors in more detail. The legend in (b) applies to both panels.

to −70 ppm or −46 to −59 ppm with the MITgcm, depending on eddy representation (Munday et al., 2014). Halving the wind intensity may lead to a relatively small $CO_{2,atm}$ decrease of −3 to −5 ppm (Marinov et al., 2008b, 2008a; Tschumi et al., 2008; Munday et al., 2014) or a relative large $CO_{2,atm}$ decrease of −16 to −20 ppm (d'Orgeville et al., 2010; Lauderdale et al., 2013, 2017; Munday et al., 2014) (Fig. 14a, inset). A 50%-increase in the SHW wind intensity raises modelled $CO_{2,atm}$ relatively little by +7 to +11 ppm (Tschumi et al., 2008; Lauderdale et al., 2013; Munday et al., 2014) or much stronger by +16 to +35 ppm (Toggweiler et al., 2006; Lauderdale et al., 2013, 2017; Munday et al., 2014) (Fig. 14a, inset). A significantly larger $CO_{2,atm}$ increase compared to other models with similar wind scaling factor ($f = 1–2$) is observed in the study of Schmittner et al. (2007a) and Lee et al. (2011), showing a $CO_{2,atm}$ increase of +85 ppm and +58 ppm, respectively. This is because Schmittner et al. (2007a) impose increased wind stress globally at the ocean- and sea ice surface, and Lee et al. (2011) force MESMO (an EMIC) offline wind anomalies obtained with an offline AGCM; both forcings are likely unrealistically large.

2.3.3.3. Driving mechanisms. Increasing the SHW wind strength in coupled carbon cycle-climate models leads to enhanced Ekman pumping and vertical mixing in the SOc, which causes the upwelling of CO_2-rich sub-surface waters to the surface and increased CO_2 fluxes to the atmosphere (Winguth et al., 1999; Parekh et al., 2006b; Toggweiler et al., 2006; Schmittner et al., 2007a; Marinov et al., 2008a, 2008b; Menviel et al., 2008b; Tschumi et al., 2008; d'Orgeville et al., 2010; Lee et al., 2011; Tschumi et al., 2011; Lauderdale et al., 2013; Huiskamp et al., 2015; Lauderdale et al., 2017), and a lowering of the ocean's CO_2 solubility due to increased abyssal temperatures (Munday et al., 2014). These changes account for a $CO_{2,atm}$ increase in the models (Fig. 14a), although they are slightly buffered by increased export production given enhanced sub-surface nutrient supply (Winguth et al., 1999; Parekh et al., 2006b; Schmittner et al., 2007a; Menviel et al., 2008b; Tschumi et al., 2008; d'Orgeville et al., 2010; Lee et al., 2011; Tschumi et al., 2011) and enhanced vegetation growth on land through CO_2 fertilisation (d'Orgeville et al., 2010; Huiskamp et al., 2015). Some simulations suggest that a large proportion of the respired carbon released to the atmosphere originates from the mid-depth ocean (~500–2000 m), which is the depth interval on which the SHW winds exert the strongest impact (d'Orgeville et al., 2010; Munday et al., 2014; Huiskamp et al., 2015). In many cases, Antarctic sea ice changes are not considered or a sea ice response to SHW adjustments is disabled (Toggweiler et al., 2006; Lee et al., 2011; Tschumi et al., 2011; Lauderdale et al., 2013, 2017; Munday et al., 2014), therefore suppressing important processes such as wind-driven advection of sea ice or a sea ice influence on the SHW position (e.g., Morales Maqueda and Rahmstorf, 2002; Sen Gupta and England, 2006; Sime et al., 2016). A weakening of the SHW shows opposite trends in the simulations, lowering simulated $CO_{2,atm}$ (Fig. 14a).

Changes in the SHW wind intensity were shown to scale with ocean mixing in the North Pacific and the NAtl (Toggweiler et al., 2006; Tschumi et al., 2008, 2011), and with the formation of intermediate mode water in the SOc (Lauderdale et al., 2013; Huiskamp et al., 2015). However, for a lowering of the SHW wind stress to f=<0.5, the AMOC transitions abruptly into a collapsed state, which leads to a proportionally stronger decrease in $CO_{2,atm}$ than with active AMOC (Fig. 14a; Tschumi et al., 2011).

Differences in the $CO_{2,atm}$ response for a given wind scaling factor may be explained by the difference in the complexity of the numerical models (especially the grid spacing) and the experimental design, as well as the representation of internal processes such as the treatment of ocean biology and mesoscale eddies. Increasing SHW intensities leads to a greater nutrient supply to the surface, which promotes biological productivity and carbon export into the deep ocean, buffering the $CO_{2,atm}$ increase due to wind-driven Ekman-pumping by a factor of ~3 (Menviel et al., 2008b; Lee et al., 2011). This negative feedback is absent for instance in the study of Toggweiler et al. (2006), accounting for the larger $CO_{2,atm}$ change for a similar forcing. In addition, simulations with different model grid spacing (determining the nature of eddy representation, i.e., parameterising or permitting) show that an enhanced southward eddy-induced transport (eddy compensation) dampens the $CO_{2,atm}$ response, because it counteracts the impacts of enhanced

SHW winds on SOc upwelling (Lauderdale et al., 2013, 2017; Munday et al., 2014). However, all simulations use a relatively coarse ocean model resolution of ≥1/2° that cannot be considered as eddy-resolving. In fact, the ability of current coarse-resolution models to simulate localised features that determine SOc circulation dynamics such as AABW formation and the interference of ocean currents with topography is limited (Klocker, 2018). However, in a higher-resolution (*eddy-permitting*) OGCM (1/4°), Menviel et al. (2018) simulated ocean carbon loss that led to a $CO_{2,atm}$ rise of +20 ppm within 50 model years under interglacial boundary conditions, when the SHW are shifted southward *and* are intensified, confirming the simulated trends in other eddy-permitting and eddy-parameterising simulations.

Our compilation suggests that the impact of SOc upwelling and increased air-sea CO_2 fluxes on $CO_{2,atm}$ becomes progressively saturated in strong wind-scenarios, but amplified in weak wind-scenarios (Fig. 14a; e.g., Munday et al., 2014). To some degree, this is related to the effects of eddies that modify the sensitivity of SOc overturning to changes in wind stress through compensating meridional eddy-driven transport (i.e., eddy compensation) and 'absorption' of kinetic energy imposed by winds (i.e., eddy saturation) (e.g., Morrison and Hogg, 2013; Munday et al., 2014). Both also modify the effects of other feedback mechanisms involved in the interplay between wind-driven Ekman pumping and concomitant $CO_{2,atm}$ change (Munday et al., 2014). Specifically, in strong wind-scenarios, the residence time of CO_2- or DIC-rich water masses in the surface ocean decreases and their subduction rate becomes greater (Munday et al., 2014). Both increasingly act to decrease the efficiency of air-sea CO_2 equilibration and the release of carbon to the atmosphere, despite strong Ekman pumping. Additionally, the vertical extent of the water column that is directly affected by increased winds (through adjustments of the pycnocline depth) becomes saturated with increasing wind intensity, which leads to a nonlinear dependency between the rate of overturning and concomitant release of respired carbon (Munday et al., 2014). In weak wind-scenarios, the magnitude of simulated $CO_{2,atm}$ drop is amplified through accelerated increases in surface water residence times and reductions in the respired carbon content of upwelling water masses (via a shoaling of pycnocline depths), hence the deep ocean becomes increasingly, but non-linearly, isolated (Munday et al., 2014).

The representation of eddy effects (both adjustments in the eddy kinetic energy and meridional eddy transport) was shown to be crucial for SOc physics (e.g., Keeling and Visbeck, 2001; Hallberg and Gnanadesikan, 2006; Farneti and Delworth, 2010; Abernathey et al., 2011; Poulsen et al., 2018). The fact that most compiled simulations are not based on eddy-resolving ocean models and use constant thickness diffusivities (e.g., Gent and Danabasoglu, 2011; Gent, 2016) suggests that the simulated ocean- and carbon cycle response is likely biased. Additionally, for some simulations a sector model was used as a tradeoff for an enhanced (eddy-permitting) grid resolution (Munday et al., 2014; Lauderdale et al., 2017), whose ocean response may be different from global ocean models. Lastly, the sea ice response to SHW changes in the simulations is highly simplified (Winguth et al., 1999; Tschumi et al., 2008, 2011; Lee et al., 2011; Ödalen et al., 2018) or even absent (Munday et al., 2014; Lauderdale et al., 2017), which also introduces biases in simulated $CO_{2,atm}$ changes.

2.3.3.4. Model-predictions of past millennial-scale $CO_{2,atm}$ changes due to SHW intensity changes.

The contrasting SHW wind intensity changes during simulated stadial conditions signify that from a model perspective the behaviour of the SHW during past millennial-scale climate events remains poorly understood (see discussion in section 2.3.2.). In the cases of a 10%- (Pedro et al., 2018) and 25 %-SHW wind strengthening (Lee et al., 2011), the regression slope through all model simulations for $f = 1-2$ suggest a $CO_{2,atm}$ rise of 3 ± 2 ppm and ~8 ± 4 ppm, respectively (Table 2, Fig. 14a). For a <10% weakening of the SHW (Menviel et al., 2008b, 2015b; Schmittner and Lund, 2015), our linear regression model for $f = 0.5-1$ implies a $CO_{2,atm}$ decrease of up to ~4 ± 2 ppm (Table 2, Fig. 14a). These model outcomes would indicate that SHW changes alone can not be the main driver of $CO_{2,atm}$ changes over millennial timescales.

2.3.4. Global carbon cycle response of changes in the latitudinal position of the SHW

2.3.4.1. Overview of experimental design used in the compiled studies.

We have synthesised eight studies that have assessed the millennial-scale $CO_{2,atm}$ response to changes in the position of the SHW and that have presented 184 separate simulations (Table 1, Table S5). Most of these studies apply interglacial or pre-industrial boundary conditions, while two studies apply glacial or glacial-like climate background conditions (Huiskamp and Meissner, 2012; Völker and Köhler, 2013). The simulations were performed with EMICs both with a simple (Bern-3D) and a complex 3D ocean component (UVic-ESCM), and an OGCM with ocean biogeochemistry (MITgcm) (Table 1, Table S9). The models are forced by latitudinal shifts of the SHW in a particular latitudinal band by −18° to +10° (Fig. 3e), with prescribed transitions to unchanged wind fields north and south of this latitude band. Völker and Köhler (2013) shifted the position of the SHW wind belt, which also resulted in a ~50% increase in the wind stress for a 10°-southward shift. Some studies consider a combination of latitudinal SHW shifts with changes in the magnitude of the SHW wind stress (Tschumi et al., 2008; Lauderdale et al., 2013; Huiskamp et al., 2015), in vertical ocean diffusivities (Tschumi et al., 2008) and in AMOC strength through FWF in the NAtl (Huiskamp and Meissner, 2012).

2.3.4.2. Simulated $CO_{2,atm}$ changes.

Prescribing a northward (southward) shift of the SHW in coupled carbon-cycle climate models leads generally to an increase (decrease) of modelled $CO_{2,atm}$ levels (Fig. 14b, Table S5). The response is stronger under interglacial (with a 25%- to 75%-percentile range of +7 and + 12 (−9 to -2) ppm, n = 18 (13)) than under glacial background conditions (with a 25%- and 75%-percentile range of +1 and + 2 (−9 and +7) ppm, $n = 2$ (5); Table 2). Linear regressions of the interglacial model results indicate a $CO_{2,atm}$ increase (decrease) of 0.9 ± 0.4 (−0.6 ± 0.4) ppm per 1° northward (southward) shift of the SHW (Table 2). The number of existing simulations is insufficient to derive differences in simulated $CO_{2,atm}$ changes across different model hierarchies (Fig. 4e,f). Principal model simulations forced by large shifts of the SHW by ≥ 10° indicate a maximum $CO_{2,atm}$ change of −15 ppm and +16 ppm, respectively (Fig. 14b). These simulated $CO_{2,atm}$ changes due to extreme shifts in the SHW are much smaller than observed in simulations forced by extreme changes in the SHW wind intensity, which range between −70 and + 95 ppm (Fig. 14a).

Through sensitivity tests with step-changes in the position of the SHW, Tschumi et al. (2008) and Huiskamp et al. (2015) show that the $CO_{2,atm}$ response is nearly a linear function of the magnitude of latitudinal wind shift, for both northward and southward shifted SHW (Fig. 14b). This, however, may depend on the exact boundary conditions (Fig. 14b; Tschumi et al., 2008). The simulated $CO_{2,atm}$ increase in response to northward shifted SHW by Lauderdale et al. (2013, 2017) is consistent, yet slightly lower, than in the standard runs of Tschumi et al. (2008). For moderately northward (southward) shifted SHW by +5° (−5°), the simulated

$CO_{2,atm}$ change in two EMICs ranges between +9 and +12 (−10 to −4) ppm (Fig. 14b; Tschumi et al., 2008; Huiskamp et al., 2015). In contrast, d'Orgeville et al. (2010) show a small and consistently negative $CO_{2,atm}$ change (−0.5 to −2.5 ppm), despite prescribing a substantial shift of the SHW in their model by −7.2° and +7.2° (Fig. 14b).

In contrast to the interglacial simulations described above, OGCM simulations under glacial climate boundary conditions show an increase in $CO_{2,atm}$, i.e., by +0.5 to +3 ppm in the northward shifted SHW-scenarios (+5°, +10°), and by +7 to +9 ppm in the southward shifted SHW-scenarios (−5°, −10°) (Fig. 14b; Völker and Köhler, 2013). Shifting the SHW southward in simulations with an EMIC run under idealised H stadial boundary conditions leads to a decrease in $CO_{2,atm}$ levels by −1 to −9 ppm for a shift of −9° and by −15 ppm for an extreme shift of −18° (Fig. 14b; Huiskamp and Meissner, 2012), which is consistent with Tschumi et al. (2008) and Huiskamp et al. (2015), but inconsistent with Völker and Köhler (2013).

2.3.4.3. Driving mechanisms. A prescribed northward SHW shift enhances the outcrop area of deep water masses in the SOc (i.e., an increase in the width of the Antarctic Divergence Zone) and increases SOc vertical mixing, which increases the CO_2 flux from the ocean to the atmosphere, driving $CO_{2,atm}$ up (Tschumi et al., 2008; Lauderdale et al., 2013, 2017; Völker and Köhler, 2013; Huiskamp et al., 2015). These effects are buffered by increased export production due to enhanced sub-surface nutrient supply in the SOc (Tschumi et al., 2008; Lauderdale et al., 2013, 2017; Völker and Köhler, 2013; Huiskamp et al., 2015) and an increase in terrestrial carbon storage through CO_2 fertilisation (Huiskamp et al., 2015). It has been observed that ocean carbon is primarily lost from intermediate water levels (Huiskamp and Meissner, 2012; Lauderdale et al., 2013) or from the Pacific Ocean through changes in NPDW formation and -ventilation (Tschumi et al., 2008; Huiskamp and Meissner, 2012; Huiskamp et al., 2015) in northward shifted SHW scenarios. Some studies note increases in Antarctic sea ice cover (Völker and Köhler, 2013) and -thickness (Huiskamp et al., 2015) associated with northward shifts of the SHW, which sustains the formation of AABW (although site shifts may occur), and therefore promotes deep-ocean ventilation and the release of carbon from the ocean. Opposite trends are generally observed for southward shifted SHW, but in one study decreased export production dominates the simulated $CO_{2,atm}$ signal, accounting for an $CO_{2,atm}$ increase instead of a $CO_{2,atm}$ drop that is observed in the other simulations (Völker and Köhler, 2013). Low-amplitude $CO_{2,atm}$ changes in wind-shift scenarios were also associated with a massive carbon redistribution within the ocean, i.e., from the deep-ocean to the mid-depth (d'Orgeville et al., 2010) or between the Pacific and Atlantic oceans (Huiskamp and Meissner, 2012), causing only a small fraction of this carbon to be released from the ocean to the atmosphere.

The general trend of increasing (decreasing) $CO_{2,atm}$ concentrations for prescribed northward (southward) shifted SHW is inconsistent with the study of Toggweiler et al. (2006), which postulates $CO_{2,atm}$ minima, when the SHW are shifted northward. Toggweiler et al. (2006) supported their concept by idealised OGCM simulations that were forced by adjustments of the SHW *intensity*, assuming that latitudinal shifts and changes in the SHW intensity have equivalent impacts on SOc carbon cycling. Timmermann et al. (2014) suggested a strong dependence of the SHW wind intensity on obliquity-driven changes in meridional temperature gradients, and therefore predict a strengthening prior to the LGM and weakening of the westerlies during the last deglaciation, which is inconsistent with the proposals of Toggweiler et al. (2006), Anderson et al. (2009) and Denton et al. (2010). None of the simulations compiled here show a $CO_{2,atm}$ increase for poleward shifted SHW, as suggested by Toggweiler et al. (2006), except the study of Völker and Köhler (2013), which is the only study applying full glacial conditions. The simulations suggest an increase in $CO_{2,atm}$ levels by up to +10 ppm for southward shifted SHW, but due to different processes than those postulated by Toggweiler et al. (2006). Our model compilation also highlights that the assumptions made by Toggweiler et al. (2006) of equivalent effects of SHW wind shifts and -intensity changes on $CO_{2,atm}$ do not hold.

2.3.4.4. Model-predictions of past millennial-scale $CO_{2,atm}$ changes due to SHW shifts. Proxy-data compilations suggest a northward displacement of up to +5° of the SOc westerlies during the LGM with respect to modern (Kohfeld et al., 2013; Shulmeister et al., 2004). Considering this estimate as an upper bound for the southward displacement of the SHW during NAtl stadials, our regression model of all interglacial simulations compiled in this review predict a $CO_{2,atm}$ decrease of 3 ± 2 ppm, which contrasts with a generally positive trend of observed $CO_{2,atm}$ change during these time intervals. This estimate may be flawed, because the impact of latitudinal SHW shifts may be different under glacial boundary conditions and in numerical models with improved representation of wind- and mesoscale eddy dynamics. Indeed, Timmermann et al. (2010) found differences in the dynamics of atmospheric teleconnections during millennial-scale climate perturbations under different climate background conditions. The only full-glacial simulation in our compilation suggests that southward shifts of the SHW have likely contributed to observed $CO_{2,atm}$ increases during stadials by up to +7 ppm (Völker and Köhler, 2013). However, *transient* effects of SHW wind shifts on $CO_{2,atm}$ might be very different from the equilibrium simulations compiled here, which remains to be addressed.

It is also unknown how combined changes of the intensity and position of the SHW might have affected $CO_{2,atm}$ levels. SHW wind intensity changes were suggested to dominate the net $CO_{2,atm}$ change through their control on SOc vertical mixing and air-sea CO_2 fluxes (Lauderdale et al., 2013, 2017). Huiskamp et al. (2015) modelled that the $CO_{2,atm}$ response to combined changes in SHW intensity and -position is primarily determined by the direction of SHW shift, because their prescribed wind intensity change was much weaker (±20%) than applied in Lauderdale et al. (2013, 2017) (±50%), and hence the overall $CO_{2,atm}$ change is overwhelmed by the effects of SHW shifts. In contrast, Tschumi et al. (2008) found the simulated $CO_{2,atm}$ response in simulations to be essentially the superposition of the responses induced by the wind scaling and the shift separately. Accurate model-based predictions of the magnitude of $CO_{2,atm}$ variations therefore rely on an improved understanding of past changes of the SHW 'geometry' over millennial timescales, and a faithful representation of SHW dynamics in numerical models (both of which to date remain incomplete).

2.4. Antarctic sea ice

2.4.1. Proxy data constraints on past Antarctic sea ice changes

Sea ice can have an impact on $CO_{2,atm}$ levels by impeding air-sea gas exchange (e.g., Takahashi et al., 2009), and modulating biological nutrient utilisation and export production through light limitation (e.g., Oka et al., 2011; Buchanan et al., 2016), but also by supplying nutrients during sea ice melt (e.g., Sedwick and DiTullio, 1997). Moreover, sea ice affects the hydrography and circulation dynamics of the SOc through surface ocean buoyancy forcing and brine rejection (e.g., Iudicone et al., 2008; Abernathey et al., 2016; Sun et al., 2016).

Reconstructions of the past extent and seasonality of Antarctic sea ice are based on micro-palaeontological (e.g., diatom assemblages) or lithological proxies (e.g., IRD) (e.g., Armand et al., 2017). A first assessment of the Antarctic sea ice extent during the LGM suggested an expanded sea ice edge during summer and winter (CLIMAP project members, 1981). More recent compilations showed that winter sea ice expanded northward by 5–8° in latitude during the LGM (to ~45°S in the Atlantic and ~55°–62°S in the Indo-Pacific), while summer sea ice in the SOc may have expanded northward to the present-day winter sea ice edge (Gersonde and Zielinski, 2000) or may have remained unchanged (Crosta et al., 1998). Both observations would, however, be consistent with a greater seasonality of the Antarctic sea ice during the LGM compared to present-day. Abelmann et al. (2015) suggested that this increase in seasonality during the LGM was associated with distinct seasonal carbon- and opal export regimes that caused efficient $CO_{2,atm}$ drawdown. Spatially sparse marine proxy evidence is corroborated by sea ice-derived sea salt aerosol levels in Antarctic ice cores that suggest Antarctic-wide expansion of winter sea ice coverage and a significant increase in summer sea ice extent in the Atlantic sector of the SOc, despite caveats associated with a quantitative assessment due to variable rates of aerosol depletion depending on transport time (Wolff et al., 2006; Fischer et al., 2007a). Given the challenges of spatial analyses, little is known on the dynamics of Antarctic sea ice during millennial-scale climate events, despite some indications for winter-sea ice expansion and -retreat during intervals of millennial-scale Antarctic cooling (Bianchi and Gersonde, 2004; Ferry et al., 2015) and -warming (Shemesh et al., 2002; Fischer et al., 2007a; Collins et al., 2012), respectively.

2.4.2. Antarctic sea ice dynamics in climate models

Simulating sea ice processes is challenging, because sea ice depends on robust representations of ocean- and atmospheric temperatures, ocean currents and wind stress (e.g., Loose et al., 2014). Simulated changes in global sea ice thickness or -extent during the last decades are often inconsistent with observations (e.g., Shu et al., 2015). Similarly, although all PMIP climate models simulate an increase in Antarctic sea ice extent during the LGM, they suggest a different seasonality and extent of glacial Antarctic sea ice (e.g., Roche et al., 2012; Sime et al., 2016). They also show systematic differences in sea ice-related changes in surface ocean buoyancy forcing, SOc density stratification and vertical mixing (Marzocchi and Jansen, 2017). Initial biases in sea ice model components with respect to present-day sea ice characteristics propagate into simulated past climates (e.g., Roche et al., 2012). These biases may be associated with insufficiently represented sea ice physics and heat fluxes in the upper ocean as well as biases in ocean currents, and the position and vigour of the SHW (Goosse et al., 2013).

Sea ice can be coupled to the ocean and atmosphere through thermodynamic (i.e., heat exchange with ocean and atmosphere) and/or dynamical processes (e.g., through wind stress and ocean currents) (e.g., Hunke et al., 2010). Not all characteristics of complex sea ice dynamics are represented in the numerical models analysed here (Table S9). For instance, the role of sea ice in ocean biogeochemical cycles and winds (Sime et al., 2016), and the release and fate of brines during the formation of sea ice are insufficiently represented. In some cases very simple parameterisations are applied (e.g., Bouttes et al., 2010). Below, we elaborate on the role of Antarctic sea ice in marine carbon cycling and in $CO_{2,atm}$ changes as presented by numerical model simulations.

2.4.3. Global carbon cycle response to changes in Antarctic sea ice

2.4.3.1. Overview of experimental design used in the compiled studies. The role of sea ice in $CO_{2,atm}$ changes has been assessed in nine studies (Table 1; Table S6). A total of 148 separate simulations were performed with box models, EMICs and GCMs, mostly run under interglacial climate boundary conditions (Table S6). The forcing applied to induce changes in sea ice cover varies widely among the models. Most studies consider changes in the fractional sea ice cover and the position of the SOc sea ice edge through variations of air-sea gas exchange in the southern high latitudes (Fig. 3f,g; Stephens and Keeling, 2000; Archer et al., 2003; Kurahashi-Nakamura et al., 2007; Tschumi et al., 2008). Changes in sea ice cover are also implemented in models through variations of the sea ice albedo (Sun and Matsumoto, 2010) and the sinking of brines associated with sea ice formation (Bouttes et al., 2010, 2011). Accordingly, different metrics form the basis of the analyses of the model output (e.g., fractional or global sea ice cover, location of sea ice edge), which complicate an inter-model comparison (Fig. 15, Table S6). The simulations of Bouttes et al. (2010, 2011) and Chikamoto et al. (2012a) are the only simulations run under glacial climate boundary conditions.

2.4.3.2. Simulated $CO_{2,atm}$ changes. Prescribing and mimicking annually integrated Antarctic sea ice expansion (retreat) in numerical models (through adjustments of air-sea gas exchange, sea ice albedo or brine formation) leads generally to a decrease (increase) in simulated $CO_{2,atm}$ levels – the magnitude of which strongly dependents on the model type (Figs. 4g,h, 15; Archer et al., 2003). A combination of all 70 (15) model simulations, irrespective of the model complexity and experimental setup, indicates a 25%- to 75%-percentile range of −15 to 0 (−47 to −20) ppm under interglacial (glacial) climate background conditions of simulated $CO_{2,atm}$ change for more *expanded* Antarctic sea ice, respectively (Table 2, Table S6). For comparison, when Antarctic sea ice cover is forced to *decline* under interglacial climate boundary conditions, the 25%- to 75%-percentile range of $CO_{2,atm}$ change is slightly positive (+3 to +5 ppm; $n = 7$). A glacial simulation testing the impact of reduced Antarctic sea ice cover on $CO_{2,atm}$ levels shows a similar trend, namely a 4 ppm-$CO_{2,atm}$ increase (Chikamoto et al., 2012a).

In box models, expansion of Antarctic sea ice (i.e., impediment of air-sea gas exchange in the SOc box) leads to a decrease in $CO_{2,atm}$, the magnitude of which depends on the amplitude of the suppression of air-sea gas fluxes (Fig. 15). By prescribing year-round reduction of air-sea gas exchange, and hence *perennial* sea ice cover, in the SOc south of ~55°S, the simulated $CO_{2,atm}$ is reduced by −33 to −71 ppm (Stephens and Keeling, 2000; Archer et al., 2003, Fig. 15a). The result of Stephens and Keeling (2000) is qualitatively supported by a simulation of Sun and Matsumoto (2010), who show a 41 ppm-decrease in $CO_{2,atm}$ for a doubling in global fractional sea ice cover (invoked through sea ice albedo adjustments; Fig. 15b). Simulations with a more complex coupled sea ice-upper ocean model performed by Morales Maqueda and Rahmstorf (2002) support a contribution of sea ice changes to glacial $CO_{2,atm}$ minima by up to −56 ppm only. In simulations with expansive and perennial sea ice cover in some lower-sensitivity box models, a similar $CO_{2,atm}$ decline but with a much smaller amplitude of −1 to −7 ppm is observed (Archer et al., 2003). In contrast, various EMICs show a $CO_{2,atm}$ change of −4 to +3 ppm for the same forcing (Fig. 15a; Archer et al., 2003), which is in stark contrast with Stephens and Keeling (2000) and the lower-sensitivity box model results of Archer et al. (2003). GCM simulations, however, indicate a rise of $CO_{2,atm}$ by +1 to +26 ppm for more compact and expanded sea ice cover in the SOc imposed through modification of air-sea gas exchange and/or the rate of export production (Fig. 15a; Archer et al., 2003; Kurahashi-Nakamura et al., 2007).

The simulated $CO_{2,atm}$ results of Kurahashi-Nakamura et al. (2007) and Sun and Matsumoto (2010) are comparable on the basis of the reported position of the Antarctic sea ice edge, although

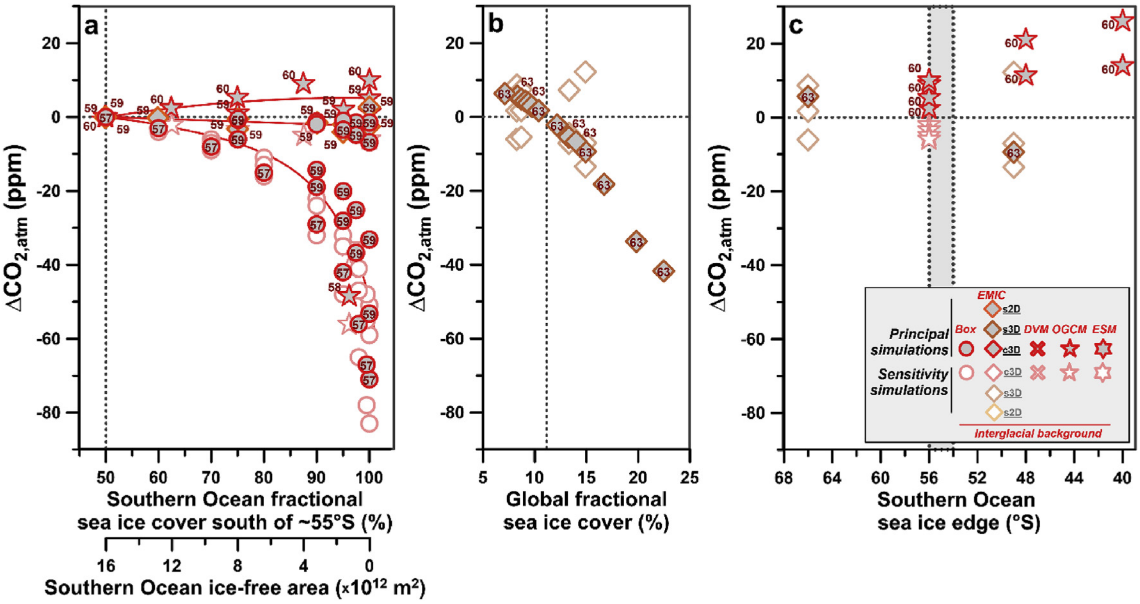

Fig. 15. Simulated $CO_{2,atm}$ in numerical models forced by changes in Antarctic sea ice cover. Shown as function of the fractional sea ice cover (a) in the SOc and (b) in the global ocean, as well as (c) the position of the SOc sea ice edge. Symbols are identical those used in Fig. 3. Red lines in (a) show a mean of "high-sensitivity" box models (definition by Archer et al., 2003), "low-sensitivity" box models (definition by Archer et al., 2003) as well as EMICs and OGCMs (from bottom to top). Vertical stippled lines show the fractional sea ice cover (a) in the SOc and (b) the global ocean, as well as (c) the position of the SOc sea ice edge as observed or prescribed in the control simulations. Please note that simulations with label 60 (Kurahashi-Nakamura et al., 2007) in (a) are also shown in (c). Experiments with label 63 (Sun and Matsumoto, 2010) in (b) are also shown in (c). Numbers refer to Table 1, Tables S1 and S6, which list details and references of the individual simulations. The legend in (c) applies to all panels.

both apply fundamentally different forcing mechanisms through adjustments of gas exchange rates and export production as well as the sea ice albedo, respectively. Their results appear mutually exclusive (Fig. 15c): while a northward shifting SOc sea ice edge is associated with a $CO_{2,atm}$ increase in Kurahashi-Nakamura et al. (2007), it is linked with a $CO_{2,atm}$ drop in Sun and Matsumoto (2010). Similarly, opposite trends between these two studies are observed for a southward shifting Antarctic sea ice edge.

2.4.3.3. Driving mechanisms. Based on box model simulations, highly-idealised sea ice-driven changes in air-sea gas exchange were suggested to have drawn down $CO_{2,atm}$ significantly at the LGM (Stephens and Keeling, 2000). Prescribing *year-round* reductions in air-sea gas exchange in the SOc very likely leads to an unrealistic capping-off of the SOc and the deep ocean from the atmosphere, as summer sea ice expansion northward was shown to be limited (Crosta et al., 1998; Gersonde and Zielinski, 2000), and may hence lead to overestimations of the sea ice impact on $CO_{2,atm}$ levels on both glacial-interglacial and millennial timescales. However, similar trends are observed in a more complex and fully coupled ocean-atmosphere-sea ice GCM with a seasonal representation of sea ice dynamics (Ferreira et al., 2018). Stephens and Keeling (2000) justify their prescribed changes by implying year-round Antarctic sea-ice cover, or wintertime coverage combined with sea ice melting-induced stratification during summer. Their prescribed forcing leads to reduced air-sea gas equilibration and reduced ventilation of the deep ocean, leading to increased ocean carbon storage, and a large decrease in $CO_{2,atm}$ of up to −71 ppm, equivalent to the impact of SOc stratification postulated by Toggweiler (1999). These findings were suggested to overestimate the role of sea ice in glacial-interglacial $CO_{2,atm}$ variations, based on simulations with a sea ice-upper ocean model with more realistic representations of the dissipation and deformation of sea ice by winds and a seasonal sea ice cycle (Morales Maqueda and Rahmstorf, 2002). These simulations show a larger ice free region under glacial conditions, and hence suggest a weaker contribution of sea ice to glacial $CO_{2,atm}$ minima (Morales Maqueda and Rahmstorf, 2002).

A significant challenge to the large effect of sea ice on $CO_{2,atm}$ is posited by the studies of Archer et al. (2003) and Broecker and Peng (1986), who used the same experimental setup as in Stephens and Keeling (2000) but applied various model hierarchies. Archer et al. (2003) suggest an overrepresentation of high-latitude processes in the box model of Stephens and Keeling (2000), which in turn also implies the lack of important feedback mechanism such as wind-sea ice feedbacks, light limitation of ocean productivity, compensating effects from low-latitude export production and ocean CO_2 solubility variations. In other simulations with more complex OGCMs and an EMIC with more realistic biogeochemistry- and sea ice components, it was shown that the effects of sea ice on reducing air-sea gas exchange (tending to decrease $CO_{2,atm}$) and inhibiting biological production (tending to increase $CO_{2,atm}$) largely cancel each other out (Kurahashi-Nakamura et al., 2007; Sun and Matsumoto, 2010; Chikamoto et al., 2012a). In fact, the bulk of $CO_{2,atm}$ change in the study of Sun and Matsumoto (2010) results from an increase in CO_2 solubility due to colder temperatures in sea ice-covered areas rather than inhibition of air-sea gas exchange. Ridgwell (2001) pointed out that increased Antarctic sea ice cover leads to reduced export production in the SOc but through advection of nutrients through the thermocline this is compensated via increased equatorial export production (having only a small net effect on simulated $CO_{2,atm}$ levels). This feedback was not considered in Stephens and Keeling (2000) due to the lack of an equatorial surface box in their model. Therefore, most of the disparate $CO_{2,atm}$ response across model hierarchies comes down to the different processes considered and the reliability with which they are represented. This leaves the role of sea ice in millennial- or orbital-scale $CO_{2,atm}$ changes from a model-standpoint insufficiently constrained.

A different approach to test the effect of sea ice on $CO_{2,atm}$ was chosen by Bouttes et al. (2010, 2011), who in glacial simulations with CLIMBER-2 successively increased the amount of brines associated with sea ice formation, focusing on the impact of sea ice on density stratification of the ocean interior. This experimental setup is highly idealised, because carbon and salt are directly transferred from the surface to the deep ocean in the simple ocean component of CLIMBER-2. Prescribing a larger fraction of sea ice brines that reaches the deep ocean enhances the salinity and isolation of the deep ocean, and promotes a stronger density stratification of the water column (vertical ocean diffusivities remain, however, unaffected), which causes a drop in $CO_{2,atm}$ by up to 50 ppm (Bouttes et al., 2010, 2011). This is supported by model simulations that have indicated a significant impact of sea-ice related changes in the density structure of the SOc, and hence in deep-ocean carbon storage, on glacial-interglacial $CO_{2,atm}$ change (Gildor and Tziperman, 2001; Gildor et al., 2002; Paillard and Parrenin, 2004; Jansen, 2017). However, prescribed salinification of deep waters in the SOc in OGCM simulations of Kobayashi et al. (2015) leads to stronger AABW overturning, driving $CO_{2,atm}$ up by +5 ppm. This is largely due to a decline of the residence time of deep-waters, in contrast to the findings of Bouttes et al. (2011). As brine rejection below sea ice and the dynamics of AABW formation are sub-gridscale phenomena and are not sufficiently represented in numerical models, the impact of sea ice dynamics and associated brines on millennial-scale $CO_{2,atm}$ changes remains an important aspect that needs to be further tested in coupled carbon cycle-climate models.

2.5. Aeolian dust supply to the ocean

2.5.1. Proxy data constraints on past changes in aeolian dust supply to the ocean

Air-borne dust influences the Earth's radiative budget (Ridgwell and Watson, 2002; Jickells et al., 2005; Maher et al., 2010), for instance through scattering and absorbing solar radiation (e.g., Miller and Tegen, 1998; Miller et al., 2004) and influencing cloud formation, with consequences for the albedo and the hydrological cycle (e.g., Mahowald and Kiehl, 2003; Spracklen et al., 2008). In addition, the supply of dust, in particular to high-nutrient low-chlorophyll (HNLC) regions such as the SOc, has been shown to affect marine biogeochemical cycles, and hence $CO_{2,atm}$ levels (Ridgwell and Watson, 2002; Jickells et al., 2005; Martínez-García et al., 2014; Tagliabue et al., 2017), for instance through i) a control on export production and nutrient utilisation (e.g., Martin et al., 1990; de Baar et al., 1995; Cassar et al., 2007), ii) the fixation of nitrogen and the availability of nitrate at the surface ocean (e.g., Falkowski, 1997; Tagliabue et al., 2008), iii) changes in ecosystem stoichiometries (e.g., Hutchins and Bruland, 1998; Pichevin et al., 2014; Person et al., 2018), and iv) variations in community structures (e.g., Archer and Maier-Reimer, 1994; Bopp et al., 2003). Dust supply in the SOc may therefore also impact on low-latitude export production through determining the nutrient content and -composition, in particular the silicic acid concentration, of waters exported to equatorial regions (a process known as silicic acid leakage; Brzezinski et al., 2002; Matsumoto et al., 2002). On the other hand, climate itself modulates the availability (through aridity and vegetation cover), mobilisation (through windiness and gustiness) and deposition (through precipitation) of dust and iron in the global ocean (Mahowald et al., 1999, 2006; Kohfeld and Harrison, 2001; Ridgwell, 2003; Fischer et al., 2007b; Shoenfelt et al., 2018). In addition to aeolian dust, other sources of iron to the surface ocean include upwelling of sub-surface waters (de Baar et al., 1995; Latimer and Filippelli, 2001; Blain et al., 2007; Tagliabue et al., 2014b), iceberg- and sea ice melting (e.g., Sedwick and DiTullio, 1997; Raiswell et al., 2008; Raiswell and Canfield, 2012), glacial outwash sediments (Sugden et al., 2009), and hydrothermal plumes at ocean ridges (e.g., Tagliabue et al., 2010; Saito et al., 2013). Furthermore, lowered sea level may significantly reduce the supply of sedimentary iron from shelf areas to the ocean, partially compensating the effects of increased aeolian dust fluxes (Muglia et al., 2017). Changes in iron sources and their output may have a significant impact on the marine carbon cycle (Tagliabue et al., 2014a, 2017), but their relative contributions to the dissolved iron inventory of the ocean remain unknown.

During the LGM, dust fluxes are estimated to have been up to 2 to 5 times higher globally (e.g., Rea, 1994; Kohfeld and Harrison, 2001; Maher et al., 2010; Lambert et al., 2015; Kienast et al., 2016). Glacial dust fluxes to Antarctica were found to have increased 20–30 fold (e.g., Lambert et al., 2008, 2013). However, these estimates cannot directly be translated into past atmospheric dust load changes due to temporally changing dust transport- and deposition schemes (e.g., Fischer et al., 2007a; Markle et al., 2018). Nonetheless, Winckler et al. (2008) showed a tight correspondence between dust fluxes in the Equatorial Pacific with those in Antarctica, indicating that climate-related changes in dust flux may have changed globally. During millennial-scale climate events, the supply of Fe-bearing dust to the SOc has varied substantially (e.g., Fischer et al., 2007a; Lambert et al., 2012; Anderson et al., 2014; Martínez-García et al., 2014). Dust flux estimates in the South Atlantic show that changes likely did not exceed a factor of four (Anderson et al., 2014; Martínez-García et al., 2014). Changes in aeolian dust supply during millennial-scale climate variability are thought to have altered the nutrient utilisation efficiency and export production patterns in the SOc, and hence influenced $CO_{2,atm}$ concentrations via their leverage on the efficiency of the biological carbon pump of the ocean (Ziegler et al., 2013; Anderson et al., 2014; Martínez-García et al., 2014; Gottschalk et al., 2016; Jaccard et al., 2016).

2.5.2. Variations in aeolian dust fluxes in climate models

Early numerical models have addressed the influence of iron on the ocean carbon cycle, and hence $CO_{2,atm}$ through simple parameterisations only (given the lack of an implementation of the ocean iron cycle in these models), for instance by prescribing changes in surface ocean nutrient concentration/utilisation in order to mimic dust-driven iron fertilisation of marine phytoplankton (Joos et al., 1991; Peng and Broecker, 1991; Sarmiento and Orr, 1991; Kurz and Maier-Reimer, 1993). These early simple models were designed to quantify the extreme upper-limit impact of iron fertilisation, and yield an upper limit of the simulated drop in $CO_{2,atm}$ between −34 and −59 ppm (Joos et al., 1991; Peng and Broecker, 1991; Kurz and Maier-Reimer, 1993).

The complexity of the Fe cycle realisation varies among the models compiled here, but all simulate Fe cycle dynamics explicitly. They consider the iron input into the ocean via dust (e.g., Watson et al., 2000) or additional non-aeolian sources (e.g., Parekh et al., 2008; Tagliabue et al., 2014a), particle remineralisation in the ocean, as well as variations in the solubility, bioavailability (e.g, ligand concentration), scavenging, and photosynthetic uptake of Fe in the ocean; the latter is parameterised as function of light, as well as nutrient- and iron concentrations, with a preset or variable molar Fe:C ratio (Parekh et al., 2006b, 2008; Oka et al., 2011). Numerical models within the Iron Model Inter-comparison Project FeMIP show large differences in the residence time of Fe in the ocean (by two orders of magnitude), in the relative fractions of aeolian and non-aeolian dust sources, and in the distribution of dissolved iron in the ocean that mismatch with observations (Lambert et al., 2015; Tagliabue et al., 2016). Improving the representation of the iron cycle in models, for instance through prognostic modelling of ligands (Völker and Tagliabue, 2015), incorporating iron speciation (Tagliabue and Völker, 2011), and accounting for other non-aeolian iron sources to the ocean (Tagliabue et al., 2009a), as well as gaining more insights into the ocean's iron cycle and biogeochemistry from field experiments (e.g., Boyd et al., 2007) will help furthering our understanding of the role of dust on the global carbon cycle.

Numerous model simulations were performed to understand the dynamics of aeolian dust during the LGM (e.g., Mahowald et al., 1999, 2006; Lunt and Valdes, 2001, 2002; Werner et al., 2002; Takemura et al., 2009; Albani et al., 2016), but there is a paucity of simulations assessing the spatial variability of aeolian dust supply on millennial timescales (Albani et al., 2016). Through accounting for changes in dust mobilisation, -transport and -deposition, Mahowald et al. (1999) showed that globally the LGM atmosphere experienced 2.5 times higher dust loading than at present-day, due to more vigorous winds, a weaker hydrological cycle, a decline in terrestrial vegetation and expanded regional dust sources. In contrast, Lunt and Valdes (2002) suggested a 1.5 times stronger dust loading in the LGM atmosphere compared to present-day, and a weaker contribution from North African sources to LGM dust fluxes as compared to the study of Mahowald et al. (1999). By including glaciogenic sources of dust and CO_2 fertilisation changes of land vegetation, Mahowald et al. (2006) simulated a 3.3-times increase in global atmospheric dust fluxes during the LGM compared to modern.

There is an incomplete understanding of dust flux changes during millennial-scale climate events as the number of existing simulations is low (e.g., transient simulations of Parekh et al. (2008)). Numerical models are often forced by (independently) simulated global LGM dust fluxes to assess the role of changes in aeolian dust supply in $CO_{2,atm}$ variations. However, differences in simulated LGM dust dynamics translate into different dust loading maps used to force numerical models. For instance, dust loadings applied to the LGM surface ocean were based on Mahowald et al. (1999) in some coupled carbon cycle-climate simulations (Bopp et al., 2003; Parekh et al., 2006b), on Mahowald et al. (2006) in others (Tagliabue et al., 2009b; Menviel et al., 2012) and on Takemura et al. (2009) in Oka et al. (2011). Related to the application of these different baseline dust loading maps, different global or SOc dust scaling factors (f_{global} or f_{SOc}, respectively) are considered to represent the LGM with reference to modern, for instance $f_{global} = 1.75$ (Bopp et al., 2003), $f_{global} = 2$ (Lefèvre and Watson, 1999; Watson and Lefèvre, 1999), $f_{global} = 5.5$ (Parekh et al., 2006a, 2006b), or $f_{SOc} = 20$ (Lefèvre and Watson, 1999; Oka et al., 2011). The dust loading factor f indicates the mean magnitude of prescribed dust flux changes to the ocean with reference to modern dust fluxes. Here, we analyse these model simulations with the motivation of identifying the possible *maximum* influence of aeolian dust flux variations on millennial-scale $CO_{2,atm}$ variability.

2.5.3. Global carbon cycle response to changes in aeolian dust transport

2.5.3.1. Overview of experimental design used in the compiled studies. We have assessed the simulated $CO_{2,atm}$ response to changes in the supply of aeolian dust to the ocean in 14 studies (Table 1; Tables S6 and S7), which present 101 separate model simulations performed with box models (Lefèvre and Watson, 1999; Watson and Lefèvre, 1999; Watson et al., 2000; Ridgwell, 2003), EMICs (Parekh et al., 2008; Bouttes et al., 2011; Watson et al., 2015), OGCMs with ocean biogeochemistry (Parekh et al., 2006a, 2006b), OBGMs (Bopp et al., 2003; Tagliabue et al., 2009b, 2014a; Lambert et al., 2015) and an ESM (Oka et al., 2011). Most of the simulations were run under pre-industrial/modern climate boundary conditions, while few studies also apply glacial climate boundary conditions (Lefèvre and Watson, 1999; Bopp et al., 2003). The experimental setup is very similar in most studies: dust fluxes to the surface of the global ocean or to specific ocean regions (e.g., SOc) are increased (Fig. 3h), with assumptions made on the Fe content of aeolian dust (3.5%), the solubility of Fe in the ocean (which ranges between 0.5% and 10% in the compiled simulations) and the character of the molar Fe:C ratio (constant or variable as function of Fe concentrations, and/or the light availability). The ligand concentration and -strength are additionally varied (Parekh et al., 2006b, 2008; Tagliabue et al., 2014a). Some studies impose the degree of nutrient utilisation efficiency in the surface ocean (rather than simulating Fe cycling directly) to *mimic* varying aeolian supply of iron to the surface ocean (Bouttes et al., 2011; Watson et al., 2015).

2.5.3.2. Simulated $CO_{2,atm}$ changes. Simulations forced with increased dust fluxes to the global ocean combined show a decrease in $CO_{2,atm}$ with a 25%- to 75%-percentile range of −43 to −19 ppm and −29 to −16 ppm, when performed under interglacial ($n = 36$) and glacial boundary conditions ($n = 5$), respectively (Fig. 16). The magnitude of this $CO_{2,atm}$ decrease is proportional to the dust loading factor f_{global} (Fig. 16; Lefèvre and Watson, 1999; Watson and Lefèvre, 1999; Parekh et al., 2006a, 2006b), with a maximum $CO_{2,atm}$ decrease of −50 ppm for $f_{global} = 10$ (Fig. 16; Lefèvre and Watson, 1999; Watson and Lefèvre, 1999). However, there is a marked difference in the magnitude of simulated $CO_{2,atm}$ drop between box models and OGCMs/ESMs (Fig. 4i,j). Linear regression of all box model simulations for $f_{global} = 1–2$ suggests a −17 ± 11 ppm change in $CO_{2,atm}$ per doubling of global dust fluxes (Lefèvre and Watson, 1999; excluding Ridgwell, 2003), whereas for all OGCM and ESM simulations it suggests a −8±7 ppm change in $CO_{2,atm}$ only (Table 2). Decreased dust fluxes to the global ocean, i.e., $f_{global} = 0–0.5$, lead to a substantial increase in $CO_{2,atm}$ by up to +181 ppm, when dust fluxes are set to zero (Fig. 16; Parekh et al., 2006a, 2006b), but show only a small increase of +2 ppm in Tagliabue et al. (2014a). In simulations forced with increased dust fluxes to the SOc, the $CO_{2,atm}$ decrease is limited to −10 ppm (Parekh et al., 2008). This contrasts with the box model simulations of Watson et al. (2000) that show a 40 ppm $CO_{2,atm}$ decrease for $f_{SOc} = 25$ (Fig. 16). The 25% to 75%-percentile range of all SOc simulations is −2.5 to −10 ppm ($n = 12$). Nonetheless, simulated $CO_{2,atm}$ levels decrease as function of f_{global} and f_{SOc}, when both are larger than 1. Both $CO_{2,atm}$ records show asymptotic behaviour, which is more evident in the simulations that prescribe changes in SOc dust fluxes (Fig. 16).

Our model compilation shows that there are large differences in the modelled $CO_{2,atm}$ response of up to ~20 ppm for $f_{global} = 1.5–2$ (Fig. 16a, inset). While the MITgcm (with ocean biogeochemistry and Fe cycle incorporated) shows a small $CO_{2,atm}$ decline for this f_{global} range ($\Delta CO_{2,atm} = -2$ to -4 ppm; Parekh et al., 2006a, 2006b), the 10-box model PANDORA, the 14-box model of Ridgwell (2003), OBGMs and an ESM indicate a larger $CO_{2,atm}$ decline of −9 to −40 ppm (Fig. 16; Lefèvre and Watson, 1999; Bopp et al., 2003; Ridgwell, 2003; Tagliabue et al., 2009b; Oka et al., 2011). Given the low number of simulations run under glacial climate boundary conditions (Fig. 16), differences in the $CO_{2,atm}$ response to aeolian dust fluxes between interglacial and glacial climate cannot be determined.

Sensitivity studies have assessed the impact of dust-driven changes in the Fe:C ratio of exported organic matter on $CO_{2,atm}$, and show negligible impact on simulated $CO_{2,atm}$ compared to simulations with fixed Fe:C ratios (Lefèvre and Watson, 1999; Watson and Lefèvre, 1999; Table S7). In contrast, an increased

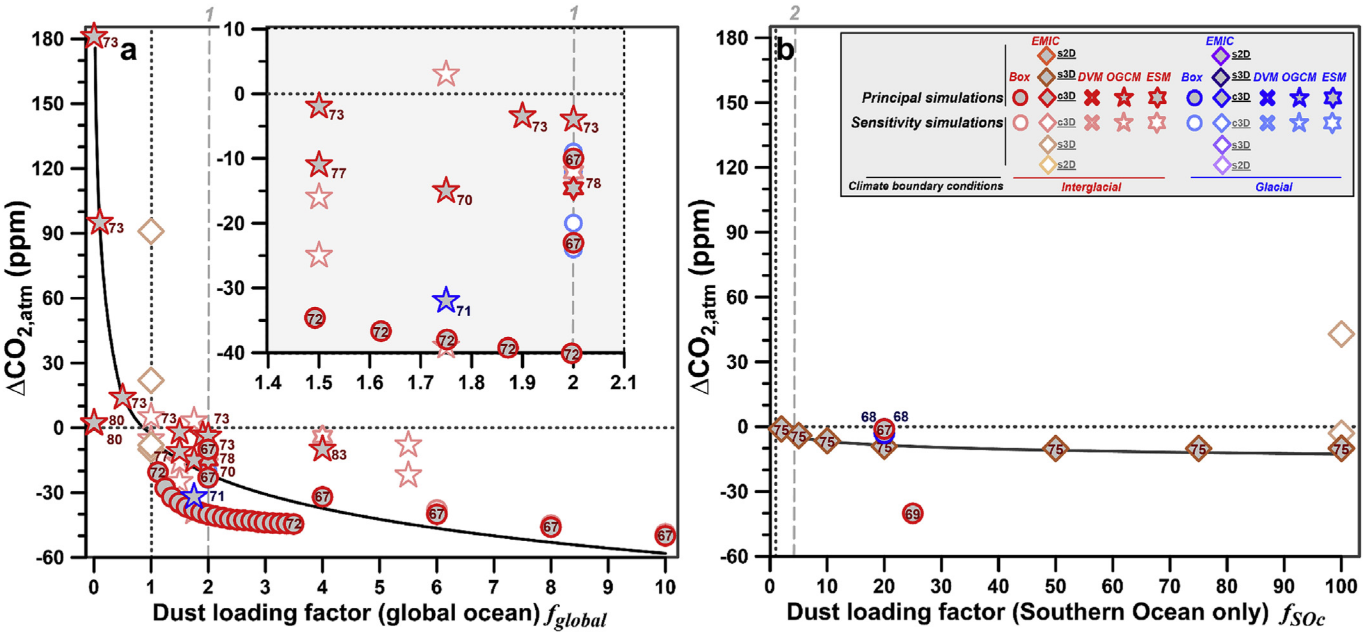

Fig. 16. **Simulated $CO_{2,atm}$ changes in numerical models forced by variations in aeolian dust supply to the ocean.** Shown for variations in dust fluxes to the (a) global ocean and (b) the SOc as function of the mean dust scaling factor f_{global} and f_{SOc}, respectively. This factor indicates the magnitude of prescribed dust flux changes to the ocean with reference to modern dust fluxes. Symbols are identical to Fig. 3. Black lines show a logarithmic fit through all principal simulations. Numbers refer to Table 1, Tables S1 and S7, which list further information and references of the individual simulations. Vertical dashed lines show proxy data- and model-based estimates of realistic changes of dust fluxes in the past: 1) a doubling of global ocean dust fluxes at the LGM, i.e., $f_{global} = 2$ (e.g., Mahowald et al., 1999; Kohfeld and Harrison, 2001; Kienast et al., 2016), and 2) a fourfold increase of dust fluxes to the SOc, i.e., $f_{SOc} = 4$ (Anderson et al., 2014; Martínez-García et al., 2014). These may, given the absence of better estimates, serve as indication for the *maximum* influence of aeolian dust fluxes to the ocean on $CO_{2,atm}$ during millennial-scale climate variability. The legend in (b) applies to both panels.

ligand concentration in the ocean leads to an increased $CO_{2,atm}$ drawdown by a factor of ~3, when dust fluxes are enhanced (Parekh et al., 2006a, 2006b, 2008; Tagliabue et al., 2014a; Table S7).

Increasing dust loadings in the surface ocean in regions outside the SOc, including the Equatorial or North Pacific, leads to a small $CO_{2,atm}$ decrease only ($\Delta CO_{2,atm} < -4$ ppm; Oka et al., 2011; Parekh et al., 2008), which is significantly smaller than the $CO_{2,atm}$ drop associated with dust fluxes in the SOc (Fig. 16). The only exception to this observation is the −12 ppm drop in $CO_{2,atm}$ resulting from enhanced dust fluxes in the entire Pacific Ocean (Oka et al., 2011; Table S7).

2.5.3.3. Driving mechanisms. The simulated $CO_{2,atm}$ decrease resulting from increased aeolian dust fluxes to the global and SOc is caused by iron fertilisation of marine biota, and hence both a stronger and more efficient biological carbon pump (Watson et al., 2000, 2015; Bopp et al., 2003; Ridgwell, 2003; Parekh et al., 2008; Tagliabue et al., 2009b; Bouttes et al., 2011). Other processes by which $CO_{2,atm}$ was suggested to decrease owing to increased iron fluxes include an ecosystem shift towards more siliceous phytoplankton (or in fact, a different species composition), changes in the abundance of silicifying organisms, a change of the $CaCO_3$:C_{org} rain ratio and an increase in surface ocean alkalinity (Bopp et al., 2003; Tagliabue et al., 2014a). The simulated $CO_{2,atm}$ range in the compiled studies is consistent with transient simulations of past glacial cycles that support both the lower ($\Delta CO_{2,atm} = -10$ ppm; Menviel et al., 2012) and upper end of this range ($\Delta CO_{2,atm} = -22$ to −52 ppm; Ridgwell, 2001, 2003; Brovkin et al., 2012; Ganopolski and Brovkin, 2017). The inter-model difference may partly be related to how ligands are treated in the ocean biogeochemistry model component (Ridgwell, 2003), whether non-aeolian dust sources to the surface ocean are considered (Tagliabue et al., 2014a; Lambert et al., 2015) and how complex the ecosystem model is (Table S9). In some simulations, dust-driven changes in export production in the SOc lead to a reduced nutrient supply to the equatorial region, lowering export production, and therefore causing a small net $CO_{2,atm}$ change only (Tagliabue et al., 2009b; Lambert et al., 2015). The simulated asymptotic $CO_{2,atm}$ change as function of aeolian dust fluxes can be explained by negative feedbacks and other limiting factors of ocean productivity, particularly in the SOc, that are not alleviated by the addition of iron, such as sea ice cover, light, and the availability of other nutrients (Watson et al., 2000; Ridgwell and Watson, 2002; Parekh et al., 2006a, 2006b).

The insensitivity of $CO_{2,atm}$ to aeolian dust fluxes to the Atlantic (Oka et al., 2011) or distinct regions of the Pacific Ocean (Parekh et al., 2008) can be explained by the absence of iron limitation of ocean biota in these simulations. Most of the $CO_{2,atm}$ change in these simulations is primarily driven through downstream effects on SOc export production, but it is minor because most of the dissolved iron is scavenged onto sinking particles during the transit to the SOc, which substantially lowers its bioavailability (Parekh et al., 2008; Oka et al., 2011; Tagliabue and Resing, 2016). However, ocean current transport of iron was shown to be non-negligible in other simulations (Lefèvre and Watson, 1999; Lambert et al., 2015). The significant impact of aeolian dust supply to the *entire* Pacific Ocean on $CO_{2,atm}$ levels modelled by Oka et al. (2011) shows that in these simulations large areas of the Pacific are iron-limited HNLC regions, with higher modern surface phosphate concentrations than measured. Another reason why this is not observed in other studies (Parekh et al., 2008) may be the underestimation of dust fluxes in some simulated global dust loading maps (Lambert et al., 2015), which are used to force numerical models.

Additional sources of iron to the surface ocean such as from sediments, upwelling of sub-surface waters or hydrothermal vents reduce the sensitivity of $CO_{2,atm}$ to changes in aeolian iron fertilisation (Peng and Broecker, 1991; Lefèvre and Watson, 1999;

Watson and Lefèvre, 1999; Tagliabue et al., 2014a). In models that do not resolve different iron sources, decreases in dust fluxes show a rapid increase in $CO_{2,atm}$ levels proportional to the forcing, because the global ocean biota becomes severely iron limited (Archer and Johnson, 2000; Parekh et al., 2006a, 2006b). In models that resolve non-aeolian iron sources in the ocean, the $CO_{2,atm}$ increase due to the absence of aeolian dust fluxes is marginal ($\Delta CO_{2,atm} = +2$ ppm), because marine biota utilise iron from other sources (Tagliabue et al., 2014a).

A $CO_{2,atm}$ drop as a result of increased aeolian dust fluxes to the ocean is amplified through an increase in ligand concentrations (Parekh et al., 2006b, 2008; Tagliabue et al., 2014a), which enhances the bioavailability of iron through organic complexation (Rue and Bruland, 1995; Gledhill and Buck, 2012). In simulations with a doubling and tripling of ligand concentrations in the global ocean and SOc, respectively, the observed $CO_{2,atm}$ decrease is enhanced by a factor of three (Parekh et al., 2006b, 2008). Field experiments show an increase in ligand concentrations with higher ocean iron concentrations (e.g., Rue and Bruland, 1997), providing a potential positive feedback mechanism for $CO_{2,atm}$ drawdown through aeolian dust supply. However, ligand concentrations, -types, and their modes of formation are poorly documented, and are generally not prognostically simulated (Ridgwell, 2003; Völker and Tagliabue, 2015). Along with uncertainties regarding the spatial and temporal variability of iron solubility in the ocean (Albani et al., 2016), ligands therefore remain a major uncertainty in estimating the role of aeolian dust supply on the global carbon cycle. Furthermore, lithogenic material deposits not only dust and iron in the ocean, it also acts as scavenging surface for dissolved iron in seawater (e.g., Wagener et al., 2010). Considering these two opposing roles of dust particles as iron source and sink in biogeochemical models is important, because its consideration brings simulated marine iron distributions much closer to observations (Ye and Völker, 2017). Another critical aspect are features of the ocean iron cycle that may be missing in models because their existence is unknown. Recently, an enormous plume of iron emanating from the Sea of Okhotsk into the sub-Arctic North Pacific, a major HNLC region, was discovered and was found to have a significant impact on nutrient utilisation and export production in that region (Nishioka and Obata, 2017). If global dust models do not consider all possible sources of iron to the ocean, also including glacial outwash (Sugden et al., 2009), epicontinental seas (Nishioka and Obata, 2017) or even palaeo-fires (Albani et al., 2016), then this may be another major limitation of the models' ability to simulate dust fluxes accurately and assess their biogeochemical impacts reliably.

2.5.3.4. Model-predictions of past millennial-scale $CO_{2,atm}$ changes due to aeolian dust fluxes. Assuming a two-fold global ocean increase in dust supply during the LGM (e.g., Mahowald et al., 1999; Kohfeld and Harrison, 2001; Kienast et al., 2016) and taking this as upper boundary for aeolian dust-driven changes in $CO_{2,atm}$ on millennial timescales, linear regression of the compiled simulations suggests a large range of possible magnitudes of $CO_{2,atm}$ drop varying between -8 ± 7 ppm (GCMs and ESMs; Bopp et al., 2003; Parekh et al., 2006a, 2006b; Tagliabue et al., 2009b), and -17 ± 11 ppm (box models; Lefèvre and Watson, 1999; Watson and Lefèvre, 1999), cf. Table 2. Unknown ligand concentrations/-strength and different iron sources in the ocean add significant uncertainty to these estimates (e.g., Parekh et al., 2006b, 2008; Tagliabue et al., 2014a).

As the SOc is the largest HNLC zone at present-day, aeolian supply of dust to the SOc may be crucial for dust-driven $CO_{2,atm}$ changes (e.g., Menviel et al., 2012). Direct estimates of changes in the supply of dust to the South Atlantic and South Pacific at the LGM suggest $f_{SOc} = 4$ as an appropriate upper limit (Anderson et al., 2014; Lamy et al., 2014; Martínez-García et al., 2014). Extrapolating these findings to the entire SOc in the light of sparse proxy data, Parekh et al. (2008) find that dust supply had negligible impact on $CO_{2,atm}$ ($\Delta CO_{2,atm} = \sim$-4 ppm). However, the model of Parekh et al. (2008) lacks a silicic acid cycle and is characterised by too vigorous deep Southern Ocean convection and upwelling of CO_2-rich water masses that compensates for $CO_{2,atm}$ drawdown by iron-fertilised marine biology. How realistic the model estimates of Parekh et al. (2008) are for determining the largest $CO_{2,atm}$ effect of SOc dust fluxes remains therefore an open question.

3. Summary

We have compiled 55 model studies that provide insights into millennial-scale changes in $CO_{2,atm}$ based on 778 individual simulations that focus on six different forcing mechanisms. We have analysed modelled $CO_{2,atm}$ changes of each of these simulations as a function of the structural and spatial model complexity, and prescribed forcing parameters. Although these simulations are very different and are dominated by different mechanisms, common trends of simulated $CO_{2,atm}$ change emerge (Table 2, Fig. 17). Where possible, we have quantified these trends across simulations with different model hierarchies and forcing parameters for a given type of forcing, which summarises the current numerical model perspective on the drivers of millennial-scale $CO_{2,atm}$ variations (Table 2). We also acknowledge various sources of uncertainties and unresolved issues (Table 2). Observed inter- and intra-model variations in simulated $CO_{2,atm}$ change can to some extent be explained by differences in complexity of the applied model and/or in the experimental design (Tables 1 and 2). Our review highlights that although numerical models may agree on the direction of modelled $CO_{2,atm}$ change for a prescribed forcing and a particular time during the simulation, the mechanisms underlying this $CO_{2,atm}$ change may be fundamentally different.

Climate boundary conditions influence the magnitude of simulated $CO_{2,atm}$ change in NAtl FW hosing experiments, both by determining the amount of carbon stored in the ocean interior, but also via dynamically different oceanic and land processes affecting $CO_{2,atm}$. The impact of different climate background conditions on $CO_{2,atm}$ levels in simulations forced by FW addition in the SOc, as well as changes in the position and intensity of the SHW, Antarctic sea ice or aeolian dust supply to the ocean remains insufficiently known.

Model-informed predictions of the contribution of one particular forcing to millennial-scale $CO_{2,atm}$ change is typically hampered due to a number of reasons. Firstly, realistic forcing parameters are poorly constrained (for instance in the case of SHW changes). Secondly, simulations run under interglacial boundary conditions provide an incomplete picture of past carbon cycle dynamics, because millennial-scale $CO_{2,atm}$ variability is a distinct feature of “mild”-glacial boundary conditions. And thirdly, different complexities and insufficiencies of the models often express themselves in a wide range of $CO_{2,atm}$ variations simulated for a given forcing. The effects of parameterisations, idealisations and simplifications of physical, biological or chemical processes on simulated $CO_{2,atm}$ levels are often insufficiently constrained. Nevertheless, our review emphasises that observed millennial-scale $CO_{2,atm}$ variability can only be explained by a combination of factors, consistent with previous findings (e.g., Köhler et al., 2005a; Brovkin et al., 2012).

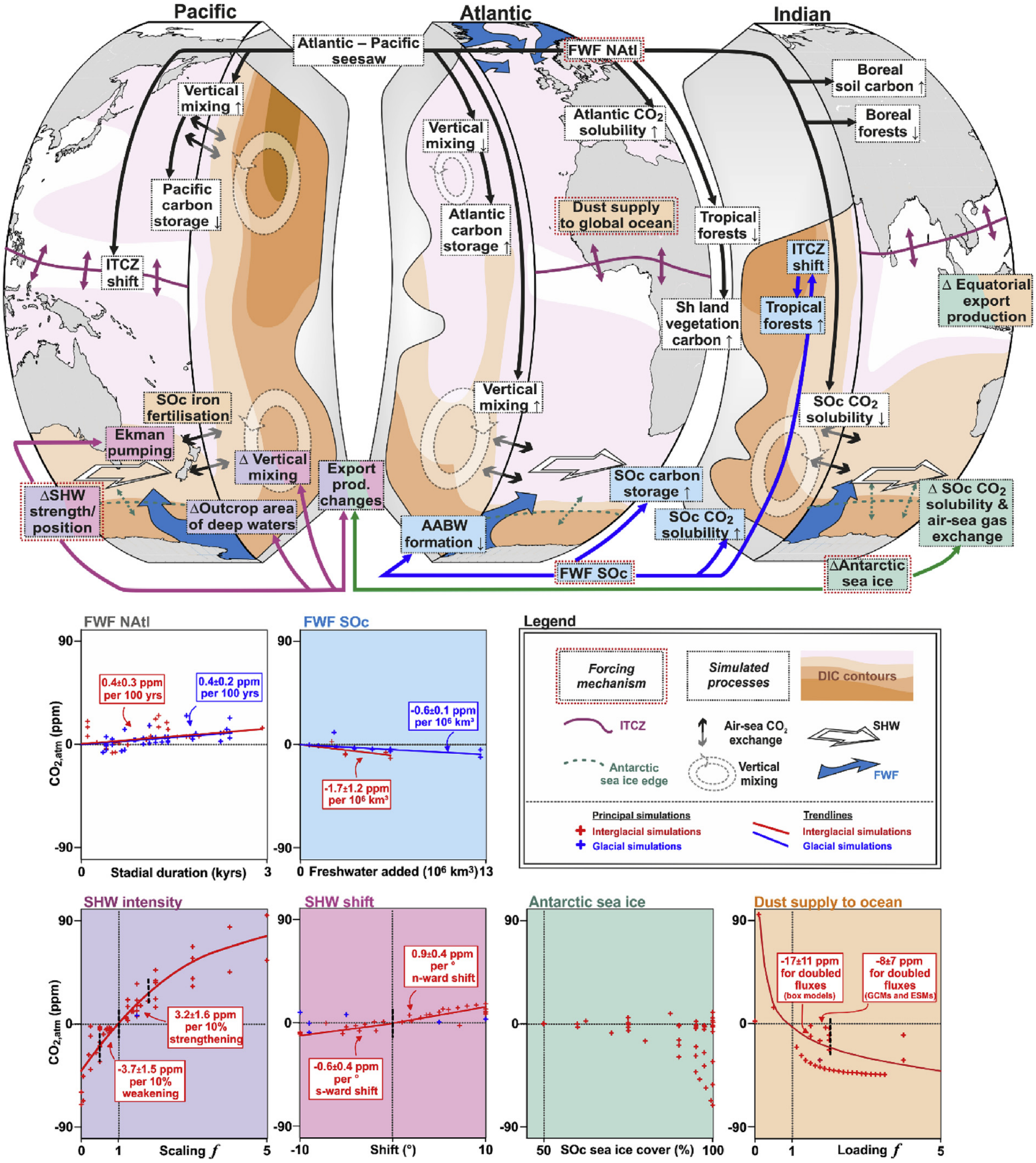

Fig. 17. Mechanisms of millennial-scale $CO_{2,atm}$ change in numerical model simulations. We highlight the characteristics of modelled $CO_{2,atm}$ change, and adjustments in land- and marine carbon inventories in simulations forced by different types of mechanisms: FW supply to the NAtl (white) and the SOc (blue), changes in the strength (purple) and position of the SHW (violet), variations in Antarctic sea ice extent (green), and changes in aeolian dust supply to the ocean (orange). Boxes below show the compiled simulated $CO_{2,atm}$ change (crosses) for a given forcing under interglacial (red) and glacial (blue) boundary conditions (principal simulations only; Tables S1–S7), as well as the trends of $CO_{2,atm}$ change per unit forcing derived from them (Table 2).

3.1. FWF in the NAtl

Numerical model simulations forced by FW hosing in the NAtl show both an increase and decrease in simulated $CO_{2,atm}$ during associated AMOC minima. The direction of $CO_{2,atm}$ change is not a function of specific parameters of the experimental design. Only in individual studies, where boundary conditions and the overall forcing setting are held constant, the amplitude of $CO_{2,atm}$ change correlates with the magnitude, duration and total amount of FW release. The modelled $CO_{2,atm}$ increase at AMOC recoveries/-overshoots is linearly correlated to the stadial duration (i.e., the duration of the AMOC perturbation). The link between the modelled $CO_{2,atm}$ change and stadial length, and its characteristic millennial timescale, implies that the cumulative release of CO_2 from the ocean- and/or land biosphere reservoirs is broadly linear over time, and that it is primarily driven by the ocean (with dampening from land processes). Indeed, the mean overturning timescale of the ocean is believed to be much slower than the timescale of dynamic changes in land vegetation. However, there is a lack of experiments testing the characteristic timescale of anomalous carbon fluxes from soils, litter, boreal- or tropical forests for various stadial lengths. The simulated $CO_{2,atm}$ change is an integral of changes in the oceanic and terrestrial carbon reservoirs, whereby the effects of the dominant driver are generally buffered by changes in the non-dominant reservoir by 50–80%. A FW-driven AMOC reduction generally leads to increased carbon storage in the Atlantic due to reduced overturning rates and increased CO_2 solubility at the sea surface, which acts as a carbon sink. However, these effects are often counteracted to variable degree by different far-field changes that are triggered by AMOC perturbations. In the SOc, these remote effects may include a lowered CO_2 solubility owing to surface ocean warming, as well as increased vertical mixing and carbon release through air-sea CO_2 equilibration. The latter is often simulated for the North Pacific Ocean, where the deep ocean becomes increasingly better ventilated (through the Atlantic-Pacific seesaw mechanism) and loses its carbon, often through anomalous air-sea CO_2 fluxes in the Pacific sector of the SOc. Through shifts in the ITCZ, tropical forests may experience large changes in their carbon inventories that interact with ocean carbon storage changes to modify $CO_{2,atm}$. Temperature effects on carbon degradation in soils and CO_2 fertilisation effects on the terrestrial biosphere additionally influence carbon stocks on land, and hence $CO_{2,atm}$ levels. A consistent dominant driver of $CO_{2,atm}$ levels does not emerge from the compiled hosing experiments.

3.2. FWF in the SOc

FW hosing experiments in the SOc with a full organic carbon cycle mostly simulate a $CO_{2,atm}$ decrease (of up to 12 ppm). The primary physical ocean response to SOc FW hosing in these simulations is a decrease in AABW formation. This reduces deep-ocean overturning, and hence increases deep-ocean carbon storage, which lowers $CO_{2,atm}$. In addition, NADW weakening in some SOc hosing experiments contributes to a greater deep-ocean carbon storage in the Atlantic. However, FWF in the SOc also leads to an increased CO_2 solubility due to surface cooling and/or an increase in terrestrial carbon storage in the tropics owing to a northward ITCZ shift and wetter conditions, which contribute to the modelled $CO_{2,atm}$ decrease.

3.3. Changes in SHW winds

Simulations forced by increases (decreases) in the SHW wind intensity mostly under interglacial climate boundary conditions consistently indicate a marked rise (drop) in $CO_{2,atm}$. This is primarily driven by changes in SOc vertical mixing (driving carbon release primarily from the mid-depth ocean, ~500–2000 m), which is buffered by parallel changes in marine export production and/or the terrestrial carbon storage. Inter-model differences in simulated $CO_{2,atm}$ of up to 40 ppm can be related to some extent to the representation of mesoscale eddies. These tend to counteract wind-driven changes in upwelling (lowering residual upwelling in the SOc), and hence diminish the effect of vertical mixing on $CO_{2,atm}$. Non-eddy resolving model setups, with coarse (eddy-permitting or eddy-parameterising) grid resolutions ($>1/10°$), and constant thickness diffusivity parameters, applied in all simulations compiled here question whether mesoscale eddies are faithfully represented, which in turn may suggest that all of the compiled simulations overestimate the effect of SHW changes on $CO_{2,atm}$.

In comparison, northward (southward) shifts of the SHW lead in most simulations to a weak positive (negative) change in $CO_{2,atm}$. Northward (southward) shifted SHW winds result in an increase (decrease) in the outcrop area of CO_2-rich sub-surface water masses and vertical mixing in the SOc, releasing (retaining) carbon primarily from (at) intermediate water depths and/or the Pacific Ocean. This dominates the simulated $CO_{2,atm}$ change, although it is partially compensated by changes in the terrestrial biosphere and increased marine export production. However, a large fraction of carbon is also redistributed within the ocean, causing little $CO_{2,atm}$ change in SHW wind-shift experiments. Feedback mechanisms among adjustments of the SHW, Antarctic sea ice cover, surface ocean buoyancy forcing, export production changes, and the rate and location of AABW formation remain insufficiently known, as they are incompletely represented in numerical models.

3.4. Antarctic sea ice

Prescribing an expansion of sea ice in the SOc leads often to a large $CO_{2,atm}$ reduction in box models, whereas EMICs and GCMs simulate a smaller decrease or even an increase in $CO_{2,atm}$. In box models, the $CO_{2,atm}$ response is primarily driven by an isolation of the deep ocean from the atmosphere by suppressing SOc air-sea CO_2 exchange. Additional compensating effects from changes in export production, deep-water formation, and ocean CO_2 solubility changes are resolved in EMICs and GCMs, and account for the lower-amplitude $CO_{2,atm}$ changes observed in these models. In addition, as Antarctic sea ice cover tends to reduce export production in the SOc, it has important downstream effects by enhancing the nutrient availability and export production in equatorial regions. To what extent the effects of these opposing (high-latitude versus equatorial) processes on $CO_{2,atm}$ compensate each other depends on whether these processes are represented in the models (which in box models comes down to the existence of an equatorial box). Future work may focus on the role of sea ice in $CO_{2,atm}$ in glacial climates, and what effects sea ice has on $CO_{2,atm}$ levels through impacts on vertical mixing and ocean diffusivities (e.g. through brine rejection), deep-water formation, the position of the SHW, and surface ocean buoyancy fluxes.

3.5. Aeolian dust supply to the ocean

Simulated $CO_{2,atm}$ consistently drops, when dust fluxes to the global ocean and SOc are increased, which is due to an alleviation of iron limitation of marine biota and an increase in marine export production. The simulations show that marine biota is also limited by additional factors, such as light and other nutrients (e.g., silicic acid). Iron supply to the SOc can also have down-stream effects on biological production in the equatorial region, and may be significant from non-aeolian sources. In simulations considering non-aeolian dust fluxes, simulated $CO_{2,atm}$ changes become increasingly insensitive to increasing or decreasing dust fluxes. There are uncertainties regarding the influence of climate boundary conditions on simulated dust-driven $CO_{2,atm}$ changes, the Fe solubility in the ocean, and the response of ligands to varying Fe availability. Sensitivity simulations show a large (small) drop in simulated $CO_{2,atm}$ levels for an increase (decrease) ligand concentrations. The influence of Fe from ocean sediments, hydrothermal vents, and from non-iron limited ocean regions on millennial-scale $CO_{2,atm}$ variability was acknowledged but remains incompletely quantified.

4. Concluding remarks

Numerical models are necessarily an imperfect representation of the Earth system. The choice of forcing functions and model-specific characteristics influence the simulated $CO_{2,atm}$ change and can introduce biases that can be very difficult to quantify. This applies to all simulations compiled here to various degrees (Table 2). On the other hand, models are the only tools to test the impact and physical feasibility of various processes and scenarios within the Earth system. However, they can never be a true reflection of the “real world” due to the heuristic model nature (Oreskes et al., 1994). Although all models are inevitably “imperfect” with respect to their representation of real-world processes, it is often their relative simplicity that makes them scrutable and therefore useful.

Numerical model outcomes are almost always underdetermined (i.e., having too few constraints to justify the robustness of a single simulation), because (ground-truthing) (proxy-) data are generally challenging to obtain and always come with some irreducible level of uncertainty in age and/or meaning. Model results must therefore be considered a “non-unique solution”, and can be right, i.e., consistent with sparse observations, for the wrong reasons (Oreskes et al., 1994). Unravelling the mechanisms driving $CO_{2,atm}$ changes on millennial timescales in coupled carbon cycle-climate models remains therefore a challenge, not least because of the possibility that the $CO_{2,atm}$ changes have been generated by a number of different contributing mechanisms that are difficult to unambiguously identify and/or quantify using a limited array of proxy-data and idealised model simulations. This particularly applies to assessing the role of inter-hemispheric climate variability in millennial-scale $CO_{2,atm}$ change (Fig. 2; e.g., Anderson and Carr, 2010), as well as the role of small-scale processes, because current coupled carbon cycle-climate models capable of long simulations required for the study of millennial-scale climate variability (such as EMICs) are characterised by incomplete and/or often simplified atmospheric, oceanic, and/or cryospheric model components. The potential sensitivity of $CO_{2,atm}$ to various forcing mechanisms under these restrictions needs to be understood further, for instance through global and regional Earth system model simulations with higher spatial resolution, in which small-scale processes such as deep convection, polynyas, seasonal sea ice growth/melt cycles of sea ice, and mesoscale eddy activity, can possibly be implemented.

In addition, we have identified a number of important gaps in carbon cycling modelling based on our compilation. We have pointed out that simulations with interglacial boundary conditions may be imperfect; however, these simulations shed light on the model's general sensitivity to perturbations, and often show similar processes as under glacial boundary conditions (despite differences in the magnitude of their impact). The design and performance of simulations within inter-model comparison projects that test the individual and combined influence of different forcing parameters on $CO_{2,atm}$ levels may prove particularly useful in advancing our understanding of natural $CO_{2,atm}$ variability. However, such model intercomparison projects must ultimately proceed in step with advancements in the fields of palaeoceanography and oceanography: firstly, high-resolution proxy-data reconstructions are needed to put tight constraints on past environmental changes accompanying $CO_{2,atm}$ variations, and inform models on realistic forcing parameters and climate background conditions; secondly, processes relevant for the cycling of carbon in the Earth system (e.g., role of mesoscale eddies, iron solubility in the ocean, etc.) need to be better understood from an observational standpoint. And thirdly, these processes need to be considered in Earth system models (although this comes at some computational cost), or constraints on the bias introduced through their omission or simplified representation are needed. One way of meeting these challenges may lie in an interactive and iterative process of bringing (proxy-) data and model outputs together (e.g., through data assimilation and community efforts). This may involve the identification of key observable requirements of certain hypotheses in numerical model simulations, and an assessment whether they can be refuted by existing and/or new proxy observations. On the other hand, available and evolving palaeo-data reconstructions should be used to inform and constantly challenge the validity of experimental designs and numerical model outputs.

Acknowledgements

J.G. acknowledges support from Deutsche Forschungsgemeinschaft (grant GO 2294/2-1). We are grateful for support from the Swiss National Science Foundation (J.G. and S.L.J.: grant 200021_16300; G.B., F.J., and A.J.-T.: grant 200020_172476; T.L.F.: PP00P2_170687; and S.L.J.: grants PP00P2-144811 and PP002_172915). P.K.'s coauthorship is a contribution to the German Paleomodeling Research Project PALMOD, funded by the German Federal Ministry of Education and Research (BMBF). K.J.M. and L.M. are funded by the Australian Research Council (DP180100048, DP180102357 and DE150100107). A.S. acknowledges support from the US National Science Foundation’s Marine Geology and Geophysics Program (grant 1634719). L.C.S. acknowledges the Royal Society, the Cambridge Isaac Newton Trust and NERC grant NE/J010545/1. We sincerely thank Willem Huiskamp, Nathaelle Bouttes, Axel Timmermann, Bob Anderson, Gisela Winckler, Katsumi Matsumoto, Ayako Abe-Ouchi and Jonathan Lauderdale for helpful discussions. This study benefited from discussions with attendees of meetings of the INQUA “IPODS” (Investigating Past Ocean Dynamics) and the PAGES (Past Global Changes) Ocean Circulation and Carbon Cycling (OC3) focus groups. We thank Timothy J. Horscroft and Henning A. Bauch for support throughout the writing of this contribution, two anonymous reviewers for constructive feedback on the manuscript, and Antje H. L. Voelker for efficient editorial handling. Data presented in this study are available in the supplementary material.

Appendix A. Supplementary data

Supplementary data to this article can be found online at https://doi.org/10.1016/j.quascirev.2019.05.013.

References

Abelmann, A., Gersonde, R., Knorr, G., Zhang, X., Chapligin, B., Maier, E., Esper, O., Friedrichsen, H., Lohmann, G., Meyer, H., Tiedemann, R., 2015. The seasonal sea-ice zone in the glacial Southern Ocean as a carbon sink. Nat. Commun. 6, 8136. https://doi.org/10.1038/ncomms9136.

Abernathey, R., Marshall, J., Ferreira, D., 2011. The dependence of Southern Ocean meridional overturning on wind stress. J. Phys. Oceanogr. 41 (12), 2261–2278. https://doi.org/10.1175/JPO-D-11-023.1.

Abernathey, R.P., Cerovecki, I., Holland, P.R., Newsom, E., Mazloff, M., Talley, L.D., 2016. Water-mass transformation by sea ice in the upper branch of the Southern Ocean overturning. Nat. Geosci. 9 (8), 596–601. https://doi.org/10.1038/ngeo2749.

Ahn, J., Brook, E.J., 2008. Atmospheric CO_2 and climate on millennial time scales during the last glacial period. Science 322 (5898), 83–85. https://doi.org/10.1126/science.1160832.

Albani, S., Mahowald, N.M., Murphy, L.N., Raiswell, R., Moore, J.K., Anderson, R.F., McGee, D., Bradtmiller, L.I., Delmonte, B., Hesse, P.P., Mayewski, P.A., 2016. Paleodust variability since the Last Glacial Maximum and implications for iron inputs to the ocean. Geophys. Res. Lett. 43 (8), 3944–3954. https://doi.org/10.1002/2016GL067911.

Alvarez-Solas, J., Charbit, S., Ritz, C., Paillard, D., Ramstein, G., Dumas, C., 2010. Links between ocean temperature and iceberg discharge during Heinrich events. Nat. Geosci. 3 (2), 122–126. https://doi.org/10.1038/ngeo752.

Anderson, R.F., Ali, S., Bradtmiller, L.I., Nielsen, S.H.H., Fleisher, M.Q., Anderson, B.E., Burckle, L.H., 2009. Wind-driven upwelling in the Southern Ocean and the deglacial rise in atmospheric CO_2. Science 323 (5920), 1443–1448. https://doi.org/10.1126/science.1167441.

Anderson, R.F., Barker, S., Fleisher, M., Gersonde, R., Goldstein, S.J., Kuhn, G., Mortyn, P.G., Pahnke, K., Sachs, J.P., 2014. Biological response to millennial variability of dust supply in the Subantarctic South Atlantic Ocean. Philos. Trans. R. Soc. 372, 20130054. https://doi.org/10.1098/rsta.2013.0054.

Anderson, R.F., Carr, M.-E., 2010. Uncorking the Southern Ocean's vintage CO_2. Science 328 (5982), 1117–1118. https://doi.org/10.1126/science.1190765.

Archer, D., Maier-Reimer, E., 1994. Effect of deep-sea sedimentary calcite preservation on atmospheric CO_2 concentration. Nature 367, 260–263. https://doi.

org/10.1038/367260a0.

Archer, D.E., Johnson, K., 2000. A model of the iron cycle in the ocean. Glob. Biogeochem. Cycles 14 (1), 269–279. https://doi.org/10.1029/1999GB900053.

Archer, D.E., Martin, P.A., Milovich, J., Brovkin, V., Plattner, G.-K., Ashendel, C., 2003. Model sensitivity in the effect of Antarctic sea ice and stratification on atmospheric pCO_2. Paleoceanography 18 (1), 1012. https://doi.org/10.1029/2002PA000760.

Armand, L., Ferry, A., Leventer, A., 2017. In: Thomas, D.N. (Ed.), Advances in Palaeo Sea Ice Estimation. Sea Ice. John Wiley & Sons, Ltd., Chichester, UK & Hoboken, USA, pp. 600–629. https://doi.org/10.1002/9781118778371.ch26.

Bacastow, B., 1996. The effect of temperature change of the warm surface waters of the oceans on atmospheric CO_2. Glob. Biogeochem. Cycles 10 (2), 319–333. https://doi.org/10.1029/96GB00039.

Bacastow, R., Maier-Reimer, E., 1990. Ocean-circulation model of the carbon cycle. Clim. Dyn. 4 (2), 95–125. https://doi.org/10.1007/BF00208905.

Bereiter, B., Eggleston, S., Schmitt, J., Nehrbass-Ahles, C., Stocker, T.F., Fischer, H., Kipfstuhl, S., Chappellaz, J., 2015. Revision of the EPICA Dome C CO_2 record from 800 to 600 kyr before present. Geophys. Res. Lett. 42 (2), 542–549. https://doi.org/10.1002/2014GL061957.

Bereiter, B., Lüthi, D., Siegrist, M., Schüpbach, S., Stocker, T.F., Fischer, H., 2012. Mode change of millennial CO_2 variability during the last glacial cycle associated with a bipolar marine carbon seesaw. Proc. Natl. Acad. Sci. 109 (25), 9755–9760. https://doi.org/110.1073/pnas.1204069109.

Berger, W.H., Keir, R.S., 1984. Glacial-Holocene changes in atmospheric CO_2 and the deep-sea record. In: Hansen, J.E., Takahashi, T. (Eds.), Geophysical Monograph Series 29: Climate Processes and Climate Sensitivity. American Geophysical Union, Washington, DC, USA, pp. 337–351. https://doi.org/10.1029/GM029p0337.

Bianchi, C., Gersonde, R., 2004. Climate evolution at the last deglaciation: the role of the Southern Ocean. Earth Planet. Sci. Lett. 228 (3), 407–424. https://doi.org/10.1016/j.epsl.2004.10.003.

Blain, S., Quéguiner, B., Armand, L., Belviso, S., Bombled, B., Bopp, L., Christaki, U., Corbie, A., Bowie, A., Brunet, C., Brussaard, C., Durand, I., Ebersbach, F., Fuda, J., Garcia, N., Gerringa, L., Griffiths, B., Malits, A., Mosseri, J., Obernosterer, I., Lefe, D., Savoye, N., Scouarnec, L., Souhaut, M., Thuiller, D., Timmermans, K., Viollier, E., Vong, L., Wagener, T., 2007. Effect of natural iron fertilization on carbon sequestration in the Southern Ocean. Nature 446, 1070–1075. https://doi.org/10.1038/nature05700.

Böhm, E., Lippold, J., Gutjahr, M., Frank, M., Blaser, P., Antz, B., Fohlmeister, J., Frank, N., Andersen, M.B., Deininger, M., 2015. Strong and deep Atlantic meridional overturning circulation during the last glacial cycle. Nature 517, 73–76. https://doi.org/10.1038/nature14059.

Bond, G.C., Broecker, W.S., Johnsen, S.J., McManus, J.F., Jouzel, J., Bonani, G., 1993. Correlations between climate records from North Atlantic sediments and Greenland ice. Nature 366, 529–531. https://doi.org/10.1038/365143a0.

Bond, G.C., Heinrich, H., Broecker, W., Labeyrie, L., McManus, J., Andrews, J., Huon, S., Jantschik, R., Clasen, S., Simet, C., Tedesco, K., Klas, M., Bonani, G., Ivy, S., 1992a. Evidence for massive discharges of icebergs into the North Atlantic ocean during the last glacial period. Nature 358, 325–327. https://doi.org/10.1038/360245a0.

Bond, G.C., Lotti, R., 1995. Iceberg discharges into the North Atlantic on millennial time scales during the last glaciation. Science 267 (5200), 1005–1010. https://doi.org/10.1126/science.267.5200.1005.

Bond, G.C., Showers, W., Elliot, M., Evans, M., Lotti, R., Hajdasn, I., 1992b. The North Atlantic's 1-2 kyr climate rhythm: relation to Heinrich events, Dansgaard/Oeschger cycles and the Little Ice Age. In: Geophysical Monograph Series 112: Mechanisms of Global Climate Change at Millennial Time Scales. American Geophysical Union, Washington, DC, USA, pp. 35–58. https://doi.org/10.1029/GM112p0035.

Bopp, L., Kohfeld, K.E., Le Quéré, C., Aumont, O., 2003. Dust impact on marine biota and atmospheric CO_2 during glacial periods. Paleoceanography 18 (2). https://doi.org/10.1029/2002PA000810.

Bouttes, N., Paillard, D., Roche, D.M., 2010. Impact of brine-induced stratification on the glacial carbon cycle. Clim. Past 6, 575–589. https://doi.org/10.5194/cp-6-575-2010.

Bouttes, N., Paillard, D., Roche, D.M., Brovkin, V., Bopp, L., 2011. Last glacial maximum CO_2 and $\delta^{13}C$ successfully reconciled. Geophys. Res. Lett. 38 (2), L02705. https://doi.org/10.1029/2010GL044499.

Bouttes, N., Roche, D.M., Paillard, D., 2012. Systematic study of the impact of fresh water fluxes on the glacial carbon cycle. Clim. Past 8 (2), 589–607. https://doi.org/10.5194/cp-8-589-2012.

Boyd, P.W., Jickells, T.D., Law, C.S., Blain, S., Boyle, E., Buesseler, K.O., Coale, K.H., Cullen, J.J., de Baar, H.J.W., Follows, M., Harvey, M., Lancelot, C., Levasseur, M., Owens, N.P.J., Pollard, R., Rivkin, R.B., Sarmiento, J.L., Schoemann, V., Smetacek, V., Takeda, S., Tsuda, A., Turner, S., Watson, A.J., 2007. Mesoscale iron enrichment experiments 1993-2005: synthesis and future directions. Science 315 (5812), 612–617. https://doi.org/10.1126/science.1131669.

Boyle, E.A., 1988. The role of vertical chemical fractionation in controlling late Quaternary atmospheric carbon dioxide. J. Geophys. Res. 93 (C12), 15701–15714. https://doi.org/10.1029/JC093iC12p15701.

Bozbiyik, A., Steinacher, M., Joos, F., Stocker, T.F., Menviel, L., 2011. Fingerprints of changes in the terrestrial carbon cycle in response to large reorganizations in ocean circulation. Clim. Past 7 (1), 319–338. https://doi.org/10.5194/cp-7-319-2011.

Broecker, W.S., 1994. Massive iceberg discharges as triggers for global climate change. Nature 372 (6505), 421–424. https://doi.org/10.1038/372421a0.

Broecker, W.S., 1997. Thermohaline circulation, the Achilles heel of our climate system: will man-made CO_2 upset the current balance? Science 278 (5343), 1582–1588. https://doi.org/10.1126/science.278.5343.1582.

Broecker, W.S., Peng, T.-H., 1986. Glacial to interglacial changes in the operation of the global carbon cycle. Radiocarbon 28 (2), 309–327. https://doi.org/10.1017/S0033822200007414.

Broecker, W.S., Peng, T.H., 1987. The role of $CaCO_3$ compensation in the glacial to interglacial atmospheric CO_2 change. Glob. Biogeochem. Cycles 1 (1), 15–29. https://doi.org/10.1029/GB001i001p00015.

Broecker, W.S., Peteet, D.M., Rind, D., 1985. Does the ocean-atmosphere system have more than one stable mode of operation? Nature 315 (6014), 21–26. https://doi.org/10.1038/315021a0.

Brovkin, V., Ganopolski, A., Archer, D., Munhoven, G., 2012. Glacial CO_2 cycle as a succession of key physical and biogeochemical processes. Clim. Past 8 (1), 251–264. https://doi.org/10.5194/cp-8-251-2012.

Bryan, F., 1986. High-latitude salinity effects and interhemispheric thermohaline circulations. Nature 323 (6086), 301–304. https://doi.org/10.1038/323301a0.

Bryan, K., 1969. Climate and the ocean circulation. 3. The ocean model. Mon. Weather Rev. 97 (1), 806–827. https://doi.org/10.1175/1520-0493(1969)097<0806:CATOC>2.3.CO;2.

Bryan, K., Cox, M., 1967. A numerical investigation of the oceanic general circulation. Tellus 19 (1), 54–80. https://doi.org/10.1111/j.2153-3490.1967.tb01459.x.

Brzezinski, M.A., Pride, C.J., Franck, V.M., Sigman, D.M., Sarmiento, J.L., Matsumoto, K., Gruber, N., Rau, G.H., Coale, K.H., 2002. A switch from $Si(OH)_4$ to NO_3^- depletion in the glacial Southern Ocean. Geophys. Res. Lett. 29 (12), 1564. https://doi.org/10.1029/2001GL014349.

Buchanan, P.J., Matear, R.J., Lenton, A., Phipps, S.J., Chase, Z., Etheridge, D.M., 2016. The simulated climate of the Last Glacial Maximum and insights into the global marine carbon cycle. Clim. Past 12 (12), 2271–2295. https://doi.org/10.5194/cp-12-2271-2016.

Buizert, C., Sigl, M., Severi, M., Markle, B.R., Wettstein, J.J., McConnell, J.R., Pedro, J.B., Sodemann, H., Goto-Azuma, K., Kawamura, K., Fujita, S., Motoyama, H., Hirabayashi, M., Uemura, R., Stenni, B., Parrenin, F., He, F., Fudge, T.J., Steig, E.J., 2018. Abrupt ice-age shifts in southern westerly winds and Antarctic climate forced from the north. Nature 563 (7733), 681–685. https://doi.org/10.1038/s41586-018-0727-5.

Cacho, I., Grimalt, J.O., Pelejero, C., Canals, M., Sierro, F.J., Flores, J.A., Shackleton, N., 1999. Dansgaard-Oeschger and Heinrich event imprints in Alboran sea paleotemperatures. Paleoceanography 14 (6), 698–705. https://doi.org/10.1029/1999PA900044.

Cassar, N., Bender, M.L., Barnett, B.A., Fan, S., Moxim, W.J., Levy, H., Tilbrook, B., 2007. The Southern Ocean biological response to aeolian iron deposition. Science 317 (5841), 1067–1070. https://doi.org/10.1126/science.1144602.

Charles, C.D., Lynch-Stieglitz, J., Ninnemann, U.S., Fairbanks, R.G., 1996. Climate connections between the hemisphere revealed by deep sea sediment core/ice core correlations. Earth Planet. Sci. Lett. 142 (1), 19–27. https://doi.org/10.1016/0012-821X(96)00083-0.

Chavaillaz, Y., Codron, F., Kageyama, M., 2013. Southern westerlies in LGM and future (RCP4.5) climates. Clim. Past 9 (2), 517–524. https://doi.org/10.5194/cp-9-517-2013.

Chiang, J.C.H., Bitz, C.M., 2005. Influence of high latitude ice cover on the marine Intertropical Convergence Zone. Clim. Dyn. 25 (5), 477–496. https://doi.org/10.1007/s00382-005-0040-5.

Chikamoto, M.O., Abe-Ouchi, A., Oka, A., Ohgaito, R., Timmermann, A., 2012a. Quantifying the ocean's role in glacial CO_2 reductions. Clim. Past 8 (2), 545–563. https://doi.org/10.5194/cp-8-545-2012.

Chikamoto, M.O., Menviel, L., Abe-Ouchi, A., Ohgaito, R., Timmermann, A., Okazaki, Y., Harada, N., Oka, A., Mouchet, A., 2012b. Variability in North Pacific intermediate and deep water ventilation during Heinrich events in two coupled climate models. Deep. Res. Part II Top. Stud. Oceanogr. 61–64, 114–126. https://doi.org/10.1016/j.dsr2.2011.12.002.

Clark, P.U., Alley, R.B., Keigwin, L.D., Licciardi, J.M., Johnsen, S.J., Wang, H., 1996. Origin of the first global meltwater pulse following the last glacial maximum. Paleoceanography 11 (5), 563–577. https://doi.org/10.1029/96PA01419.

Clark, P.U., Mitrovica, J.X., Milne, G.A., Tamisiea, M.E., 2002. Sea-level fingerprint as a direct test for the source of global meltwater pulse 1A. Science 295, 2438–2441. https://doi.org/10.1126/science.1068797.

Claussen, M., Mysak, L., Weaver, A., Crucifix, M., Fichefet, T., Loutre, M.F., Weber, S., Alcamo, J., Alexeev, V., Berger, A., Calov, R., Ganopolski, A., Goosse, H., Lohmann, G., Lunkeit, F., Mokhov, I., Petoukhov, V., Stone, P., Wang, Z., 2002. Earth system models of intermediate complexity: closing the gap in the spectrum of climate system models. Clim. Dyn. 18 (7), 579–586. https://doi.org/10.1007/s00382-001-0200-1.

Clement, A.C., Peterson, L.C., 2008. Mechanisms of abrupt climate change of the last glacial period. Rev. Geophys. 46 (RG4002), 1–39. https://doi.org/10.1029/2006RG000204.

CLIMAP project members, 1981. Maps of Northern and Southern Hemisphere Continental Ice, Sea Ice, and Sea Surface Temperatures in August for the Modern and the Last Glacial Maximum. Geological Society of America Map and Chart Series MC-36, Boulder, CO, USA.

Collins, L.G., Pike, J., Allen, C.S., Hodgson, D.A., 2012. High-resolution reconstruction of southwest Atlantic sea-ice and its role in the carbon cycle during marine isotope stages 3 and 2. Paleoceanography 27 (3), PA3217. https://doi.org/10.1029/2011PA002264.

Cox, P.M., Betts, R. a, Jones, C.D., Spall, S. a, Totterdell, I.J., 2000. Acceleration of global warming due to carbon-cycle feedbacks in a coupled climate model. Nature 408, 184–187. https://doi.org/10.1038/35041539.

Crosta, X., Pichon, J.J., Burckle, L.H., 1998. Reappraisal of Antarctic seasonal sea-ice at the last glacial maximum. Geophys. Res. Lett. 25 (14), 2703–2706. https://doi.org/10.1029/98GL02012.

Crowley, T.J., 1992. North Atlantic deep water cools the southern hemisphere. Paleoceanography 7 (4), 489–497. https://doi.org/10.1029/92PA01058.

d'Orgeville, M., Sijp, W.P., England, M.H., Meissner, K.J., 2010. On the control of glacial-interglacial atmospheric CO_2 variations by the Southern Hemisphere westerlies. Geophys. Res. Lett. 37 (21), 1–5. https://doi.org/10.1029/2010GL045261.

Dansgaard, W., Clausen, H.B., Gundestrup, N., Hammer, C.U., Johnsen, S.J., Kristinsdottir, P.M., Reeh, N., 1982. A new Greenland deep ice core. Science 218 (4579), 1273–1277. https://doi.org/10.1126/science.177.4047.410.

Dansgaard, W., Johnsen, S.J., Clausen, H.B., Dahl-Jensen, D., Gundestrup, N., Hammer, C.U., Oeschger, H., 1984. North Atlantic climatic oscillations revealed by deep Greenland ice cores. In: Hansen, J., Takahashi, T. (Eds.), Geophysical Monograph Series 29: Climate Processes and Climate Sensitivity. American Geophysical Union, Washington, DC, USA, pp. 288–298. https://doi.org/10.1029/GM029p0288.

de Baar, H.J.W., de Jong, J., Bakker, D.C.E., Löscher, B.M., Veth, C., Bathmann, U., Smetacek, V., 1995. Importance of iron for plankton blooms and carbon dioxide drawdown in the Southern Ocean. Nature 373, 412–415. https://doi.org/10.1038/373412a0.

De Deckker, P., Moros, M., Perner, K., Jansen, E., 2012. Influence of the tropics and southern westerlies on glacial interhemispheric asymmetry. Nat. Geosci. 5 (4), 266–269. https://doi.org/10.1038/ngeo1431.

Delmas, R.J., Ascencio, J.-M., Legrand, M., 1980. Polar ice evidence that atmospheric CO_2 20,000 yr BP was 50% of present. Nature 284, 155–157. https://doi.org/10.1038/284155a0.

Denton, G.H., Anderson, R.F., Toggweiler, J.R., Edwards, R.L., Schaefer, J.M., Putnam, A.E., 2010. The last glacial termination. Science 328 (5986), 1652–1656. https://doi.org/10.1126/science.1184119.

Deschamps, P., Durand, N., Bard, E., Hamelin, B., Camoin, G., Thomas, A.L., Henderson, G.M., Okuno, J., Yokoyama, Y., 2012. Ice-sheet collapse and sea-level rise at the Bølling warming 14,600 years ago. Nature 483 (7391), 559–564. https://doi.org/10.1038/nature10902.

Diz, P., Barker, S., 2015. Linkages between rapid climate variability and deep-sea benthic foraminifera in the deep Subantarctic South Atlantic during the last 95 kyr. Paleoceanography 30, 601–611. https://doi.org/10.1002/2015PA002784.

Dokken, T.M., Nisancioglu, K.H., Li, C., Battisti, D.S., Kissel, C., 2013. Dansgaard-Oeschger cycles: interactions between ocean and sea ice intrinsic to the Nordic seas. Paleoceanography 28, 491–502. https://doi.org/10.1002/palo.20042.

Eby, M., Weaver, A.J., Alexander, K., Zickfeld, K., Abe-Ouchi, A., Cimatoribus, A.A., Crespin, E., Drijfhout, S.S., Edwards, N.R., Eliseev, A.V., Feulner, G., Fichefet, T., Forest, C.E., Goosse, H., Holden, P.B., Joos, F., Kawamiya, M., Kicklighter, D., Kienert, H., Matsumoto, K., Mokhov, I.I., Monier, E., Olsen, S.M., Pedersen, J.O.P., Perrette, M., Philippon-Berthier, G., Ridgwell, A., Schlosser, A., Von Deimling, T.S., Shaffer, G., Smith, R.S., Spahni, R., Sokolov, A.P., Steinacher, M., Tachiiri, K., Tokos, K., Yoshimori, M., Zeng, N., Zhao, F., 2013. Historical and idealized climate model experiments: an intercomparison of Earth system models of intermediate complexity. Clim. Past 9 (3), 1111–1140. https://doi.org/10.5194/cp-9-1111-2013.

Elliot, M., Labeyrie, L., Duplessy, J.-C., 2002. Changes in North Atlantic deep-water formation associated with the Dansgaard-Oeschger temperature oscillations (60-10 ka). Quat. Sci. Rev. 21 (10), 1153–1165. https://doi.org/10.1016/S0277-3791(01)00137-8.

EPICA Community Members, 2006. One-to-one coupling of glacial climate variability in Greenland and Antarctica. Nature 444 (7116), 195–198. https://doi.org/10.1038/nature05301.

Eriksson, E., Welander, P., 1956. On a mathematical model of the carbon cycle in nature. Tellus 8 (2), 155–175. https://doi.org/10.1111/j.2153-3490.1956.tb01207.x.

Ewen, T.L., Weaver, A.J., Schmittner, A., 2004. Modelling carbon cycle feedbacks during abrupt climate change. Quat. Sci. Rev. 23, 431–448. https://doi.org/10.1016/j.quascirev.2003.08.007.

Falkowski, P.G., 1997. Evolution of the nitrogen cycle and its influence on the biological sequestration of CO_2 in the ocean. Nature 387 (6630), 272–275. https://doi.org/10.1038/387272a0.

Farneti, R., Delworth, T.L., 2010. The role of mesoscale eddies in the remote oceanic response to altered southern hemisphere winds. J. Phys. Oceanogr. 40 (10), 2348–2354. https://doi.org/10.1175/2010JPO4480.1.

Ferreira, D., Marshall, J., Ito, T., Mcgee, D., 2018. Linking glacial-interglacial states to multiple equilibria of climate. Geophys. Res. Lett. 45, 9160–9170. https://doi.org/10.1029/2018GL077019.

Ferry, A.J., Crosta, X., Quilty, P.G., Fink, D., Howard, W., Armand, L.K., 2015. First record of winter sea ice concentration in the southwest Pacific sector of the Southern Ocean. Paleoceanography 30, 1525–1539. https://doi.org/10.1002/2014PA002764.

Fischer, H., Fundel, F., Ruth, U., Twarloh, B., Wegner, A., Udisti, R., Becagli, S., Castellano, E., Morganti, A., Severi, M., Wolff, E., Littot, G., Röthlisberger, R., Mulvaney, R., Hutterli, M.A., Kaufmann, P., Federer, U., Lambert, F., Bigler, M., Hansson, M., Jonsell, U., de Angelis, M., Boutron, C., Siggaard-Andersen, M.-L., Steffensen, J.P., Barbante, C., Gaspari, V., Gabrielli, P., Wagenbach, D., 2007a. Reconstruction of millennial changes in dust emission, transport and regional sea ice coverage using the deep EPICA ice cores from the Atlantic and Indian Ocean sector of Antarctica. Earth Planet. Sci. Lett. 260 (1), 340–354. https://doi.org/10.1016/j.epsl.2007.06.014.

Fischer, H., Siggaard-Andersen, M.-L., Ruth, U., Röthlisberger, R., Wolff, E.W., 2007b. Glacial/interglacial changes in mineral dust and sea-salt records in polar ice cores: sources, transport, and deposition. Rev. Geophys. 45, RG1002. https://doi.org/10.1029/2005RG000192.

Fischer, H., Wahlen, M., Smith, J., Mastroianni, D., Deck, B., 1999. Ice core records of atmospheric CO_2 around the last three glacial terminations. Science 283 (5408), 1712–1714. https://doi.org/10.1126/science.283.5408.1712.

Fogwill, C.J., Turney, C.S.M., Golledge, N.R., Etheridge, D.M., Rubino, M., Thornton, D.P., Baker, A., Woodward, J., Winter, K., van Ommen, T.D., Moy, A.D., Curran, M.A.J., Davies, S.M., Weber, M.E., Bird, M.I., Munksgaard, N.C., Menviel, L., Rootes, C.M., Ellis, B., Millman, H., Vohra, J., Rivera, A., Cooper, A., 2017. Antarctic ice sheet discharge driven by atmosphere-ocean feedbacks at the Last Glacial Termination. Sci. Rep. 7 (39979), 1–10. https://doi.org/10.1038/srep39979.

Foley, J.A., Levis, S., Prentice, I.C., Pollard, D., Thompson, S.L., 1998. Coupling dynamic models of climate and vegetation. Glob. Chang. Biol. 4 (5), 561–579. https://doi.org/10.1046/j.1365-2486.1998.t01-1-00168.x.

Ganopolski, A., Brovkin, V., 2017. Simulation of climate, ice sheets and CO_2 evolution during the last four glacial cycles with an Earth system model of intermediate complexity. Clim. Past 13, 1695–1716. https://doi.org/10.5194/cp-13-1695-2017.

Ganopolski, A., Rahmstorf, S., 2001. Rapid changes of glacial climate simulated in a coupled climate model. Nature 409, 153–158. https://doi.org/10.1038/35051500.

Gent, P.R., 2016. Effects of southern hemisphere wind changes on the meridional overturning circulation in ocean models. Ann. Rev. Mar. Sci. 8 (1), 79–94. https://doi.org/10.1146/annurev-marine-122414-033929.

Gent, P.R., 2018. A commentary on the Atlantic meridional overturning circulation stability in climate models. Ocean Model. 122, 57–66. https://doi.org/10.1016/j.ocemod.2017.12.006.

Gent, P.R., Danabasoglu, G., 2011. Response to increasing southern hemisphere winds in CCSM4. J. Clim. 24 (19), 4992–4998. https://doi.org/10.1175/JCLI-D-10-05011.1.

Gent, P.R., McWilliams, J.C., 1990. Isopycnal Mixing in Ocean Circulation Models. J. Phys. Oceanogr. 20 (1), 150–155. https://doi.org/10.1175/1520-0485(1990)020<0150:IMIOCM>2.0.CO;2.

Gersonde, R., Zielinski, U., 2000. The reconstruction of late Quaternary Antarctic sea-ice distribution - the use of diatoms as a proxy for sea-ice. Palaeogeogr. Palaeoclimatol. Palaeoecol. 162 (3–4), 263–286. https://doi.org/10.1016/S0031-0182(00)00131-0.

Gildor, H., Tziperman, E., 2001. Physical mechanisms behind biogeochemical glacial-interglacial CO_2 variations. Geophys. Res. Lett. 28 (12), 2421–2424. https://doi.org/10.1029/2000GL012571.

Gildor, H., Tziperman, E., Toggweiler, J.R., 2002. Sea ice switch mechanism and glacial-interglacial CO_2 variations. Glob. Biogeochem. Cycles 16 (3), 1032. https://doi.org/10.1029/2001GB001446.

Gledhill, M., Buck, K.N., 2012. The organic complexation of iron in the marine environment: a review. Front. Microbiol. 3 (FEB), 1–17. https://doi.org/10.3389/fmicb.2012.00069.

Golledge, N.R., Menviel, L., Carter, L., Fogwill, C.J., England, M.H., Cortese, G., Levy, R.H., 2014. Antarctic contribution to meltwater pulse 1A from reduced Southern Ocean overturning. Nat. Commun. 5, 1–10. https://doi.org/10.1038/ncomms6107.

Gong, X., Knorr, G., Lohmann, G., Zhang, X., 2013. Dependence of abrupt atlantic meridional ocean circulation changes on climate background states. Geophys. Res. Lett. 40 (14), 3698–3704. https://doi.org/10.1002/grl.50701.

Goosse, H., Roche, D.M., Mairesse, A., Berger, M., 2013. Modelling past sea ice changes. Quat. Sci. Rev. 79, 191–206. https://doi.org/10.1016/j.quascirev.2013.03.011.

Gottschalk, J., Skinner, L.C., Lippold, J., Vogel, H., Frank, N., Jaccard, S.L., Waelbroeck, C., 2016. Biological and physical controls in the Southern Ocean on past millennial-scale atmospheric CO_2 changes. Nat. Commun. 7 (11539), 1–11. https://doi.org/10.1038/ncomms11539.

Gottschalk, J., Skinner, L.C., Misra, S., Waelbroeck, C., Menviel, L., Timmermann, A., 2015. Abrupt changes in the southern extent of North Atlantic Deep Water during Dansgaard-Oeschger events. Nat. Geosci. 8, 950–955. https://doi.org/10.1038/ngeo2558.

Grousset, F.E., Pujol, C., Labeyrie, L.D., Auffret, G., Boelaert, A., 2000. Were the North Atlantic Heinrich events triggered by the behaviour of the European ice-sheets? Geology 28 (2), 123–126. https://doi.org/10.1130/0091-7613(2000)28<123:WTNAHE>2.0.CO;2.

Hallberg, R., Gnanadesikan, A., 2006. The role of eddies in determining the structure and response of the wind-driven southern hemisphere overturning: results from the modeling eddies in the Southern Ocean (MESO) project. J. Phys. Oceanogr. 36 (12), 2232–2252. https://doi.org/10.1175/JPO2980.1.

Hansen, J., Russell, G., Rind, D., Stone, P., Lacis, A., Lebedeff, S., Ruedy, R., Travis, L., 1983. Efficient three-dimensional global models for climate studies: models I and II. Mon. Weather Rev. 111 (4), 609–662. https://doi.org/10.1175/1520-0493(1983)111<0609:ETDGMF>2.0.CO;2.

Heinrich, H., 1988. Origin and consequences of cyclic ice rafting in the Northeast Atlantic ocean during the past 130,000 years. Quat. Res. 29, 142–152. https://doi.org/10.1016/0033-5894(88)90057-9.

Hemming, S.R., 2004. Heinrich events: massive late Pleistocene detritus layers of the North Atlantic and their global climate imprint. Rev. Geophys. 42 (1), RG1005. https://doi.org/10.1029/2003RG000128.

Henry, L.G., McManus, J.F., Curry, W.B., Roberts, N.L., Piotrowski, A.M., Keigwin, L.D., 2016. North Atlantic ocean circulation and abrupt climate change during the last glaciation. Science 353 (6298), 470–474. https://doi.org/10.1126/science.aaf5529.

Hillaire-Marcel, C., Bilodeau, G., 2000. Instabilities in the Labrador Sea water mass structure during the last climatic cycle. Can. J. Earth Sci. 37 (5), 795–809. https://doi.org/10.1139/e99-108.

Hodgson, D.A., Sime, L.C., 2010. Palaeoclimate: southern westerlies and CO_2. Nat. Geosci. 3 (10), 666–667. https://doi.org/10.1038/ngeo970.

Huiskamp, W.N., Meissner, K.J., 2012. Oceanic carbon and water masses during the Mystery Interval: a model-data comparison study. Paleoceanography 27 (PA4206), 1–17. https://doi.org/10.1029/2012PA002368.

Huiskamp, W.N., Meissner, K.J., D'Orgeville, M., 2015. Competition between ocean carbon pumps in simulations with varying Southern Hemisphere westerly wind forcing. Clim. Dyn. 46 (3463), 1–18. https://doi.org/10.1007/s00382-015-2781-0.

Hülse, D., Arndt, S., Wilson, J.D., Munhoven, G., Ridgwell, A., 2017. Understanding the causes and consequences of past marine carbon cycling variability through models. Earth Sci. Rev. 171, 349–382. https://doi.org/10.1016/j.earscirev.2017.06.004.

Hunke, E.C., Lipscomb, W.H., Turner, A.K., 2010. Sea ice models for climate study: retrospective and new directions. J. Glaciol. 56 (200), 1162–1172. https://doi.org/10.3189/002214311796406095.

Hutchins, D.A., Bruland, K.W., 1998. Iron-limited diatom growth and Si:N uptake ratios in a coastal upwelling regime. Nature 393 (6685), 561–564. https://doi.org/10.1038/31203.

Indermühle, A., Monnin, E., Stauffer, B., Stocker, T.F., Wahlen, M., 2000. Atmospheric CO_2 concentration from 60 to 20 kyr BP from the Taylor Dome ice core, Antarctica. Geophys. Res. Lett. 27 (5), 735–738. https://doi.org/10.1029/1999GL010960.

Ito, T., Follows, M.J., 2003. Upper ocean control on the solubility pump of CO_2. J. Mar. Res. 61 (4), 465–489. https://doi.org/10.1357/002224003322384898.

Iudicone, D., Madec, G., Blanke, B., Speich, S., 2008. The role of Southern Ocean surface forcings and mixing in the global conveyor. J. Phys. Oceanogr. 38 (7), 1377–1400. https://doi.org/10.1175/2008JPO3519.1.

Jaccard, S.L., Galbraith, E.D., Martínez-Garcia, A., Anderson, R.F., 2016. Covariation of abyssal Southern Ocean oxygenation and pCO_2 throughout the last ice age. Nature 530, 207–210. https://doi.org/10.1038/nature16514.

Jansen, M.F., 2017. Glacial ocean circulation and stratification explained by reduced atmospheric temperature. Proc. Natl. Acad. Sci. 114 (1), 45–50. https://doi.org/10.1073/pnas.1610438113.

Jickells, T.D., An, Z.S., Andersen, K.K., Baker, A.R., Bergametti, G., Brooks, N., Cao, J.J., Boyd, P.W., Duce, R.A., Hunter, K.A., Kawahata, H., Kubilay, N., la Roche, J., Liss, P.S., Mahowald, N., Prospero, J.M., Ridgwell, A.J., Tegen, I., Torres, R., 2005. Global iron connections between desert dust, ocean biogeochemistry, and climate. Science 308 (5718), 67–71. https://doi.org/10.1126/science.1105959.

Joos, F., Sarmiento, J.L., Siegenthaler, U., 1991. Estimates of the effect of Southern Ocean iron fertilization on atmospheric CO_2 concentrations. Nature 353, 737–740. https://doi.org/10.1038/353737a0.

Kageyama, M., Merkel, U., Otto-Bliesner, B., Prange, M., Abe-Ouchi, A., Lohmann, G., Ohgaito, R., Roche, D.M., Singarayer, J., Swingedouw, D., Zhang, X., 2013. Climatic impacts of fresh water hosing under last glacial Maximum conditions: a multi-model study. Clim. Past 9 (2), 935–953. https://doi.org/10.5194/cp-9-935-2013.

Kageyama, M., Paul, A., Roche, D.M., Van Meerbeeck, C.J., 2010. Modelling glacial climatic millennial-scale variability related to changes in the Atlantic meridional overturning circulation: a review. Quat. Sci. Rev. 29, 2931–2956. https://doi.org/10.1016/j.quascirev.2010.05.029.

Kanfoush, S.L., Hodell, D.A., Charles, C.D., Guilderson, T.P., Mortyn, P.G., Ninnemann, U.S., 2000. Millennial-scale instability of the Antarctic ice sheet during the last glaciation. Science 288 (5472), 1815–1818. https://doi.org/10.1126/science.288.5472.1815.

Keeling, R.F., Visbeck, M., 2001. Palaeoceanography: Antarctic stratification and glacial CO_2. Nature 412, 605–606. https://doi.org/10.1038/35088129.

Keigwin, L.D., Boyle, E.A., 1999. Surface and deep ocean variability in the northern Sargasso Sea during marine isotope stage 3. Paleoceanography 14 (2), 164–170. https://doi.org/10.1029/1998PA900026.

Keigwin, L.D., Jones, G.A., 1994. Western North Atlantic evidence for millennial-scale changes in ocean circulation and climate. J. Geophys. Res. Ocean. 99 (C6), 12397–12410. https://doi.org/10.1029/94JC00525.

Keir, R.S., 1988. On the Late Pleistocene ocean geochemistry and circulation. Paleoceanography 3 (4), 413–445. https://doi.org/10.1029/PA003i004p00413.

Keir, R.S., 1993. Cold surface ocean ventilation and its effect on atmospheric CO_2. J. Geophys. Res. 98 (C1), 849–856. https://doi.org/10.1029/92JC02323.

Kienast, S.S., Winckler, G., Lippold, J., Albani, S., Mahowald, N.M., 2016. Tracing dust input to the global ocean using thorium isotopes in marine sediments: ThoroMap. Glob. Biogeochem. Cycles 30 (10), 1526–1541. https://doi.org/10.1002/2016GB005408.

Kim, S.J., Flato, G.M., Boer, G.J., McFarlane, N.A., 2002. A coupled climate model simulation of the Last Glacial Maximum, part 1: transient multi-decadal response. Clim. Dyn. 19 (5–6), 515–537. https://doi.org/10.1007/s00382-002-0243-y.

Kim, S.J., Jun, S.Y., Kim, B.M., 2017. Sensitivity of southern hemisphere westerly wind to boundary conditions for the last glacial maximum. Quat. Int. 459, 165–174. https://doi.org/10.1016/j.quaint.2017.04.001.

Kim, S.J., Lee, B.Y., 2009. Westerly winds in the Southern Ocean during the last glacial maximum simulated in CCM3. Ocean Polar Res. 31 (4), 297–304. https://doi.org/10.4217/OPR.2009.31.4.297.

Kissel, C., Laj, C., Labeyrie, L., Dokken, T., Voelker, A., Blamart, D., 1999. Rapid climatic variations during marine isotopic stage 3: magnetic analysis of sediments from Nordic Seas and North Atlantic. Earth Planet. Sci. Lett. 171 (3), 489–502. https://doi.org/10.1016/S0012-821X(99)00162-4.

Klocker, A., 2018. Opening the window to the Southern Ocean: the role of jet dynamics. Sci. Adv. 4 (eaao4719), 1–12. https://doi.org/10.1126/sciadv.aao4719.

Knox Ennever, F., McElroy, M.B., 1981. Changes in atmospheric CO_2: factors regulating the glacial to interglacial transition. In: Sundquist, E.T., Broecker, W.S. (Eds.), Geophysical Monograph Series 32. The Carbon Cycle and Atmospheric CO_2: Natural Variations Archean to Present, pp. 154–162. https://doi.org/10.1029/GM032p0154.

Knox, F., McElroy, M.B., 1984. Changes in atmospheric CO_2: influence of the marine biota at high latitude. J. Geophys. Res. 89 (D3), 4629–4637. https://doi.org/10.1029/JD089iD03p04629.

Knutti, R., Flückiger, J., Stocker, T.F., Timmermann, A., 2004. Strong hemispheric coupling of glacial climate through freshwater discharge and ocean circulation. Nature 430 (7002), 851–856. https://doi.org/10.1038/nature02786.

Kobayashi, H., Abe-Ouchi, A., Oka, A., 2015. Role of Southern Ocean stratification in glacial atmospheric CO_2 reduction evaluated by a three-dimensional ocean general circulation model. Paleoceanography 30 (9), 1202–1216. https://doi.org/10.1002/2015PA002786.

Kohfeld, K.E., Graham, R.M., de Boer, A.M., Sime, L.C., Wolff, E.W., Le Quéré, C., Bopp, L., 2013. Southern Hemisphere westerly wind changes during the Last Glacial Maximum: paleo-data synthesis. Quat. Sci. Rev. 68, 76–95. https://doi.org/10.1016/j.quascirev.2013.01.017.

Kohfeld, K.E., Harrison, S.P., 2001. DIRTMAP: the geological record of dust. Earth Sci. Rev. 54 (1–3), 81–114. https://doi.org/10.1016/S0012-8252(01)00042-3.

Kohfeld, K.E., Ridgwell, A.J., 2009. Glacial-interglacial variability in atmospheric CO_2. In: Le Quéré, C., Saltzman, E. (Eds.), American Geophysical Union Geophysical Research Series 187: Surface Ocean - Lower Atmosphere Processes. American Geophysical Union, Washington, DC, USA, pp. 251–286. https://doi.org/10.1029/2008gm000845.

Köhler, P., Fischer, H., 2006. Simulating low frequency changes in atmospheric CO_2 during the last 740,000 years. Clim. Past 2, 57–78. https://doi.org/10.5194/cp-2-57-2006.

Köhler, P., Fischer, H., Munhoven, G., Zeebe, R.E., 2005a. Quantitative interpretation of atmospheric carbon records over the last glacial termination. Glob. Biogeochem. Cycles 19 (4), GB4020. https://doi.org/10.1029/2004GB002345.

Köhler, P., Joos, F., Gerber, S., Knutti, R., 2005b. Simulated changes in vegetation distribution, land carbon storage, and atmospheric CO_2 in response to a collapse of the North Atlantic thermohaline circulation. Clim. Dyn. 25 (7), 689–708. https://doi.org/10.1007/s00382-005-0058-8.

Köhler, P., Muscheler, R., Fischer, H., 2006. A model-based interpretation of low-frequency changes in the carbon cycle during the last 120,000 years and its implications for the reconstruction of atmospheric $\Delta^{14}C$. Geochem. Geophys. Geosyst. 7 (11), Q11N06. https://doi.org/10.1029/2005GC001228.

Köhler, P., Nehrbass-Ahles, C., Schmitt, J., Stocker, T.F., Fischer, H., 2017. A 156 kyr smoothed history of the atmospheric greenhouse gases CO_2, CH_4, and N_2O and their radiative forcing. Earth Syst. Sci. Data 9, 363–387. https://doi.org/10.5194/essd-9-363-2017.

Kurahashi-Nakamura, T., Abe-Ouchi, A., Yamanaka, Y., Misumi, K., 2007. Compound effects of Antarctic sea ice on atmospheric pCO_2 change during glacial-interglacial cycle. Geophys. Res. Lett. 34 (L20708), 1–5. https://doi.org/10.1029/2007GL030898.

Kurz, K.D., Maier-Reimer, E., 1993. Iron fertilization of the austral ocean - the Hamburg Model assessment. Glob. Biogeochem. Cycles 7 (1), 229–244. https://doi.org/10.1029/92GB02910.

Kwon, E.Y., Primeau, F., Sarmiento, J.L., 2009. The impact of remineralization depth on the air-sea carbon balance. Nat. Geosci. 2 (9), 630–635. https://doi.org/10.1038/ngeo612.

Lambert, F., Bigler, M., Steffensen, J.P., Hutterli, M., Fischer, H., 2012. Centennial mineral dust variability in high-resolution ice core data from Dome C, Antarctica. Clim. Past 8 (2), 609–623. https://doi.org/10.5194/cp-8-609-2012.

Lambert, F., Delmonte, B., Petit, J.-R., Bigler, M., Kaufmann, P.R., Hutterli, M.A., Stocker, T.F., Ruth, U., Steffensen, J.P., Maggi, V., 2008. Dust-climate couplings over the past 800,000 years from the EPICA Dome C ice core. Nature 452 (7187), 616–619. https://doi.org/10.1038/nature06763.

Lambert, F., Kug, J.S., Park, R.J., Mahowald, N., Winckler, G., Abe-Ouchi, A., O'Ishi, R., Takemura, T., Lee, J.H., 2013. The role of mineral-dust aerosols in polar temperature amplification. Nat. Clim. Change 3 (5), 487–491. https://doi.org/10.1038/nclimate1785.

Lambert, F., Tagliabue, A., Shaffer, G., Lamy, F., Winckler, G., Farias, L., Gallardo, L., De Pol-Holz, R., 2015. Dust fluxes and iron fertilization in Holocene and last glacial maximum climates. Geophys. Res. Lett. 42, 6014–6023. https://doi.org/10.1002/2015GL064250.

Lamy, F., Gersonde, R., Winckler, G., Esper, O., Jaeschke, A., Kuhn, G., Ullermann, J., Martinez-Garcia, A., Lambert, F., Kilian, R., 2014. Increased dust deposition in the Pacific Southern Ocean during glacial periods. Science 343 (6169), 403–407. https://doi.org/10.1126/science.1245424.

Lamy, F., Hebbeln, D., Wefer, G., 1999. High-resolution marine record of climatic change in mid-latitude Chile during the last 28,000 years based on terrigenous sediment parameters. Quat. Res. 51 (1), 83–93. https://doi.org/10.1006/qres.1998.2010.

Lamy, F., Kaiser, J., Arz, H.W., Hebbeln, D., Ninnemann, U., Timm, O., Timmermann, A., Toggweiler, J.R., 2007. Modulation of the bipolar seesaw in the southeast Pacific during termination 1. Earth Planet. Sci. Lett. 259 (3), 400–413. https://doi.org/10.1016/j.epsl.2007.04.040.

Landais, A., Masson-Delmotte, V., Stenni, B., Selmo, E., Roche, D.M., Jouzel, J., 2015. A review of the bipolar seesaw from synchronized and high resolution ice core water stable isotope records from Greenland and. Quat. Sci. Rev. 114, 18–32. https://doi.org/10.1016/j.quascirev.2015.01.031.

Latimer, J.C., Filippelli, G.M., 2001. Terrigenous input and paleoproductivity in the Southern Ocean. Paleoceanography 16 (6), 627–643. https://doi.org/10.1029/2000PA000586.

Lauderdale, J.M., Garabato, A.C.N., Oliver, K.I.C., Follows, M.J., Williams, R.G., 2013. Wind-driven changes in Southern Ocean residual circulation, ocean carbon reservoirs and atmospheric CO_2. Clim. Dyn. 41 (7–8), 2145–2164. https://doi.org/10.1007/s00382-012-1650-3.

Lauderdale, J.M., Williams, R.G., Munday, D.R., Marshall, D.P., 2017. The impact of Southern Ocean residual upwelling on atmospheric CO_2 on centennial and millennial timescales. Clim. Dyn. 48 (5–6), 1611–1631. https://doi.org/10.1007/s00382-016-3163-y.

Lee, S.Y., Chiang, J.C.H., Matsumoto, K., Tokos, K.S., 2011. Southern Ocean wind response to North Atlantic cooling and the rise in atmospheric CO_2: modeling perspective and paleoceanographic implications. Paleoceanography 26 (26), 1214. https://doi.org/10.1029/2010PA002004.

Lefèvre, N., Watson, A.J., 1999. Modeling the geochemical cycle of iron in the oceans and its impact on atmospheric CO_2 concentrations. Glob. Biogeochem. Cycles 13 (3), 727–736. https://doi.org/10.1029/1999GB900034.

Li, C., Born, A., 2019. Coupled atmosphere-ice-ocean dynamics in Dansgaard-Oeschger events. Quat. Sci. Rev. 203 (5020), 1–20. https://doi.org/10.1016/j.quascirev.2018.10.031.

Liu, W., Lu, J., Leung, L.R., Xie, S.P., Liu, Z., Zhu, J., 2015. The de-correlation of westerly winds and westerly-wind stress over the Southern Ocean during the Last Glacial Maximum. Clim. Dyn. 45 (11–12), 3157–3168. https://doi.org/10.1007/s00382-015-2530-4.

Loose, B., McGillis, W.R., Perovich, D., Zappa, C.J., Schlosser, P., 2014. A parameter model of gas exchange for the seasonal sea ice zone. Ocean Sci. 10 (1), 17–28. https://doi.org/10.5194/os-10-17-2014.

Lunt, D.J., Valdes, P.J., 2001. Dust transport to Dome C, Antarctica, at the last glacial maximum and present day. Geophys. Res. Lett. 28 (2), 295–298. https://doi.org/10.1029/2000GL012170.

Lunt, D.J., Valdes, P.J., 2002. Dust deposition and provenance at the Last Glacial Maximum and present day. Geophys. Res. Lett. 29 (22), 42-1–42-4. https://doi.org/10.1029/2002GL015656.

Lüthi, D., Le Floch, M., Bereiter, B., Blunier, T., Barnola, J.-M., Siegenthaler, U., Raynaud, D., Jouzel, J., Fischer, H., Kawamura, K., Stocker, T.F., 2008. High-resolution carbon dioxide concentration record 650,000-800,000 years before present. Nature 453, 379–382. https://doi.org/10.1038/nature06949.

Lynch-Stieglitz, J., 2017. The Atlantic Meridional Overturning Circulation and Abrupt Climate Change. Ann. Rev. Mar. Sci. 9 (1), 83–104. https://doi.org/10.1146/annurev-marine-010816-060415.

Lynch-Stieglitz, J., Schmidt, M.W., Henry, L.G., Curry, W.B., Skinner, L.C., Mulitza, S., Zhang, R., Chang, P., 2014. Muted change in Atlantic overturning circulation over some glacial-aged Heinrich events. Nat. Geosci. 7, 144–150. https://doi.org/10.1038/ngeo2045.

Ma, H., Wu, L., 2011. Global teleconnections in response to freshening over the Antarctic Ocean. J. Clim. 24 (4), 1071–1088. https://doi.org/10.1175/2010JCLI3634.1.

Maher, B.A., Prospero, J.M., Mackie, D., Gaiero, D., Hesse, P.P., Balkanski, Y., 2010. Global connections between aeolian dust, climate and ocean biogeochemistry at the present day and at the last glacial maximum. Earth Sci. Rev. 99 (1), 61–97. https://doi.org/10.1016/j.earscirev.2009.12.001.

Mahowald, N., Kohfeld, K., Hansson, M., Balkanski, Y., Harrison, S.P., Prentice, I.C., Schulz, M., Rodhe, H., 1999. Dust sources and deposition during the last glacial maximum and current climate: a comparison of model results with paleodata from ice cores and marine sediments. J. Geophys. Res. Atmos. 104 (D13), 15895–15916. https://doi.org/10.1029/1999JD900084.

Mahowald, N.M., Kiehl, L.M., 2003. Mineral aerosol and cloud interactions. Geophys. Res. Lett. 30 (9), 1475. https://doi.org/10.1029/2002GL016762.

Mahowald, N.M., Muhs, D.R., Levis, S., Rasch, P.J., Yoshioka, M., Zender, C.S., Luo, C., 2006. Change in atmospheric mineral aerosols in response to climate: last glacial period, preindustrial, modern, and doubled carbon dioxide climates. J. Geophys. Res. Atmos. 111 (D10202), 1–22. https://doi.org/10.1029/2005JD006653.

Manabe, S., 1969a. Climate and the Ocean Circulation. 1. The atmospheric circulation and the hydrology of the Earth's surface. Mon. Weather Rev. 97 (11), 739–774. https://doi.org/10.1175/1520-0493(1969)097<0739:CATOC>2.3.CO;2.

Manabe, S., 1969b. Climate and the ocean circulation. 2. The atmospheric circulation and the effect of heat transfer by ocean currents. Mon. Weather Rev. 97 (11), 775–805. https://doi.org/10.1175/1520-0493(1969)097<0775:CATOC>2.3.CO;2.

Manabe, S., Stouffer, R.J., 1988. Two stable equilibria of a coupled ocean-atmosphere model. J. Clim. 1, 841–866. https://doi.org/10.1175/1520-0442(1993)006<0175:COSEOA>2.0.CO;2.

Manabe, S., Stouffer, R.J., 1995. Simulation of abrupt climate change induced by freshwater input to the North Atlantic Ocean. Nature 378 (6553), 165–167. https://doi.org/10.1038/378165a0.

Marchal, O., Stocker, T.F., Joos, F., 1998. Impact of oceanic reorganizations on the ocean carbon cycle and atmospheric carbon dioxide content. Paleoceanography 13 (3), 225–244. https://doi.org/10.1029/98PA00726.

Marchal, O., Stocker, T.F., Joos, F., Indermühle, A., Blunier, T., Tschumi, J., 1999. Modelling the concentration of atmospheric CO_2 during the Younger Dryas climate event. Clim. Dyn. 15 (5), 341–354. https://doi.org/10.1007/s003820050286.

Marcott, S. a, Clark, P.U., Padman, L., Klinkhammer, G.P., Springer, S.R., Liu, Z., Otto-Bliesner, B.L., Carlson, A.E., Ungerer, A., Padman, J., He, F., Cheng, J., Schmittner, A., 2011. Ice-shelf collapse from subsurface warming as a trigger for Heinrich events. Proc. Natl. Acad. Sci. 108 (33), 13415–13419. https://doi.org/10.1073/pnas.1104772108.

Marcott, S.A., Bauska, T.K., Buizert, C., Steig, E.J., Rosen, J.L., Cuffey, K.M., Fudge, T.J., Severinghaus, J.P., Ahn, J., Kalk, M.L., McConnell, J.R., Sowers, T., Taylor, K.C., White, J.W.C., Brook, E.J., 2014. Centennial-scale changes in the global carbon cycle during the last deglaciation. Nature 514 (7524), 616–619. https://doi.org/10.1038/nature13799.

Marinov, I., Follows, M., Gnanadesikan, A., Sarmiento, J.L., Slater, R.D., 2008a. How does ocean biology affect atmospheric pCO_2? Theory and models. J. Geophys. Res. 113, C07032. https://doi.org/10.1029/2007JC004598.

Marinov, I., Gnanadesikan, A., Sarmiento, J.L., Toggweiler, J.R., Follows, M., Mignone, B.K., 2008b. Impact of oceanic circulation on biological carbon storage in the ocean and atmospheric pCO_2. Glob. Biogeochem. Cycles 22 (3), GB3007. https://doi.org/10.1029/2007GB002958.

Mariotti, V., Bopp, L., Tagliabue, A., Kageyama, M., Swingedouw, D., 2012. Marine productivity response to Heinrich events: a model-data comparison. Clim. Past 8 (5), 1581–1598. https://doi.org/10.5194/cp-8-1581-2012.

Markle, B.R., Steig, E.J., Buizert, C., Schoenemann, S.W., Bitz, C.M., Fudge, T.J., Pedro, J.B., Ding, Q., Jones, T.R., White, J.W.C., Sowers, T., 2017. Global atmospheric teleconnections during Dansgaard–Oeschger events. Nat. Geosci. 10, 36–40. https://doi.org/10.1038/ngeo2848.

Markle, B.R., Steig, E.J., Roe, G.H., Winckler, G., McConnell, J.R., 2018. Concomitant variability in high-latitude aerosols, water isotopes and the hydrologic cycle. Nat. Geosci. 11, 853–859. https://doi.org/10.1038/s41561-018-0210-9.

Marotzke, J., Willebrand, J., 1991. Multiple equilibria of the global thermohaline circulation. J. Phys. Oceanogr. 21 (9), 1372–1385. https://doi.org/10.1175/1520-0485(1991)021<1372:MEOTGT>2.0.CO;2.

Martin, J.H., Gordon, R.M., Fitzwater, S.E., 1990. Iron in Antarctic waters. Nature 345, 156–158. https://doi.org/10.1038/345156a0.

Martínez-García, A., Sigman, D.M., Ren, H., Anderson, R.F., Straub, M., Hodell, D.A., Jaccard, S.L., Eglinton, T.I., Haug, G.H., 2014. Iron fertilization of the subantarctic ocean during the last ice age. Science 343 (6177), 1347–1350. https://doi.org/10.1126/science.1246848.

Marzocchi, A., Jansen, M., 2017. Connecting Antarctic sea ice to deep ocean circulation in modern and glacial climate simulations. Geophys. Res. Lett. 44, 6286–6295. https://doi.org/10.1002/2017GL073936.

Matsumoto, K., Hashioka, T., Yamanaka, Y., 2007. Effect of temperature-dependent organic carbon decay on atmospheric pCO_2. J. Geophys. Res. 112 (G02007), 1–9. https://doi.org/10.1029/2006JG000187.

Matsumoto, K., Sarmiento, J.L., Brzezinski, M.A., 2002. Silicic acid leakage from the Southern Ocean: a possible explanation for glacial atmospheric pCO_2. Glob. Biogeochem. Cycles 16 (3), 1031. https://doi.org/10.1029/2001GB001442.

Matsumoto, K., Yokoyama, Y., 2013. Atmospheric $\Delta^{14}C$ reduction in simulations of Atlantic overturning circulation shutdown. Glob. Biogeochem. Cycles 27, 296–304. https://doi.org/10.1002/gbc.20035.

Mayr, C., Lücke, A., Wagner, S., Wissel, H., Ohlendorf, C., Haberzettl, T., Oehlerich, M., Schäbitz, F., Wille, M., Zhu, J., others, 2013. Intensified Southern Hemisphere Westerlies regulated atmospheric CO_2 during the last deglaciation. Geology 41 (8), 831–834. https://doi.org/10.1130/G34335.1.

McManus, J.F., François, R., Gherardi, J., Keigwin, L.D., 2004. Collapse and rapid resumption of Atlantic meridional circulation linked to deglacial climate changes. Nature 428 (6985), 834–837. https://doi.org/10.1038/nature02494.

Meissner, K.J., 2007. Younger Dryas: a data to model comparison to constrain the strength of the overturning circulation. Geophys. Res. Lett. 34 (21), 2–6. https://doi.org/10.1029/2007GL031304.

Menviel, L., England, M.H., Meissner, K.J., Mouchet, A., Yu, J., 2014. Atlantic-Pacific seesaw and its role in outgassing CO_2 during Heinrich events. Paleoceanography 29 (1), 58–70. https://doi.org/10.1002/2013PA002542.

Menviel, L., Joos, F., Ritz, S.P., 2012. Simulating atmospheric CO_2, ^{13}C and the marine carbon cycle during the Last Glacial-Interglacial cycle: possible role for a deepening of the mean remineralization depth and an increase in the oceanic nutrient inventory. Quat. Sci. Rev. 56, 46–68. https://doi.org/10.1016/j.quascirev.2012.09.012.

Menviel, L., Mouchet, A., Meissner, K.J., Joos, F., England, M.H., 2015a. Impact of oceanic circulation changes on atmospheric $\delta^{13}CO_2$. Glob. Biogeochem. Cycles 29, 1944–1961. https://doi.org/10.1002/2015GB005207.

Menviel, L., Spence, P., England, M.H., 2015b. Contribution of enhanced Antarctic Bottom Water formation to Antarctic warm events and millennial-scale atmospheric CO_2 increase. Earth Planet. Sci. Lett. 413, 37–50. https://doi.org/10.1016/j.epsl.2014.12.050.

Menviel, L., Spence, P., Yu, J., Chamberlain, M.A., Matear, R.J., Meissner, K.J., England, M.H., 2018. Southern Hemisphere westerlies as a driver of the early deglacial atmospheric CO_2 rise. Nat. Commun. 9 (1), 2503. https://doi.org/10.

1038/s41467-018-04876-4.

Menviel, L., Timmermann, A., Mouchet, A., Timm, O., 2008a. Meridional reorganizations of marine and terrestrial productivity during Heinrich events. Paleoceanography 23 (1), PA1203. https://doi.org/10.1029/2007PA001445.

Menviel, L., Timmermann, A., Mouchet, A., Timm, O., 2008b. Climate and marine carbon cycle response to changes in the strength of the Southern Hemispheric westerlies. Paleoceanography 23 (4), PA4201. https://doi.org/10.1029/2008PA001604.

Menviel, L., Timmermann, A., Timm, O.E., Mouchet, A., 2010. Climate and biogeochemical response to a rapid melting of the West Antarctic Ice sheet during interglacials and implications for future climate. Paleoceanography 25 (4), 1–12. https://doi.org/10.1029/2009PA001892.

Mikolajewicz, U., Maier-Reimer, E., 1994. Mixed boundary-conditions in ocean general-circulation models and their influence on the stability of the models conveyor belt. J. Geophys. Res. 99 (C11), 22633–22644. https://doi.org/10.1029/94JC01989.

Miller, R.L., Tegen, I., 1998. Climate response to soil dust aerosols. J. Clim. 11 (12), 3247–3267. https://doi.org/10.1175/1520-0442(1998)011<3247:CRTSDA>2.0.CO;2.

Miller, R.L., Tegen, I., Perlwitz, J., 2004. Surface radiative forcing by soil dust aerosols and the hydrologic cycle. J. Geophys. Res. Atmos. 109 (D04203), 1–24. https://doi.org/10.1029/2003JD004085.

Monnin, E., Indermühle, A., Dällenbach, A., Flückiger, J., Stauffer, B., Stocker, T.F., Raynaud, D., Barnola, J.M., 2001. Atmospheric CO_2 concentrations over the last glacial termination. Science 291 (5501), 112–114. https://doi.org/10.1126/science.291.5501.112.

Montade, V., Kageyama, M., Combourieu-Nebout, N., Ledru, M.P., Michel, E., Siani, G., Kissel, C., 2015. Teleconnection between the intertropical convergence zone and southern westerly winds throughout the last deglaciation. Geology 43 (8), 735–738. https://doi.org/10.1130/G36745.1.

Morales Maqueda, M.A., Rahmstorf, S., 2002. Did Antarctic sea-ice expansion cause glacial CO_2 decline? Geophys. Res. Lett. 29 (1), 11. https://doi.org/10.1029/2001GL013240.

Moreno, P.I., Villa-Martínez, R., Cárdenas, M.L., Sagredo, E.A., 2012. Deglacial changes of the southern margin of the southern westerly winds revealed by terrestrial records from SW Patagonia (52°S). Quat. Sci. Rev. 41, 1–21. https://doi.org/10.1016/j.quascirev.2012.02.002.

Morrison, A.K., Hogg, A.M., 2013. On the relationship between Southern Ocean overturning and ACC transport. J. Phys. Oceanogr. 43 (1), 140–148. https://doi.org/10.1175/JPO-D-12-057.1.

Muglia, J., Somes, C.J., Nickelsen, L., Schmittner, A., 2017. Combined effects of atmospheric and seafloor iron fluxes to the glacial ocean. Paleoceanography 32 (11), 1204–1218. https://doi.org/10.1002/2016PA003077.

Munday, D.R., Johnson, H.L., Marshall, D.P., 2014. Impacts and effects of mesoscale ocean eddies on ocean carbon storage and atmospheric pCO_2. Glob. Biogeochem. Cycles 28, 877–896. https://doi.org/10.1002/2014GB004836.

Munhoven, G., François, L.M., 1996. Glacial-interglacial variability of atmospheric CO_2 due to changing continental silicate rock weathering: a model study. J. Geophys. Res. 101 (D16), 21423–21437. https://doi.org/10.1029/96JD01842.

Neftel, A., Oeschger, H., Schwander, J., Stauffer, B., Zumbrunn, R., 1982. Ice core sample measurements give atmospheric CO_2 content during the past 40,000 yr. Nature 295 (5846), 220–223. https://doi.org/10.1038/295220a0.

NGRIP members, 2004. High-resolution record of Northern Hemisphere climate extending into the last interglacial period. Nature 431, 147–151. https://doi.org/10.1038/nature02805.

Nishioka, J., Obata, H., 2017. Dissolved iron distribution in the western and central subarctic Pacific: HNLC water formation and biogeochemical processes. Limnol. Oceanogr. 62 (5), 2004–2022. https://doi.org/10.1002/lno.10548.

Obata, A., 2007. Climate-carbon cycle model response to freshwater discharge into the North Atlantic. J. Clim. 20 (24), 5962–5976. https://doi.org/10.1175/2007JCLI1808.1.

Ödalen, M., Nycander, J., Oliver, K.I.C., Brodeau, L., Ridgwell, A., 2018. The influence of the ocean circulation state on ocean carbon storage and CO_2 drawdown potential in an Earth system model. Biogeosciences 15, 1367–1393. https://doi.org/10.5194/bg-15-1367-2018.

Oeschger, H., Siegenthaler, U., Schotterer, U., Gugelmann, A., 1975. A box diffusion model to study the carbon dioxide exchange in nature. Tellus 27 (2), 168–192. https://doi.org/10.1111/j.2153-3490.1975.tb01671.x.

Oka, A., Abe-Ouchi, A., Chikamoto, M.O., Ide, T., 2011. Mechanisms controlling export production at the LGM: effects of changes in oceanic physical fields and atmospheric dust deposition. Glob. Biogeochem. Cycles 25, 1–12. https://doi.org/10.1029/2009GB003628.

Okazaki, Y., Timmermann, A., Menviel, L., Harada, N., Abe-Ouchi, A., Chikamoto, M.O., Mouchet, A., Asahi, H., 2010. Deepwater formation in the north Pacific during the last glacial termination. Science 329, 200–205. https://doi.org/10.1126/science.1190612.

Opdyke, B.N., Walker, J.C.G., 1992. Return of the coral reef hypothesis: basin to shelf partitioning of $CaCO_3$ and its effect on atmospheric CO_2. Geology 20 (8), 733–736. https://doi.org/10.1130/0091-7613(1992)020<0733:ROTCRH>2.3.CO;2.

Oreskes, N., Shrader-Frechette, K., Belitz, K., 1994. Verification, Validation, and Confirmation of Numerical Models in the Earth Sciences. Science 263 (5147), 641–646. https://doi.org/10.1126/science.263.5147.641.

Otto-Bliesner, B.L., Brady, E.C., Clauzet, G., Tomas, R., Levis, S., Kothavala, Z., 2006. Last Glacial Maximum and Holocene Climate in CCSM3. J. Clim. 19 (11), 2526–2544. https://doi.org/10.1175/JCLI3748.1.

Paillard, D., Parrenin, F., 2004. The Antarctic ice sheet and the triggering of deglaciations. Earth Planet. Sci. Lett. 227 (3–4), 263–271. https://doi.org/10.1016/j.epsl.2004.08.023.

Parekh, P., Dutkiewicz, S., Follows, M.J., Ito, T., 2006a. Atmospheric carbon dioxide in a less dusty world. Geophys. Res. Lett. 33 (L03610), 2–5. https://doi.org/10.1029/2005GL025098.

Parekh, P., Follows, M.J., Dutkiewicz, S., Ito, T., 2006b. Physical and biological regulation of the soft tissue carbon pump. Paleoceanography 21 (PA3001), 1–11. https://doi.org/10.1029/2005PA001258.

Parekh, P., Joos, F., Müller, S.A., 2008. A modeling assessment of the interplay between aeolian iron fluxes and iron-binding ligands in controlling carbon dioxide fluctuations during Antarctic warm events. Paleoceanography 23 (4), PA4202. https://doi.org/10.1029/2007PA001531.

Pedro, J.B., Jochum, M., Buizert, C., He, F., Barker, S., Rasmussen, S.O., 2018. Beyond the bipolar seesaw: toward a process understanding of interhemispheric coupling. Quat. Sci. Rev. 192, 27–46. https://doi.org/10.1016/j.quascirev.2018.05.005.

Peltier, W.R., Vettoretti, G., 2014. Dansgaard-Oeschger oscillations predicted in a comprehensive model of glacial climate: a "kicked" salt oscillator in the Atlantic. Geophys. Res. Lett. 41 (20), 7306–7313. https://doi.org/10.1002/2014GL061413.

Peng, T.-H., Broecker, W.S., 1991. Dynamical limitations on the Antarctic iron fertilization strategy. Nature 349, 227–229. https://doi.org/10.1038/353737a0.

Person, R., Aumont, O., Lévy, M., 2018. The biological pump and seasonal variability of pCO_2 in the Southern Ocean: exploring the role of diatom adaptation to low iron. J. Geophys. Res. Ocean. 123, 1–23. https://doi.org/10.1029/2018JC013775.

Petit, J.-R., Jouzel, J., Raynaud, D., Barkov, N.I., Barnola, J.-M., Basile, I., Bender, M., Chappellaz, J., Davis, M., Delaygue, G., Delmotte, M., Kotlyakov, V.M., Legrand, M., Lipenkov, V.Y., Lorius, C., L. Pepin, L., Ritz, C., Saltzman, E., Stievenard, M., 1999. Climate and atmospheric history of the past 420,000 years from the Vostok ice core, Antarctica. Nature 399 (6735), 429–436. https://doi.org/10.1038/20859.

Pichevin, L.E., Ganeshram, R.S., Geibert, W., Thunell, R., Hinton, R., 2014. Silica burial enhanced by iron limitation in oceanic upwelling margins. Nat. Geosci. 7, 541–546. https://doi.org/10.1038/ngeo2181.

Poulsen, M.B., Jochum, M., Nuterman, R., 2018. Parameterized and resolved Southern Ocean eddy compensation. Ocean Model. 124, 1–15. https://doi.org/10.1016/j.ocemod.2018.01.008.

Praetorius, S.K., McManus, J.F., Oppo, D.W., Curry, W.B., 2008. Episodic reductions in bottom-water currents since the last ice age. Nat. Geosci. 1 (7), 449–452. https://doi.org/10.1038/ngeo227.

Prange, M., Lohmann, G., Paul, A., 2003. Influence of vertical mixing on the thermohaline hysteresis: analyses of an OGCM. J. Phys. Oceanogr. 33 (8), 1707–1721. https://doi.org/10.1175/2389.1.

Prentice, K.C., Fung, I.Y., 1990. The sensitivity of terrestrial carbon storage to climate change. Nature 346, 48–51. https://doi.org/10.1038/346048a0.

Putnam, A.E., Denton, G.H., Schaefer, J.M., Barrell, D.J.A., Andersen, B.G., Finkel, R.C., Schwartz, R., Doughty, A.M., Kaplan, M.R., Schlüchter, C., 2010. Glacier advance in southern middle-latitudes during the Antarctic cold reversal. Nat. Geosci. 3 (10), 700–704. https://doi.org/10.1038/ngeo962.

Quade, J., Kaplan, M.R., 2017. Lake-level stratigraphy and geochronology revisited at Lago (Lake) Cardiel, Argentina, and changes in the Southern Hemispheric Westerlies over the last 25 ka. Quat. Sci. Rev. 177, 173–188. https://doi.org/10.1016/j.quascirev.2017.10.006.

Rae, J.W.B., Burke, A., Robinson, L.F., Adkins, J.F., Chen, T., Cole, C., Greenop, R., Li, T., Littley, E.F.M., Nita, D.C., Stewart, J.A., Taylor, B.J., 2018. CO_2 storage and release in the deep Southern Ocean on millennial to centennial timescales. Nature 562, 569–573. https://doi.org/10.1038/s41586-018-0614-0.

Rahmstorf, S., 2002. Ocean circulation and climate during the past 120,000 years. Nature 419 (6903), 207–214. https://doi.org/10.1038/nature01090.

Rahmstorf, S., Crucifix, M., Ganopolski, A., Goosse, H., Kamenkovich, I., Knutti, R., Lohmann, G., Marsh, R., Mysak, L.A., Wang, Z., Weaver, A.J., 2005. Thermohaline circulation hysteresis: a model intercomparison. Geophys. Res. Lett. 32 (23), L23605. https://doi.org/10.1029/2005GL023655.

Raiswell, R., Benning, L.G., Tranter, M., Tulaczyk, S., 2008. Bioavailable iron in the Southern Ocean: the significance of the iceberg conveyor belt. Geochem. Trans. 9, 7. https://doi.org/10.1186/1467-4866-9-7.

Raiswell, R., Canfield, D.E., 2012. The Iron Biogeochemical Cycle Past and Present, Geochemical Perspectives. European Association for Geochemistry, Houten, NED.

Randall, D.A., Wood, R.A., Bony, S., Colman, R., Fichefet, T., Fyfe, J., Kattsov, V., Pitman, A., Shukla, J., Srinivasan, J., Sumi, A., Stouffer, R.J., Taylo, K.E., 2007. Climate models and their evaluation. In: Solomon, S., Qin, D., Manning, M., Chen, Z., Marquis, M., Averyt, K.B., Tignor, M., Miller, H.L. (Eds.), Climate Change 2007: the Physical Science Basis. Contribution of Working Group I to the Fourth Assessment Report of the Intergovernmental Panel on Climate Change. Cambridge University Press, Cambridge, UK and New York, USA, pp. 589–662.

Rea, D.K., 1994. The paleoclimatic deposition record provided of wind by eolian in the deep sea: the geologic history of wind. Rev. Geophys. 32 (2), 159–195. https://doi.org/10.1029/93RG03257.

Richardson, G., Wadley, M.R., Heywood, K.J., Stevens, D.P., Banks, H.T., 2005. Short-term climate response to a freshwater pulse in the Southern Ocean. Geophys. Res. Lett. 32 (3), 1–4. https://doi.org/10.1029/2004GL021586.

Ridgwell, A.J., 2001. Glacial-interglacial Perturbations in the Global Carbon Cycle, PhD Thesis. University of East Anglia at Norwich, UK.

Ridgwell, A.J., 2003. Implications of the glacial CO_2 "iron hypothesis" for Quaternary climate change. Geochem. Geophys. Geosyst. 4 (9), 1–10. https://doi.org/10.1029/2003GC000563.

Ridgwell, A.J., Watson, A.J., 2002. Feedback between aeolian dust, climate, and atmospheric CO_2 in glacial time. Paleoceanography 17 (4), 1–14. https://doi.org/10.1029/2001PA000729.

Ridgwell, A.J., Watson, A.J., Maslin, M.A., Kaplan, J.O., 2003. Implications of coral reef buildup for the controls on atmospheric CO_2 since the last glacial maximum. Paleoceanography 18 (4), 1–7. https://doi.org/10.1029/2003PA000893.

Rind, D., DeMenocal, P., Russell, G., Sheth, S., Collins, D., Schmidt, G., Teller, J., 2001a. Effects of glacial meltwater in the GISS coupled atmosphere-ocean model 1. North Atlantic Deep Water response. J. Geophys. Res. Atmos. 106 (D21), 27355–27365. https://doi.org/10.1029/2000JD000070.

Rind, D., Russell, G., Schmidt, G., Sheth, S., Collins, D., DeMenocal, P., Teller, J., 2001b. Effects of glacial meltwater in the GISS coupled atmosphere-ocean model - 2. A bipolar seesaw in Atlantic Deep Water production. J. Geophys. Res. 106 (D21), 27355–27365. https://doi.org/10.1029/2001JD000954.

Roche, D., Paillard, D., Cortijo, E., 2004. Constraints on the duration and freshwater release of Heinrich event 4 through isotope modelling. Nature 432 (7015), 379–382. https://doi.org/10.1038/nature03059.

Roche, D.M., Crosta, X., Renssen, H., 2012. Evaluating Southern Ocean sea-ice for the Last Glacial Maximum and pre-industrial climates: PMIP-2 models and data evidence. Quat. Sci. Rev. 56, 99–106. https://doi.org/10.1016/j.quascirev.2012.09.020.

Rodgers, K.B., Mikaloff-Fletcher, S.E., Bianchi, D., Beaulieu, C., Galbraith, E.D., Gnanadesikan, A., Hogg, A.G., Iudicone, D., Lintner, B.R., Naegler, T., Reimer, P.J., Sarmiento, J.L., Slater, R.D., 2011. Interhemispheric gradient of atmospheric radiocarbon reveals natural variability of Southern Ocean winds. Clim. Past 7 (4), 1123–1138. https://doi.org/10.5194/cp-7-1123-2011.

Rohling, E.J., Marsh, R., Wells, N.C., Siddall, M., Edwards, N.R., 2004. Similar meltwater contributions to glacial sea level changes from Antarctic and northern ice sheets. Nature 430 (7003), 1016–1021. https://doi.org/10.1038/nature02859.

Rojas, M., 2013. Sensitivity of southern hemisphere circulation to LGM and $4xCO_2$ climates. Geophys. Res. Lett. 40 (5), 965–970. https://doi.org/10.1002/grl.50195.

Rojas, M., Moreno, P., Kageyama, M., Crucifix, M., Hewitt, C., Abe-Ouchi, A., Ohgaito, R., Brady, E.C., Hope, P., 2009. The Southern Westerlies during the last glacial maximum in PMIP2 simulations. Clim. Dyn. 32 (4), 525–548. https://doi.org/10.1007/s00382-008-0421-7.

Rue, E.E.L., Bruland, K.K.W., 1995. Complexation of iron (III) by natural organic ligands in the Central North Pacific as determined by a new competitive ligand equilibration/adsorptive cathodic stripping. Mar. Chem. 50, 117–138. https://doi.org/10.1016/0304-4203(95)00031-L.

Rue, E.L., Bruland, K.W., 1997. The role of organic complexation on ambient iron chemistry in the equatorial Pacific Ocean and the response of a mesoscale iron addition experiment. Limnol. Oceanogr. 42 (5), 901–910. https://doi.org/10.4319/lo.1997.42.5.0901.

Russell, J.L., Stouffer, R.J., Dixon, K.W., 2006. Intercomparison of the Southern Ocean circulations in IPCC coupled model control simulations. J. Clim. 19, 4560–4576. https://doi.org/10.1175/JCLI3869.1.

Sachs, J.P., Lehman, S.J., 1999. Subtropical North Atlantic temperatures 60,000 to 30,000 years ago. Science 286 (5440), 756–759. https://doi.org/10.1126/science.286.5440.756.

Saenko, O. a, Schmittner, A., Weaver, A.J., 2004. The Atlantic – Pacific Seesaw. J. Clim. 17 (11), 2033–2038. https://doi.org/10.1175/1520-0442(2004)017<2033:TAS>2.0.CO;2.

Saito, M. a., Noble, A.E., Tagliabue, A., Goepfert, T.J., Lamborg, C.H., Jenkins, W.J., 2013. Slow-spreading submarine ridges in the South Atlantic as a significant oceanic iron source. Nat. Geosci. 6 (9), 775–779. https://doi.org/10.1038/ngeo1893.

Sarmiento, J.L., Orr, J.C., 1991. Three-dimensional simulations of the impact of Southern Ocean nutrient depletion on atmospheric CO_2 and ocean chemistry. Limnol. Oceanogr. 36 (8), 1928–1950. https://doi.org/10.4319/lo.1991.36.8.1928.

Sarmiento, J.L., Toggweiler, J.R., 1984. A new model for the role of the oceans in determining atmospheric pCO_2. Nature 308 (5960), 621–624. https://doi.org/10.1038/308621a0.

Sarmiento, J.L., Toggweiler, J.R., Najjar, R., Webb, D.J., Jenkins, W.J., Elderfield, H., Whitfield, M., Minster, J., 1988. Ocean carbon-cycle dynamics and atmospheric pCO_2. Philos. Trans. R. Soc. Lond. Ser. A Math. Phys. Sci. 325 (1583), 3–21. https://doi.org/10.1098/rsta.1988.0039.

Schmittner, A., Brook, E.J., Ahn, J., 2007a. Impact of the ocean's overturning circulation on atmospheric CO_2. In: Schmittner, A., Chiang, J.C.H., Hemming, S.R. (Eds.), Geophysical Monograph Series 173: Ocean Circulation: Mechanisms and Impacts. American Geophysical Union, Washington, DC, USA, pp. 209–246. https://doi.org/10.1029/173GM20.

Schmittner, A., Galbraith, E.D., 2008. Glacial greenhouse-gas fluctuations controlled by ocean circulation changes. Nature 456 (7220), 373–376. https://doi.org/10.1038/nature07531.

Schmittner, A., Galbraith, E.D., Hostetler, S.W., Pedersen, T.F., Zhang, R., 2007b. Large fluctuations of dissolved oxygen in the Indian and Pacific oceans during Dansgaard-Oeschger oscillations caused by variations of North Atlantic Deep Water subduction. Paleoceanography 22 (3), PA3207. https://doi.org/10.1029/2006PA001384.

Schmittner, A., Lund, D.C., 2015. Early deglacial Atlantic overturning decline and its role in atmospheric CO_2 rise inferred from carbon isotopes ($\delta^{13}C$). Clim. Past 11 (2), 135–152. https://doi.org/10.5194/cp-11-135-2015.

Schmittner, A., Saenko, O.A., Weaver, A.J., 2003. Coupling of the hemispheres in observations and simulations of glacial climate change. Quat. Sci. Rev. 22 (5–7), 659–671. https://doi.org/10.1016/S0277-3791(02)00184-1.

Schmittner, A., Silva, T.A.M., Fraedrich, K., Kirk, E., Lunkeit, F., 2011. Effects of mountains and ice sheets on global ocean circulation. J. Clim. 24 (11), 2814–2829. https://doi.org/10.1175/2010JCLI3982.1.

Schmittner, A., Weaver, A.J., 2001. Dependence of multiple climate states on ocean mixing parameters. Geophys. Res. Lett. 28 (6), 1027–1030. https://doi.org/10.1029/2000GL012410.

Schmittner, A., Yoshimori, M., Weaver, A.J., 2002. Instability of glacial climate in a model of the ocean- atmosphere-cryosphere system. Science 295 (5559), 1489–1493. https://doi.org/10.1126/science.1066174.

Scholze, M., Knorr, W., Heimann, M., Jena, D., 2003. Modelling terrestrial vegetation dynamics and carbon cycling for an abrupt climatic change event. Holocene 13 (2), 327–333. https://doi.org/10.1191/0959683603hl625rp.

Schulz, M., Seidov, D., Sarnthein, M., Stattegger, K., 2001. Modeling ocean-atmosphere carbon budgets during the Last Glacial Maximum-Heinrich 1 meltwater event-Bølling transition. Int. J. Earth Sci. 90 (2), 412–425. https://doi.org/10.1007/s00531000036.

Sedwick, P.N., DiTullio, G.R., 1997. Regulation of algal blooms in Antarctic shelf waters by the release of iron from melting sea ice. Geophys. Res. Lett. 24 (20), 2515–2518. https://doi.org/10.1029/97GL02596.

Seidov, D., Maslin, M., 2001. Atlantic ocean heat piracy and the bipolar climate seesaw during Heinrich and Dansgaard-Oeschger events. J. Quat. Sci. 16 (4), 321–328. https://doi.org/10.1002/jqs.595.

Sen Gupta, A., England, M.H., 2006. Coupled Ocean-Atmosphere-Ice Response to Variations in the Southern Annular Mode. J. Clim. 19 (18), 4457–4486. https://doi.org/10.1175/JCLI3843.1.

Shemesh, A., Burckle, L.H., Hays, J.D., 1995. Late Pleistocene oxygen isotope records of biogenic silica from the Atlantic sector of the Southern Ocean. Paleoceanography 10 (2), 179–196. https://doi.org/10.1029/94PA03060.

Shemesh, A., Hodell, D., Crosta, X., Kanfoush, S., Charles, C., Guilderson, T., 2002. Sequence of events during the last deglaciation in Southern Ocean sediments and Antarctic ice cores. Paleoceanography 17 (4), 1056. https://doi.org/10.1029/2000PA000599.

Shoenfelt, E.M., Winckler, G., Lamy, F., Anderson, R.F., Bostick, B.C., 2018. Highly bioavailable dust-borne iron delivered to the Southern Ocean during glacial periods. Proc. Natl. Acad. Sci. 115 (44), 11180–11185. https://doi.org/10.1073/pnas.1809755115.

Shu, Q., Song, Z., Qiao, F., 2015. Assessment of sea ice simulations in the CMIP5 models. Cryosphere 9 (1), 399–409. https://doi.org/10.5194/tc-9-399-2015.

Shulmeister, J., Goodwin, I., Renwick, J., Harle, K., Armand, L., McGlone, M.S., Cook, E., Dodson, J., Hesse, P.P., Mayewski, P., Curran, M., 2004. The Southern Hemisphere westerlies in the Australasian sector over the last glacial cycle: a synthesis. Quat. Int. 118–119, 23–53. https://doi.org/10.1016/S1040-6182(03)00129-0.

Siegenthaler, U., Stocker, T.F., Monnin, E., Lüthi, D., Schwander, J., Stauffer, B., Raynaud, D., Barnola, J.-M., Fischer, H., Masson-Delmotte, V., Jouzel, J., 2005. Stable carbon cycle – climate relationship during the late Pleistocene stable carbon cycle – climate relationship during the late Pleistocene. Science 310, 1313–1317. https://doi.org/10.1126/science.1120130.

Siegenthaler, U., Wenk, T., 1984. Rapid atmospheric CO_2 variations and ocean circulation. Nature 308 (5960), 624–626. https://doi.org/10.1038/308624a0.

Sime, L.C., Hodgson, D., Bracegirdle, T.J., Allen, C., Perren, B., Roberts, S., De Boer, A.M., 2016. Sea ice led to poleward-shifted winds at the Last Glacial Maximum: the influence of state dependency on CMIP5 and PMIP3 models. Clim. Past 12 (12), 2241–2253. https://doi.org/10.5194/cp-12-2241-2016.

Sime, L.C., Kohfeld, K.E., Le Quéré, C., Wolff, E.W., Boer, A.M. De, Graham, R.M., Bopp, L., 2013. Southern Hemisphere westerly wind changes during the Last Glacial Maximum : model-data comparison. Quarternary Sci. Rev. 64, 104–120. https://doi.org/10.1016/j.quascirev.2012.12.008.

Skinner, L.C., Fallon, S., Waelbroeck, C., Michel, E., Barker, S., 2010. Ventilation of the deep Southern Ocean and deglacial CO_2 rise. Science 328 (5982), 1147–1151. https://doi.org/10.1126/science.1183627.

Skinner, L.C., Waelbroeck, C., Scrivner, A.E., Fallon, S.J., 2014. Radiocarbon evidence for alternating northern and southern sources of ventilation of the deep Atlantic carbon pool during the last deglaciation. Proc. Natl. Acad. Sci. 111 (15), 5480–5484. https://doi.org/10.1073/pnas.1400668111.

Spence, P., Saenko, O.A., Sijp, W., England, M.H., 2013. North Atlantic climate response to Lake Agassiz drainage at coarse and ocean eddy-permitting resolutions. J. Clim. 26 (8), 2651–2667. https://doi.org/10.1175/JCLI-D-11-00683.1.

Spracklen, D.V., Carslaw, K.S., Kulmala, M., Kerminen, V.M., Sihto, S.L., Riipinen, I., Merikanto, J., Mann, G.W., Chipperfield, M.P., Wiedensohler, A., Birmili, W., Lihavainen, H., 2008. Contribution of particle formation to global cloud condensation nuclei concentrations. Geophys. Res. Lett. 35 (6), 1–5. https://doi.org/10.1029/2007GL033038.

Stauffer, B., Blunier, T., Dällenbach, A., Indermühle, A., Schwander, J., Stocker, T.F., Tschumi, J., Chappellaz, J., Raynaud, D., Hammer, C.U., others, 1998. Atmospheric CO_2 concentration and millennial-scale climate change during the last glacial period. Nature 392 (6671), 59–62. https://doi.org/10.1038/32133.

Stephens, B.B., Keeling, R.F., 2000. The influence of Antarctic sea ice on glacial-interglacial CO_2 variations. Nature 404 (6774), 171–174. https://doi.org/10.1038/35004556.

Stocker, T.F., 2000. Past and future reorganizations in the climate system. Quat. Sci.

Rev. 19 (1), 301–319. https://doi.org/10.1016/S0277-3791(99)00067-0.

Stocker, T.F., Johnsen, S.J., 2003. A minimum thermodynamic model for the bipolar seesaw. Paleoceanography 18 (4), 1087. https://doi.org/10.1029/2003PA000920.

Stocker, T.F., Marchal, O., 2000. Abrupt climate change in the computer: is it real? Proc. Natl. Acad. Sci. 97 (4), 1362–1365. https://doi.org/10.1073/pnas.97.4.1362.

Stocker, T.F., Timmermann, A., Renold, M., Timm, O., 2007. Effect of salt compensation on the climate model response in simulations of large changes of the Atlantic meridional overturning circulation. J. Clim. 20 (24), 5912–5928. https://doi.org/10.1175/2007JCLI1662.1.

Stocker, T.F., Wright, D.G., 1991. Rapid transitions of the ocean's deep circulation induced by changes in surface water fluxes. Nature 351, 729–732. https://doi.org/10.1038/351729a0.

Stommel, H., 1961. Thermohaline convection with two stable regimes of flow. Tellus 13 (2), 224–230. https://doi.org/10.3402/tellusa.v13i2.9491.

Stouffer, R.J., Seidov, D., Haupt, B.J., 2007. Climate response to external sources of freshwater: north Atlantic versus the Southern Ocean. J. Clim. 20, 436–448. https://doi.org/10.1175/JCLI4015.1.

Stouffer, R.J., Yin, J., Gregory, J.M.J.M., Dixon, K.W., Spelman, M.J., Hurlin, W., Weaver, a. J., Eby, M., Flato, G.M., Hasumi, H., Hu, A., Jungclaus, J.H., Kamenkovich, I.V., Levermann, A., Montoya, M., Murakami, S., Nawrath, S., Oka, A., Peltier, W.R., Robitaille, D.Y., Sokolov, A.P., Vettoretti, G., Weber, S.L., Weber, N., 2006. Investigating the causes of the response of the thermohaline circulation to past and future climate changes. J. Clim. 19 (8), 1365–1387. https://doi.org/10.1175/JCLI3689.1.

Sugden, D.E., McCulloch, R.D., Bory, A.J.-M., Hein, A.S., 2009. Influence of Patagonian glaciers on Antarctic dust deposition during the last glacial period. Nat. Geosci. 2 (4), 281–285. https://doi.org/10.1038/ngeo474.

Sun, S., Eisenman, I., Stewart, A.L., 2016. Southern Ocean surface buoyancy forcing controls glacial-interglacial changes in the global deep ocean stratification. Geophys. Res. Lett. 43, 1–9. https://doi.org/10.1002/2016GL070058.1.

Sun, X., Matsumoto, K., 2010. Effects of sea ice on atmospheric pCO_2: a revised view and implications for glacial and future climates. J. Geophys. Res. 115 (G02015), 1–8. https://doi.org/10.1029/2009JG001023.

Swart, N.C., Fyfe, J.C., 2012. Observed and simulated changes in the Southern Hemisphere surface westerly wind-stress. Geophys. Res. Lett. 39 (16), 6–11. https://doi.org/10.1029/2012GL052810.

Swingedouw, D., Fichefet, T., Goosse, H., Loutre, M.F., 2009. Impact of transient freshwater releases in the Southern Ocean on the AMOC and climate. Clim. Dyn. 33 (2–3), 365–381. https://doi.org/10.1007/s00382-008-0496-1.

Swingedouw, D., Fichefet, T., Huybrechts, P., Goosse, H., Driesschaert, E., Loutre, M.F., 2008. Antarctic ice-sheet melting provides negative feedbacks on future climate warming. Geophys. Res. Lett. 35 (17), 2–5. https://doi.org/10.1029/2008GL034410.

Tagliabue, A., Aumont, O., Bopp, L., 2014a. The impact of different external sources of iron on the global carbon cycle. Geophys. Res. Lett. 41 (3), 920–926. https://doi.org/10.1002/2013GL059059.

Tagliabue, A., Aumont, O., DeAth, R., Dunne, J.P., Dutkiewicz, S., Galbraith, E., Misumi, K., Moore, J.K., Ridgwell, A., Sherman, E., Stock, C., Vichi, M., Volker, C., Yool, A., 2016. How well do global ocean biogeochemistry models simulate dissolved iron distributions? Glob. Biogeochem. Cycles 30, 149–174. https://doi.org/10.1002/2015GB005289.

Tagliabue, A., Bopp, L., Aumont, O., 2008. Ocean biogeochemistry exhibits contrasting responses to a large scale reduction in dust deposition. Biogeosciences 5 (1), 11–24. https://doi.org/10.5194/bg-5-11-2008.

Tagliabue, A., Bopp, L., Aumont, O., 2009a. Evaluating the importance of atmospheric and sedimentary iron sources to Southern Ocean biogeochemistry. Geophys. Res. Lett. 36 (13), 1–5. https://doi.org/10.1029/2009GL038914.

Tagliabue, A., Bopp, L., Dutay, J.-C., Bowie, A.R., Chever, F., Jean-Baptiste, P., Bucciarelli, E., Lannuzel, D., Remenyi, T., Sarthou, G., Aumont, O., Gehlen, M., Jeandel, C., 2010. Hydrothermal contribution to the oceanic dissolved iron inventory. Nat. Geosci. 3 (4), 252–256. https://doi.org/10.1038/ngeo818.

Tagliabue, A., Bopp, L., Roche, D.M., Bouttes, N., Dutay, J.-C., Alkama, R., Kageyama, M., Michel, E., Paillard, D., 2009b. Quantifying the roles of ocean circulation and biogeochemistry in governing ocean carbon-13 and atmospheric carbon dioxide at the last glacial maximum. Clim. Past 5, 695–706. https://doi.org/10.5194/cp-5-695-2009.

Tagliabue, A., Bowie, A.R., Boyd, P.W., Buck, K.N., Johnson, K.S., Saito, M.A., 2017. The integral role of iron in ocean biogeochemistry. Nature 543 (7643), 51–59. https://doi.org/10.1038/nature21058.

Tagliabue, A., Resing, J., 2016. Impact of hydrothermalism on the ocean iron cycle. Philos. Trans. R. Soc. 374 (2081), 1–16. https://doi.org/10.1098/rsta.2015.0291.

Tagliabue, A., Sallée, J., Bowie, A.R., Lévy, M., Swart, S., Boyd, P.W., 2014b. Surface-water iron supplies in the Southern Ocean sustained by deep winter mixing. Nat. Geosci. 7, 314–320. https://doi.org/10.1038/ngeo2101.

Tagliabue, A., Völker, C., 2011. Towards accounting for dissolved iron speciation in global ocean models. Biogeosciences 8 (10), 3025–3039. https://doi.org/10.5194/bg-8-3025-2011.

Takahashi, T., Sutherland, S.C., Wanninkhof, R., Sweeney, C., Feely, R. a., Chipman, D.W., Hales, B., Friederich, G., Chavez, F., Sabine, C., Watson, A., Bakker, D.C.E., Schuster, U., Metzl, N., Yoshikawa-Inoue, H., Ishii, M., Midorikawa, T., Nojiri, Y., Körtzinger, A., Steinhoff, T., Hoppema, M., Olafsson, J., Arnarson, T.S., Tilbrook, B., Johannessen, T., Olsen, A., Bellerby, R., Wong, C.S., Delille, B., Bates, N.R., de Baar, H.J.W., 2009. Climatological mean and decadal change in surface ocean pCO_2, and net sea-air CO_2 flux over the global oceans. Deep. Res. Part II Top. Stud. Oceanogr. 56, 554–577. https://doi.org/10.1016/j.dsr2.2008.12.009.

Takemura, T., Egashira, M., Matsuzawa, K., Ichijo, H., O'Ishi, R., Abe-Ouchi, A., 2009. A simulation of the global distribution and radiative forcing of soil dust aerosols at the Last Glacial Maximum. Atmos. Chem. Phys. 9 (9), 3061–3073. https://doi.org/10.5194/acp-9-3061-2009.

Timmermann, A., Friedrich, T., Timm, O.E., Chikamoto, M.O., Abe-Ouchi, A., Ganopolski, A., 2014. Modeling obliquity and CO_2 effects on southern hemisphere climate during the past 408 ka. J. Clim. 27 (5), 1863–1875. https://doi.org/10.1175/JCLI-D-13-00311.1.

Timmermann, A., Krebs, U., Justino, F., Goosse, H., Ivanochko, T., 2005. Mechanisms for millennial-scale global synchronization during the last glacial period. Paleoceanography 20 (4), PA4008. https://doi.org/10.1029/2004PA001090.

Timmermann, A., Menviel, L., Okumura, Y., Schilla, A., Merkel, U., Timm, O., Hu, A., Otto-Bliesner, B., Schulz, M., 2010. Towards a quantitative understanding of millennial-scale Antarctic warming events. Quat. Sci. Rev. 29 (1–2), 74–85. https://doi.org/10.1016/j.quascirev.2009.06.021.

Timmermann, A., Okumura, Y., An, S.I., Clement, A., Dong, B., Guilyardi, E., Hu, A., Jungclaus, J.H., Renold, M., Stocker, T.F., Stouffer, R.J., Sutton, R., Xie, S.P., Yin, J., 2007. The influence of a weakening of the Atlantic meridional overturning circulation on ENSO. J. Clim. 20 (19), 4899–4919. https://doi.org/10.1175/JCLI4283.1.

Toggweiler, J.R., 1999. Variation of atmospheric CO_2 by ventilation of the ocean's deepest water. Paleoceanography 14, 571–588. https://doi.org/10.1029/1999PA900033.

Toggweiler, J.R., Russell, J., 2008. Ocean circulation in a warming climate. Nature 451 (7176), 286–288. https://doi.org/10.1038/nature06590.

Toggweiler, J.R., Russell, J.L., Carson, S.R., 2006. Midlatitude westerlies, atmospheric CO_2, and climate change during the ice ages. Paleoceanography 21 (26), 2005. https://doi.org/10.1029/2005PA001154.

Toggweiler, J.R., Sarmiento, J.L., 1985. Glacial to interglacial changes in atmospheric carbon dioxide: the critical role of ocean surface water in high latitudes. In: Sundquist, E.T., Broecker, W.S. (Eds.), Geophysical Monograph Series 32: the Carbon Cycle and Atmospheric CO_2: Natural Variations Archean to Present. American Geophysical Union, Washington, DC, USA, pp. 163–184. https://doi.org/10.1029/GM032p0163.

Trevena, J., Sijp, W.P., England, M.H., 2008. North Atlantic Deep Water collapse triggered by a Southern Ocean meltwater pulse in a glacial climate state. Geophys. Res. Lett. 35 (9), 1–6. https://doi.org/10.1029/2008GL033236.

Tschumi, T., Joos, F., Gehlen, M., Heinze, C., 2011. Deep ocean ventilation, carbon isotopes, marine sedimentation and the deglacial CO_2 rise. Clim. Past 7, 771–800. https://doi.org/10.5194/cp-7-771-2011.

Tschumi, T., Joos, F., Parekh, P., 2008. How important are Southern Hemisphere wind changes for low glacial carbon dioxide? A model study. Paleoceanography 23 (4), PA4208. https://doi.org/10.1029/2008PA001592.

van Meerbeeck, C.J., Svensson, A., Vandenberghe, J., Renssen, H., Roche, D.M., Wohlfarth, B., Bohncke, S.J.P., Bos, J.A.A., Engels, S., Helmens, K.F., Sánchez-Goñi, M.F., 2011. The nature of MIS 3 stadial-interstadial transitions in Europe: new insights from model-data comparisons. Quat. Sci. Rev. 30, 3618–3637. https://doi.org/10.1016/j.quascirev.2011.08.002.

Vellinga, M., Wood, R.A., 2002. Global climatic impacts of a collapse of the atlantic thermohaline circulation. Clim. Change 54 (3), 251–267. https://doi.org/10.1002/joc.1492.

Vellinga, M., Wood, R.A., Gregory, J.M., 2002. Processes governing the recovery of a perturbed thermohaline circulation in HadCM3. J. Clim. 15 (7), 764–780. https://doi.org/10.1175/1520-0442(2002)015<0764:PGTROA>2.0.CO;2.

Voelker, A.H.L., Workshop Participants, 2002. Global distribution of centennial-scale records for Marine Isotope Stage (MIS) 3: a database. Quat. Sci. Rev. 21 (10), 1185–1212. https://doi.org/10.1016/S0277-3791(01)00139-1.

Völker, C., Köhler, P., 2013. Responses of ocean circulation and carbon cycle to changes in the position of the Southern Hemisphere westerlies at Last Glacial Maximum. Paleoceanography 28 (4), 726–739. https://doi.org/10.1002/2013PA002556.

Völker, C., Tagliabue, A., 2015. Modeling organic iron-binding ligands in a three-dimensional biogeochemical ocean model. Mar. Chem. 173, 67–77. https://doi.org/10.1016/j.marchem.2014.11.008.

Waelbroeck, C., Pichat, S., Böhm, E., Lougheed, B.C., Faranda, D., Vrac, M., Missiaen, L., Vazquez Riveiros, N., Burckel, P., Lippold, J., Arz, H.W., Dokken, T., Thil, F., Dapoigny, A., 2018. Relative timing of precipitation and ocean circulation changes in the western equatorial Atlantic over the last 45 kyr. Clim. Past 14, 1315–1330. https://doi.org/10.5194/cp-14-1315-2018.

Wagener, T., Guieu, C., Leblond, N., 2010. Effects of dust deposition on iron cycle in the surface Mediterranean Sea: results from a mesocosm seeding experiment. Biogeosciences 7, 3769–3781. https://doi.org/10.5194/bg-7-3769-2010.

WAIS Divide Project Members, 2015. Precise interpolar phasing of abrupt climate change during the last ice age. Nature 520 (7549), 661–665. https://doi.org/10.1038/nature14401.

Watson, A.J., Bakker, D.C.E., Ridgwell, A.J., Boyd, P.W., Law, C.S., 2000. Effect of iron supply on Southern Ocean CO_2 uptake and implications for glacial atmospheric CO_2. Nature 407 (6805), 730–733. https://doi.org/10.1038/35037561.

Watson, A.J., Lefèvre, N., 1999. The sensitivity of atmospheric CO_2 concentrations to input of iron to the oceans. Tellus B 51 (2), 453–460. https://doi.org/10.1034/j.1600-0889.1999.00022.x.

Watson, A.J., Vallis, G.K., Nikurashin, M., 2015. Southern Ocean buoyancy forcing of ocean ventilation and glacial atmospheric CO_2. Nat. Geosci. 8, 861–864. https://doi.org/10.1038/ngeo2538.

Weaver, A.J., Saenko, O.A., Clark, P.U., Mitrovica, J.X., 2003. Meltwater pulse IA from Antarctica as a trigger of the Bølling-Allerød warm interval. Science 299 (5613), 1709–1713. https://doi.org/10.1126/science.1081002.

Weber, M.E., Clark, P.U., Kuhn, G., Timmermann, A., Sprenk, D., Gladstone, R., Zhang, X., Lohmann, G., Menviel, L., Chikamoto, M.O., Friedrich, T., Ohlwein, C., 2014. Millennial-scale variability in Antarctic ice-sheet discharge during the last deglaciation. Nature 510 (7503), 134–138. https://doi.org/10.1038/nature13397.

Wenk, T., Siegenthaler, U., 1985. The high-latitude ocean as a control of atmospheric CO_2. In: Sundquist, E.T., Broecker, W.S. (Eds.), Geophysical Monograph Series 32: the Carbon Cycle and Atmospheric CO_2: Natural Variations Archean to Present. American Geophysical Union, Washington, DC, USA, pp. 185–194. https://doi.org/DOI: 10.1029/GM032p0185.

Werner, M., Tegen, I., Harrison, S.P., Kohfeld, K.E., Prentice, I.C., Balkanski, Y., Rodhe, H., Roelandt, C., 2002. Seasonal and interannual variability of the mineral dust cycle under present and glacial climate conditions. J. Geophys. Res. Atmos. 107 (24), 1–19. https://doi.org/10.1029/2002JD002365.

Wilcox, L.J., Charlton-Perez, A.J., Gray, L.J., 2012. Trends in Austral jet position in ensembles of high- and low-top CMIP5 models. J. Geophys. Res. Atmos. 117 (13), 1–10. https://doi.org/10.1029/2012JD017597.

Winckler, G., Anderson, R.F., Fleisher, M.Q., McGee, D., Mahowald, N., 2008. Covariant glacial-interglacial dust fluxes in the equatorial Pacific and Antarctica. Science 320, 93–96. https://doi.org/10.1126/science.1150595.

Winguth, A.M.E., Archer, D., Duplessy, J.C., Maier-Reimer, E., Mikolajewicz, U., 1999. Sensitivity of paleonutrient tracer distributions and deep-sea circulation to glacial boundary conditions. Paleoceanography 14 (3), 304–323. https://doi.org/10.1029/1999PA900002.

Wolff, E.W., Fischer, H., Fundel, F., Ruth, U., Twarloh, B., Littot, G.C., Mulvaney, R., Röthlisberger, R., De Angelis, M., Boutron, C.F., Hansson, M., Jonsell, U., Hutterli, M.A., Lambert, F., Kaufmann, P., Stauffer, B., Stocker, T.F., Steffensen, J.P., Bigler, M., Siggaard-Andersen, M.L., Udisti, R., Becagli, S., Castellano, E., Severi, M., Wagenbach, D., Barbante, C., Gabrielli, P., Gaspari, V., 2006. Southern Ocean sea-ice extent, productivity and iron flux over the past eight glacial cycles. Nature 440 (7083), 491–496. https://doi.org/10.1038/nature04614.

Wyrwoll, K.H., Dong, B., Valdes, P., 2000. On the position of southern hemisphere westerlies at the Last Glacial Maximum: an outline of AGCM simulation results and evaluation of their implications. Quat. Sci. Rev. 19 (9), 881–898. https://doi.org/10.1016/S0277-3791(99)00047-5.

Ye, Y., Völker, C., 2017. On the role of dust-deposited lithogenic particles for iron cycling in the tropical and subtropical atlantic. Glob. Biogeochem. Cycles 31 (10), 1543–1558. https://doi.org/10.1002/2017GB005663.

Zhang, R., Delworth, T.L., 2005. Simulated tropical response to a substantial weakening of the Atlantic thermohaline circulation. J. Clim. 18 (12), 1853–1860. https://doi.org/10.1175/JCLI3460.1.

Ziegler, M., Diz, P., Hall, I.R., Zahn, R., 2013. Millennial-scale changes in atmospheric CO_2 levels linked to the Southern Ocean carbon isotope gradient and dust flux. Nat. Geosci. 6, 457–461. https://doi.org/10.1038/ngeo1782.